Durability of high-performance Thin-Ply composites

Vom Promotionsausschuss der
Technischen Universität Hamburg

zur Erlangung des akademischen Grades

Doktor-Ingenieur (Dr.-Ing.)

genehmigte Dissertation

von
Benedikt Kötter

aus
Thuine (Emsland)

2021

Vorsitzender des Prüfungsausschusses:	Prof. Dr.-Ing. Benedikt Kriegesmann (Technische Universität Hamburg)
Gutachter:	Prof. Dr.-Ing. habil. Bodo Fiedler (Technische Universität Hamburg) Prof. Clemens Dransfeld (Delft University of Technology)
Tag der mündlichen Prüfung:	30.09.2021

Technisch-Wissenschaftliche Schriftenreihe

Herausgeber:
Prof. Dr.-Ing. habil. Bodo Fiedler

Anschrift:
Technische Universität Hamburg
Institut für Kunststoffe und Verbundwerkstoffe
Denickestraße 15
21073 Hamburg

Band 40:
Durability of high-performance Thin-Ply composites

Benedikt Kötter
1. Auflage
Hamburg 2021

ISSN 2625-6029

Bibliographische Information der Deutschen Nationalbibliothek:
Die deutsche Nationalbibliothek verzeichnet diese Publikation in der Deutschen Nationalbibliothek; detaillierte Informationen sind im Internet über dnb.de abrufbar.

Acknowledgements

First and foremost, I would like to thank Prof. Dr.-Ing. habil. Bodo Fiedler for his guidance and support of this research. Numerous discussions and the free space in the research have led to the success of the work.
Furthermore, I would like to thank Prof. Clemens Dransfeld for taking on the position of second assessor and Prof. Dr.-Ing. Benedikt Kriegesmann in his function of chairman.
Great thanks go to all colleagues at the Institute of Polymer and Composites for the highly friendly working atmosphere and the many inspiring discussions. I would especially like to thank Johann Körbelin, Julian Karsten, Sergej Harder, Christina Buggisch, Dennis Gibhardt and Janina Endres for the numerous scientific discussions and the joint research. The last few years have been a great time. Part of the work was done in collaboration with Kyoto University. I would like to thank Prof. Masaki Hojo and Assoc. Prof. Masaaki Nishikawa, for the opportunity of the research stay, the many helpful discussions and the warm welcome. I would also like to thank Kohei Yamada for his support. Furthermore, I would like to thank "Der Übersee-Club e.V." for the financial support of a scholarship for my research stay in Japan.
I would like to say thank you to the students I supervised for their work, which contributed a lot to the success of the research experiments. I would also like to thank my parents Mechthild and Wolfgang, and my brother Jonas for their support. Finally, I thank my wife Christina. She provides me with a haven of peace away from work.

One never notices what has been done,
one can only see what remains to be done.

Marie Curie (1867 - 1934)

Kurzfassung

Um das Gewicht von Bauteilen aus Verbundwerkstoffen weiter zu reduzieren, muss das volle Potenzial der Kohlenstofffasern ausgenutzt werden. Eine Verringerung der Schichtdicke stellt einen möglichen Ansatz dar. Eine Reduzierung erhöht den Freiheitsgrad im Design und steigert die Zug- und Druckfestigkeiten. Allerdings führt dieses zu einer höheren Kerbempfindlichkeit und vorzeitigem Versagen in Bereichen von hohen Spannungskonzentrationen. Bei dem Einsatz von dünnen Schichtdicken in Strukturbauteilen muss dementsprechend ein Kompromiss eingegangen werden.
Aus diesem Grund wird in dieser Thesis folgende Forschungshypothese untersucht:

> *Thin-Ply Verbundwerkstoffe steigern das Leichtbaupotenzial von Primärstrukturen*

Vier Einschränkungen hinsichtlich des Einsatzes von Thin-Ply Verbundwerkstoffen in Primärstrukturen werden identifiziert und Arbeitsannahmen formuliert, welche experimentell untersucht werden:

1. Die lokale Einbettung von Edelstahlfolien (Hybridisierung) in Thin-Ply Laminaten reduziert die Auswirkungen von Spannungskonzentrationen sowie die Festigkeitsdegradation
2. Die Belastbarkeit von Bolzenverbindungen wird durch lokale Stahlhybridisierungen von Thin-Ply Laminaten erhöht
3. Eine Reduzierung der Schichtdicke verbessert das Verhalten unter zyklischer Belastung
4. Das Ermüdungsverhalten von einer durch einen Schlagschaden geschädigten Struktur wird durch eine Verringerung der Schichtdicke verbessert

Um die Auswirkungen von Spannungskonzentrationen zu reduzieren und die Belastbarkeit von Bolzenverbindungen zu verbessern, werden 90° CFK-Lagen lokal durch Edelstahlfolien ersetzt. Die Zugfestigkeit von gekerbten Proben nimmt mit zunehmendem Stahlanteil signifikant zu. Selbst wenn die Festigkeit auf die Dichte bezogen wird, steigt die spezifische Festigkeit um bis zu 36 % an und die Kerbempfindlichkeit wird reduziert. Die Belastbarkeit von Bolzenverbindungen steigt um 54.6 % aufgrund der stützenden Wirkung der Stahlfolien gegen Ausbeulen an.
Ermüdungsversuche wurden mit und ohne Schlagschädigung bei unterschiedlichen Lastverhältnissen durchgeführt. Durch die Reduzierung der Schichtdicke kann eine Verbesserung des Langzeitverhaltens unabhängig vom Lastverhältnis erreicht werden. Die Ergebnisse der mit Schlagschaden behafteten Proben zeigen, dass die Schichtdicke, die Form der Delaminationen sowie die Dicke und der Aufbau der Sublaminate entscheidend für das Langzeitverhalten sind. Computertomografie-Aufnahmen zeigen, dass die geschädigten Bereiche von Thin-Ply Proben unter Ermüdungsbelastung nicht zunehmen. Im Gegensatz dazu wächst die Schädigung von Thick-Ply Proben mit zunehmender Zyklenzahl progressiv bis zum Versagen an.
Die Ergebnisse zeigen, dass Thin-Ply Verbundwerkstoffe das Leichtbaupotenzial von Primärstrukturen verbessern und die Forschungshypothese verifiziert werden kann.

Abstract

To decrease the weight of composite structures further, it is essential to develop a method to exploit the full potential of carbon fibres. One approach is to reduce the layer thickness. As a result, the degree of freedom in design and the tensile and compressive strength increases. However, the use of thinner layer thicknesses leads to a higher notch sensitivity and premature failure in areas of high stress concentrations. Unfortunately, concerning structural applications, a compromise has to be made.
Therefore, this thesis examines the research hypothesis:

> *Thin-Ply composites improve the lightweight potential of primary structures*

Four limitations regarding the use of Thin-Ply composites in primary structures were identified, and working assumptions were formulated, which were investigated experimentally:

1. Local steel hybridisation of Thin-Ply laminates reduces the impact of stress concentrations and strength degradation
2. Local steel hybridisation of Thin-Ply laminates improves load-bearing capacity
3. Reducing the layer thickness improves the durability under fatigue loading
4. Reducing the layer thickness improves the fatigue behaviour of structures with impact damage

To reduce the impact of stress concentrations and improve the bearing strength 90° CFRP layers are substitute locally by stainless steel foils. The open hole tensile strength increases significantly with increasing steel content. Even if

the strength is related to the density, the specific strength increases by up to 36 % and the notch sensitivity decreases. The bearing strength increases by 54.6 % due to the buckling support of the steel foils.
Fatigue tests were carried out with and without impact damage under different load ratios. Reducing the layer thickness and improving long-term behaviour can be achieved independent of the load ratio. The results of the impacted samples show that the layer thickness, the shape of the delaminations and the thickness and structure of the sub-laminates are decisive for the long-term behaviour. Computed tomography images show that the damaged areas of Thin-Ply samples do not increase during fatigue loading. In contrast, the damage of Thick-Ply samples growths progressively throughout the whole sample with increasing numbers of cycles until final failure.
In summary, the research hypothesis can be verified, and Thin-Ply composites improve the lightweight potential of primary structures.

Contents

List of characters and abbreviations

Characters

Latin characters

Character	Unit	Description
a	–	Normalised stress amplitude
A	–	Parameter to calculate the material behaviour under cyclic loading
B	–	Parameter to calculate the material behaviour under cyclic loading
c	–	Normalized compressive stress
d	mm	Diameter of the hole
D	%	Degradation
f	–	Parameter to calculate the material behaviour under cyclic loading
h	mm	Height
k	–	Load per hole factor
K	–	Calculation factor (single- or double-shear test)
m	–	Normalized mean stress
N	–	Number of cycles
p	–	Parameter to calculate the material behaviour under cyclic loading
P	N	Load

q	–	Parameter to calculate the amplitude and mean stress
r	–	Parameter to calculate the material behaviour under cyclic loading
R		Load Ratio
R^2	–	Correlation factor
t	mm	Thickness
u	–	Parameter to calculate the material behaviour under cyclic loading
v	–	Parameter to calculate the material behaviour under cyclic loading
w	mm	Width
y	–	Parameter to calculate the mean stress
z	–	Parameter to calculate the amplitude and mean stress

Greek characters

Symbol	**Unit**	**Description**
δ	mm	Displacement
ϵ	%	Strain
σ	MPa	Stress
τ	MPa	Shear stress
Ψ	%	Steel content (Vol.)

Indices

Index	Description
$\perp$	Transverse
1	First value
2	Second value
3	Third value
1TT	First known measured value
a	Amplitude
br	Bearing
CFRP	Carbon fibre reinforced composite
fa	Fibre areal weight
i	Value at point i
ISS	Interlaminar shear stress
LEFM	Linear elastic fracture mechanics
m	Mean
max	Maximum
min	Minimum
n	Number of repetitions
net	Net section
OHT	Open hole tension
s	Symmetrical
SF	Steel foil
’	Unknown parameter

Abbreviations

Abbr.	Description
AE	Acoustic emission
CAI	Compression after impact
CFRP	Carbon fibre reinforced polymer
CLD	Constant-life diagram
COD	Coefficient of determination
CT	Computed tomography
CTE	Coefficient of thermal expansion
DCB	Double cantilever beam
DIC	Digital image correlation
ENF	End notched flexure
FAI	Fatigue after impact
FML	Fibre metal laminate
FRP	Fibre reinforced polymer
HCCF	Hydraulic composites compression fixture
IFF	Inter-fibre fracture
ILSS	Interlaminar shear strength
ITCF	Industrial Technology Center of Fukui Prefecture
NSR	Notched strength reduction ratio
NTPT	Northern Thin Ply Technology
OHT	Open hole tension
PAA	Phosphoric acid anodizing
pbw	Parts by weight
RD	Rolling direction
SEM	Scanning electron microscope
SF	Steel foil
TRD	Transverse rolling direction
TUHH	Hamburg University of Technology
UCS	Ultimate compressive strength

UTS	Ultimate tensile strength

1 Introduction

Due to the excellent density-specific mechanical properties, carbon fibre reinforced polymers (CFRPs) are often used for lightweight structures [1]. However, conventional CFRP laminates or structures do not exploit the full potential of the used carbon fibres. To reduce the weight of future composite structures, it is important to develop a method to exhaust the full potential of carbon fibres [2, 3].

One approach to improve their mechanical performance is to reduce the layer thickness. Kawabe et al. and Sihn et al. presented a spread-tow process to produce thin unidirectional plies; so-called Thin-Ply [4, 5]. Currently, Thin-Ply prepregs with a layer thickness of up to 18 µm are commercially available. Manufacturers such as NTPT (Northern Thin Ply Technology, Switzerland) or research institutions such as the Industrial Technology Center of Fukui Prefecture (ITCF), Japan, have focused on the production of thin prepregs made of carbon fibres and thermoset or thermoplastic matrices.

Thin-ply laminates offer a wide range of benefits regarding their possible applications or their mechanical behaviour. An essential characteristic of Thin-Ply laminates is the degree of freedom in design. The possibility of using a higher number of layers with the same laminate thickness allows to design more load-dependent and to be less influenced by the classical design rules such as symmetry, balance of the laminate, and minimum percentage of same oriented fibres [6]. Besides the degree of freedom in design, the laminate quality improves concerning void content, fibre angle deviation and resin-rich areas with decreasing layer thickness. The higher quality can be attributed to the spreading process, which results in a more homogeneous fibre distribution [7, 8]. Furthermore, the failure behaviour is highly dependent on the layer

thickness. A decreased layer thickness suppresses transverse microcracking and free edge delamination due to increased transverse tensile strength (in situ effect) [9]. The failure mode changes from complex delamination dominated failure to a brittle failure from Thick- to Thin-Ply [5, 8–11], which results in a higher ultimate tensile and compressive strength for unnotched quasi-isotropic specimens [5, 7, 8].

1.1 Aims and scope

Previous studies have shown that the use of thin-layer prepregs significantly increases the tensile and compressive strengths and leads to brittle material behaviour [5, 7, 8]. However, the studies also showed that areas with high stress concentrations lead to premature failure [8, 10, 12, 13]. Unfortunately, concerning structural applications a compromise has to be made. Therefore, the following research hypothesis emerges:

> *Thin-Ply composites improve the lightweight potential of primary structures*

The concept chosen in this thesis to evaluate the research hypothesis is to divide it into separate working assumptions that can be investigated experimentally. The working assumptions are based on a case study from the aviation industry. Figure 1.1 shows a section of a primary structure of an aircraft fuselage. Based on a primary structure, possible limitations in the use of Thin-Ply laminates are identified.

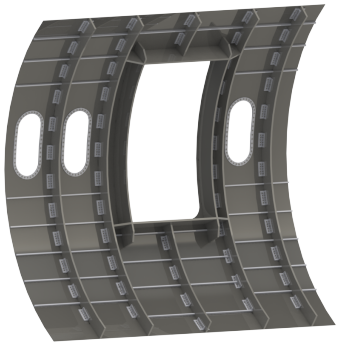

Figure 1.1: Section of a primary structure of an aircraft fuselage.

Areas with high stress concentrations are the first limitation regarding the use of Thin-Ply for primary structures. Examples are the window cut-outs or the corners of the door cut-outs of the fuselage. Previous studies have shown that stress concentrations significantly reduce the strength. The results of Amacher et al. show that in the case of open hole tensile (OHT) tests, the OHT strength of Thin-Ply is 26 % lower than the OHT strength of Thick-Ply. In contrast, the tensile strength of the Thin-Ply specimens is 42 % higher than the tensile strength of the Thick-Ply specimens. The reduction in strength due to stress concentrations increases with decreasing layer thickness [8].
To reduce the impact of stress concentrations, previous studies developed Thick-Ply hybrid composites that combine the characteristics of fibre-reinforced polymers (FRPs), and metals [14–16]. Fibre metal laminates (FML) combine the superior fatigue and fracture properties of FRPs with the ductility and durability of metals [17]. A limiting factor is the interlaminar shear strength of the interface between metal and FRP. In case of insufficient adhesion, delaminations initiate, which lead to premature failure [18, 19]. However, within Thin-Ply laminates, the interlaminar shear stresses could be lower due to the high number of layers, and thus the influence of adhesion is reduced. Therefore, the first working assumption results in:

1. *Local steel hybridisation of Thin-Ply laminates reduces the impact of stress concentrations and strength degradation*

The second limitation is the introduction of loads via bolt connections. Previous studies have shown that the bearing strength increases with decreasing layer thickness [8, 20, 21]. However, due to the higher performance of the Thin-Ply composites, the wall thickness of the structures will be reduced. A thinner wall thickness in turn weakens the load-bearing capacity. Even when using Thick-Ply composites, strength-enhancing methods, for example local thickening, are often required in areas with bolt connections. By hybridising with metals, local thickening could be avoided, and the bearing strength could be increased. Furthermore, the use of metals causes progressive material behaviour [22–24]. Earlier studies have already shown that the bearing strength increases almost linearly with increasing metal content in the case of Thick-Ply laminates [24]. Therefore, the second working assumption results in:

2. *Local steel hybridisation of Thin-Ply laminates improves load-bearing capacity*

Working assumptions three and four investigate fatigue behaviour. Earlier studies demonstrated a strong correlation between stiffness degradation and the development of damage in the material under cyclic loading [25, 26]. Furthermore, a distinction must be made between the load ratios. The fatigue failure behaviour under tensile - tensile load is different from that under tensile-compressive load [27]. Since the failure behaviour of Thin-Ply already differs from Thick-Ply in static loading, it is of particular interest to analyse the fatigue behaviour of Thin-Ply under different load ratios. Therefore, the third working assumption results in:

3. *Reducing the layer thickness improves the durability under fatigue loading*

In particular, primary structures are not allowed to fail catastrophically under cyclic loading, even in the case of predamage. In the case of Thick-

Ply FRPs, several studies have investigated the fatigue after impact (FAI) behaviour. Delaminations significantly reduce the lifetime [28–30]. At the same time, studies on impact damage of Thin-Ply show that the delamination areas increase with thinner layers [8, 31]. In combination with the larger delamination area, the impact behaviour could be a limiting factor using Thin-Ply in primary structures. However, previous studies show that under tensile and compressive loading of undamaged samples, less damage is initiated with decreasing layer thickness and existing damage grows more slowly [5, 8, 32]. This can have positive effects on the cyclic performance of structures damaged by an impact. The fourth working assumption results in:

4. *Reducing the layer thickness improves the fatigue behaviour of structures with impact damage*

1.2 Structure of the thesis

This thesis is divided into two major sections. In the first section, working assumptions one and two analyse the hybridisation of Thin-Ply CFRP. Stainless steel foils are used as patches locally in areas with high stress concentrations. The foils substitute 90° CFRP layers. To verify the two working assumptions, the first step is to examine the surface pre-treatment method of the stainless steel foil. It is essential to achieve a sufficient adhesion between the stainless steel and the CFRP to prevent delamination during loading, which would lead to premature failure. Interlaminar shear strength (ILSS) tests determine the interlaminar shear strength. The fracture toughness is investigated by double cantilever beam (Mode I), and end notched flexure (Mode II) tests. Fibre metal laminates with different fibre areal weights (40 and 160 gsm) are examined. The steel content ranges between 0 and 25 % (0, 6.25, 12.5 and 25 %). According to ASTM D5766-02a [33], open hole tensile tests are carried out to verify the first working assumption. The second working assumption's verification is carried out by bearing tests according to ASTM D5961-01 [34]. The failure behaviour is analysed using a digital image correlation system

(DIC) and micrographs.
The second major section of this thesis analysed the fatigue behaviour. For this purpose, laminates with different fibre areal weights (30, 60, 120, 240 and 360 gsm) are investigated. Three different load ratios are tested. Tensile-tensile (R=0.1), tensile-compressive (R=-0.5) and compressive-compressive (R=10) tests were carried out. S-N curves were recorded for the respective layer thicknesses. Analytical approaches to describe the fatigue behaviour are carried out by using a constant-life diagram. The failure behaviour was analysed based on the hystereses, stiffness decreases and the fracture patterns. For the fourth working assumption, tensile specimens are impacted using a drop tower and tested for fatigue at a load ratio of R=-0.5. S-N curves are recorded for the different layer thicknesses. The damage progression was followed by computed tomography images, whereby the samples were scanned after a certain number of cycles.

2 Scientific and technological background

2.1 Carbon fibre reinforced polymers

Due to the excellent density specific properties, CFRPs are often used in high-performance structures and consists of high-strength carbon fibres embedded in a polymer system [35]. In the context of this thesis, an epoxy resin system is used. The functions of the matrix are to transfer the loads between the fibres, fix the fibres, support them under compressive load, and protect the fibres against external influences such as chemicals or environmental conditions [35, 36]. The main task of the fibres is to carry the loads. They are composed of individual graphite layers, whereby the carbon atoms are bonded to each other via covalent bonds. Covalent bonds lead to high stiffness and strength. The theoretical Young's modulus in fibre direction is 1050 GPa [37]. Orthogonal to the fibre direction, van der Waals forces connect the graphite layers. Van der Waals forces lead to anisotropic material properties. The stiffness transverse to the fibre is only about 1/10 of the fibre direction's stiffness [38, 39]. In addition to the fibres and the matrix, the boundary layer between them has an essential part of mechanical properties. The interface transfers the loads from the matrix to the fibres. In the production process of carbon fibres, the surface of the fibres is often chemically treated to improve adhesion [35, 39]. Unidirectional prepregs are used within this thesis. Prepregs are layers of fibres pre-impregnated with resin. Composite materials usually consist of several layers. To compensate for a single layer's anisotropic properties, layers are combined with different fibre orientations [39]. Contrary to metals, where only the geometry has to be considered in the design process, composites'

design process is more complex. The most important parameters are the following [35]:

- Number of plies (wall thickness)
- Fibre volume content
- Orientation of layers
- Layer thickness
- Lay-up (layer sequence)

2.2 Damage mechanisms of fibre reinforced polymers

Due to their inhomogeneous and anisotropic structure, FRPs exhibit complex stress states under static and fatigue loading. Depending on the type of load, different fracture modes occur. Ehrenstein divided the fracture modes into two classes [40]. The first class is fibre failure, which represents a final failure of the structure. The second class is matrix failure. Matrix failures do not directly lead to a final failure of the structure. They initiate the damage process of FRPs [41]. A more detailed concept is pursued by Puck, who has divided the failure mechanisms of a fibre composite into four categories. The first three categories are matrix failures and the fourth category is fibre failure [42, 43]:

1. Micro-cracks
2. Inter-fibre fracture
3. Delamination
4. Fibre fracture

To provide a more detailed understanding of a fibre composite material's failure behaviour, a typical failure behaviour of a cross-ply laminate is explained below.
A characteristic damage process starts with the formation of micro-cracks. They occur under low stresses within the matrix or at the interface between matrix and fibre. The stresses result from external loads, and thermally

induced stresses from the production process [44]. Concerning the laminate's mechanical properties, micro-cracks have only a negligible influence on the strength and stiffness. The cracks grow as a result of increasing loads or fatigue stresses. When the cracks have reached macroscopic sizes, they are called inter-fibre fractures (IFF) [45]. IFFs typically grow perpendicular to the load within a layer and are stopped at adjacent layers with different fibre orientation. In areas with IFFs, no tensile forces can be transmitted within the layer. In degradation models, macroscopic cracks are described by reduced stiffness [39, 46, 47]. The stresses have to be transferred to neighbouring layers. High interlaminar shear stresses are a consequence of the load transfer so that the layer with an inter-fibre fracture will reach its original stress state again at a certain distance from the crack. If the interlaminar shear stresses exceed a critical value, delaminations, a separation of two layers, develop [40, 45]. The stress state at an inter-fibre fracture, which leads to the initiation of delamination, is shown in Figure 2.1.

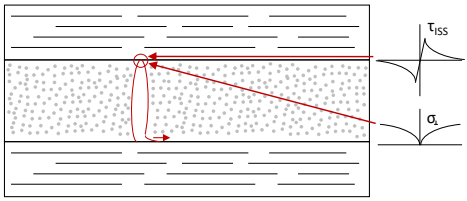

Figure 2.1: Schematic representation of the initiation of a delamination due to interlaminar shear stresses at an inter-fibre fracture.

Delaminations have a relatively small influence on the tensile strength, as they do not influence the fibres' load transfer. However, under compressive loads, the separation of the layers leads to premature failure through buckling, as the bending stiffness of the laminate decreases [42, 43].
Fibre fracture is the final failure. Not all fibres fail at the same time. Fibres with material defects or damage from the production process fail first, and the neighbouring fibres have to take up and transfer the load. If the fibres'

stress exceeds the maximum strength, the final fracture occurs [39]. Under compressive loads, the fibres fail due to buckling [48] or kinking [49].

2.2.1 Damage mechanism under low-velocity impact

The behaviour under impact is a challenge concerning primary structures, as the damage is invisible to the naked eye and reduces the mechanical properties and durability [39]. Methods such as ultrasonic examination, active thermography or computed tomography are used [50–54]. The type of impact used in this thesis is a low-velocity impact, which is characterised by an impact velocity below 20 m/s [55]. The damage caused by the impact is concentrated in a small area. In most cases, however, damage occurs throughout the entire laminate. A conical damage structure starting from the impact can be found [45]. A typical failure pattern of a CFRP laminate after a low-velocity impact is shown in Figure 2.2. The damage consists of different types of defects such as matrix cracks, delaminations and, at higher energies of the impact or low stiffnesses of the laminate, fibre fractures, which occur due to the tensile stresses on the backside of the specimen [56, 57]. The bending of the specimen during the impact causes local tensile or compressive stresses. The stresses lead to inter-fibre fractures in the 90° layers, which grow through the entire layer and stop at neighbouring layers with different fibre orientations. If the energy at the crack tip exceeds a critical value, delaminations initiate from the crack tip between the layers and grow [45, 56].

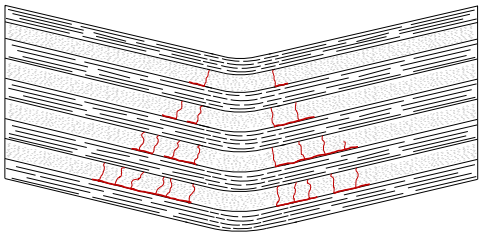

Figure 2.2: Low-velocity impact damage of a cross-ply CFRP laminate. The red lines represent damage such as inter-fibre fractures and delaminations.

2.2.2 Damage mechanism of notched laminates

The failure behaviour of notched composites with high stress concentrations strongly depends on the specimen geometry. Four parameters have a significant influence on the failure behaviour [58]:

- Specimen width
- Lay-up structure
- Ratio between hole diameter and specimen width
- Layer thickness

Depending on the combination of the above parameters, the failure is delamination dominated or fibre-dominated. Commercially available ply thicknesses in the range around 200 µm in conjunction with the specimen geometries specified in the ASTM standard D5766 (Open Hole Tensile Strength of Polymer Matrix Composite Laminates) [33] usually result in delamination-dominated failure behaviour [12]. Regarding the failure mechanism, first cracks occur under tensile stress in the 45° surface layers of the quasi-isotropic laminate ($[45/90/\text{-}45/0]_{ns}$). A representation of the failure mechanism is shown in Figure 2.3. Due to the interlaminar shear stresses at the tip of the inter-fibre fractures, delaminations develop at the interface of the 45°/90° ply. Besides, more inter-fibre fractures occur in the ±45° and 90° plies, and delaminations

initiate between the plies as the load increases. The delaminations occur at the hole and edges of the specimen. Splitting can occur within the 0° plies. Delamination and splitting at the hole blunt the stress concentration and suppress premature failure [58].

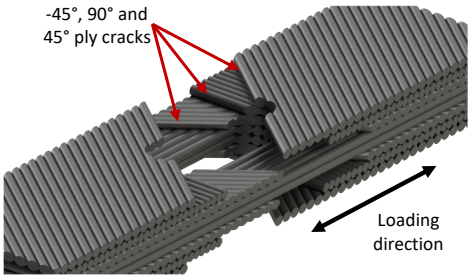

Figure 2.3: Overview of the damage mechanism of notched composite laminates.

For wide specimens, the delaminations at the hole and at the edges do not interact. The strength of the OHT sample converges with increasing width to the strength of an unnotched sample with an equivalent cross-section [58]. On the other hand, if the formation of delaminations is suppressed, such as by thinner ply thicknesses, a fibre-dominant failure behaviour occurs. By suppressing pre-damage, the stress concentration cannot blunt, and premature brittle failure occurs at lower stresses [8, 58, 59].

2.2.3 Damage mechanism under bearing stress

In primary structures and high load components, bolt connections are used for load transfer between joining parts. The advantage of bolt connections is that their failure behaviour shows a progressive damage characteristic and allows damage to be visually detected. Particularly in the case of FRP, a low decrease in the fatigue strength of bolted parts can be observed compared

to metals [35, 60]. FRPs behave similarly under bearing as elastic-plastic metals, which reduce the stress peaks by plastic deformation. In the case of FRP, the stress peaks are relieved locally by delamination and inter-fibre fractures that occur on the compression side of the hole. In the case of fibres that are oriented in the load direction, shear buckling can occur. Due to the formation of damage, the stresses are diverted to other areas, and the stress concentrations are blunted, and the hole widens [35].
Depending on the specimen geometry, the material properties of the joining parts and the properties of the bolt, different failure modes can occur. Figure 2.4 schematically shows four failure modes.

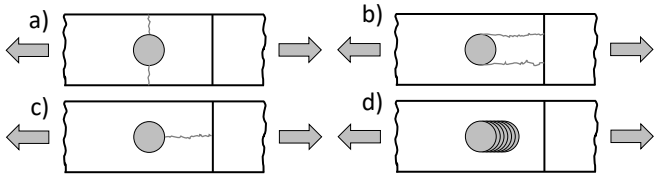

Figure 2.4: Failure modes of FRP under bearing stress: a) Tension failure, b) Shearout failure, c) Cleavage, d) Bearing failure.

Tension failure usually occurs when the nominal cross-section of the sample is too small or the stress concentration at the notch leads to fibre breakage. The most effective method to prevent tension failure is to use more 0° plies. Another failure mode is shear out failure. If this failure is observed, the edge distance may be too small or the shear strength of the joined part is too low. If the shear strength is too low, additional ±45° or 90° layers can be added. The third mode is cleavage. Cleavage occurs when the transverse tensile strength is too low, as is the case with unidirectional laminates. The simplest solution to increase the transverse tensile strength is by increasing the number of 90° plies. The fourth mode of failure is bearing failure. This type of failure should be targeted in designing a bolted connection as it is a fail-safe design. Although the hole expands, a residual strength remains so

that no final failure occurs. A typical laminate design for tension load cases consists of 50 % 0°, 40 % ±45° and 10 % 90° plies [35].
There are several possibilities to increase the bearing strength. These include clamping the joining parts to use the friction between them as a load-transferring factor or local thickening [35]. However, asymmetrical thickening leads to further stresses in the material due to the eccentricity. To avoid thickening, metal sheets can be used. They substitute locally the weaker layers (90° and if necessary ±45°) in areas with high stress concentrations [35, 61]. Figure 2.5 shows a schematic representation of such a hybrid material.

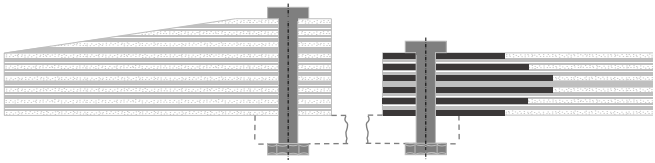

Figure 2.5: Methods to increase the load capacity of bolt connections; left) Conventional thickening of the laminate; right) Metal sheets locally substitute 90° CFRP layers in the area of the bolt connection.

Due to the metal sheets' high stiffness, they transfer high stresses and distribute them throughout the laminate. Furthermore, they suppress cleavage and shear out failure due to their isotropic material behaviour (see Figure 2.4). Plastic deformations of the metal can dissipate additional energies and increase the bearing strength. To prevent electrolytic corrosion between carbon fibres and metal, titanium alloys (e.g. Ti6Al14V) or stainless steels (e.g. 1.4310) are used [35, 61].

2.2.4 Damage mechanism under fatigue loading

Depending on the stress state, laminate structure and material, the cyclic behaviour differs significantly from the behaviour under static load [62]. For the design of primary structures, it is essential to know the cyclic failure behaviour. Fibre composites show superior properties under tensile-tensile loading compared to metals. The maximum cyclic stress to achieve long-term strength is 30 % of the ultimate tensile strength (UTS) for metals. In the case of FRP, this is 60-80 % of the UTS [41, 62]. In contrast to metals, initial damage in FRP already occurs at low cycle numbers. But the damage growth decelerates with an increasing number of cycles. In metals, the cracks grow slow at low cycle numbers but accelerate with increasing cycle numbers [39, 41, 62, 63]. In general, the damage growth of an FRP can be represented as follows [41]:

$$dD/dN = f(\sigma, R, D) \tag{2.1}$$

Here, dD/dN represents the damage growth related to the number of cycles. The damage growth is dependent on the cyclic stress σ, the load ratio $R = \sigma_{\min}/\sigma_{\max}$ and the current damage state D. However, the function f depends on material properties and specimen geometries and cannot be generalised [41].
Figure 2.6 presents a typical curve of the degradation D over the number of cycles N of a CFRP cross-ply laminate. Several studies have been shown that the relative stiffness decrease E/E_0 can be considered analogous to the degradation D [47]. The degradation development can be divided into three sections.

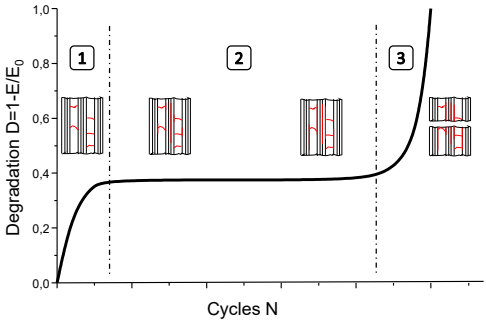

Figure 2.6: Schematic representation of the failure behaviour of a CFRP cross-ply laminate under cyclic loading.

In the first section, a stiffness decrease occurs in the range of 2-5 %. Transverse cracks initiate in the 90° and ±45° plies, and pre-damaged fibres fail. In the transition to section two, the curve flattens out. A constant crack density appears in the material [39, 64]. In the second section, the curve is approximately linear. The low gradient is due to the formation of the first small delaminations, which provide crack coupling and longitudinal cracks (splitting) in the 0° layers. If a specimen is loaded under tension, the 0°-layers carry most of the load. Due to Poisson's strain, contraction occurs within the 0° layers. This contraction is hindered by the 90° plies, which have a higher stiffness transverse to the load direction, leading to the transverse stresses and the longitudinal cracks. However, Schulte et al. have shown that the longitudinal cracks have almost no influence on the stiffness of the laminate [39]. In the third section, the degradation decreases very strongly over a few cycles, and the final failure occurs. The delaminations grow due to the applied load. New delaminations initiate at the interfaces between the transverse and longitudinal cracks. Cracks neighbouring the 0° layers increase the stress in the fibres by up to 8 %, which can cause them to break prematurely [39]. If the first fibres fail, the stress must be transferred to the neighbouring fibres until all fibres fail and a final fracture occurs. If compressive stresses

occur in addition to tensile stresses, the curve in the second section is steeper. The delaminations in the outer areas can cause buckling under compressive loading, which accelerates the growth of delamination [39, 41, 62].
In addition to the cyclic tests on undamaged specimens, the behaviour of damaged specimens due to, for example, low-velocity impacts is essential. Under tensile loads, impacts that cause inter-fibre fractures and delaminations have less influence. However, under compressive loads, buckling occurs from the first cycles, and degradation accelerates [28–30, 65–68]. As a result, the lifetime decreases with increasing impact damage [65]. Studies by Symons et al. and Rosenfeld et al. have shown that alternating tensile-compressive loading is particularly critical. As in addition to buckling under compressive loading, the inter-fibre fractures open and grow under tensile loading, resulting in new delaminations, which in turn can lead to further buckling under compressive loading [69, 70].

2.3 Constant-life diagram

To estimate the influence of different load ratios on the fatigue lifetime of a certain material for which no experimental data are available, constant-life diagrams (CLD) are a fast and powerful tool. Especially in fields where few fatigue investigations have been carried out, as is the case with Thin-Ply CFRP materials, CLDs represent an excellent first approximation. The main parameters defining a CLD are the tensile and compressive strength, the mean cyclic stress, the cyclic stress amplitude, and the load ratio R [71]. In Figure 2.7, the cyclic stress amplitude is plotted versus the mean cyclic stress. The diagram consists of three sectors, which describe the different load ratios for fatigue tests. Depending on the load ratio, the dominant loads are tensile or compressive forces. The load ratios to be investigated vary according to the chosen CLD theory. Since materials' failure behaviour under tensile and compressive loading is different, selecting a load ratio from each of the three sectors is advantageous.

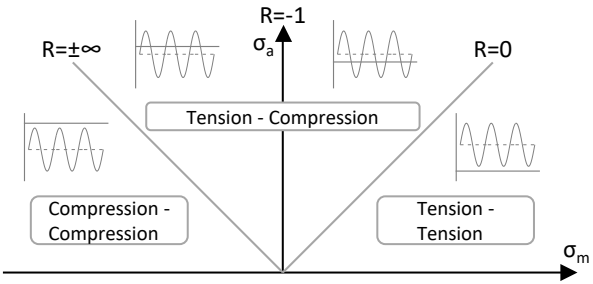

Figure 2.7: R-ratio in relation to mean cyclic stress and cyclic stress amplitude. Three sectors of fatigue testing, tension-tension, tension-compression and compression-compression.

Within a CLD, the interpolated measurement data of the S-N curves at different load ratios are presented. Figure 2.8 shows on the left-hand side a typical S-N curve. If a sample fails, the corresponding stress amplitude (Y-axis) is plotted over the number of cycles to failure (X-axis). A 50 % probability of failure is calculated from the data (black line). For calculation methods, reference should be made to the standard DIN 50100 [72]. A curve within the CLD relates to a specific number of cycles. In this example, a number of cycles of $5 \cdot 10^5$ cycles are chosen. Thus, the stress amplitude is determined according to the number of cycles using the 50 % probability (red dot, left diagram, Figure 2.8).
According to the respective load ratio, the stress amplitude in the CLD is plotted versus the mean stress (red dot, right diagram, Figure 2.8). The points are interpolated according to the chosen interpolation method at different load ratios and the ultimate tensile and compressive strength (left and right intersection with the X-axis). The designer can approximate the mechanical properties as a function of the load ratio from the CLD curves.

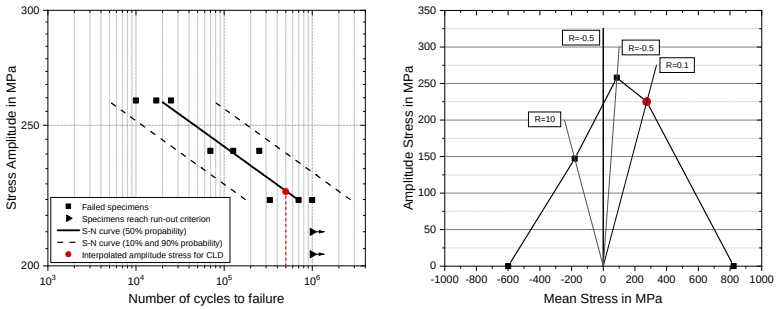

Figure 2.8: Left) S-N curve with a run-out criterion of 10^6 cycles; right) Constant-life diagram calculated using the linear interpolation method

Depending on the material behaviour, different interpolation approaches can be chosen. The simplest type of interpolation is the linear CLD model, which only requires one S-N curve with a load ratio of $R = -1$, but assumes that the material behaves the same under tensile and compressive loads [71]. Different approaches were proposed, which can be used depending on the examined material behaviour. The most commonly used non-linear interpolation approaches include Harris's CLD [73], Kawai's CLD [74], Boerstra's CLD [75], and Kassapoglou's CLD [76]. Within this thesis, the piecewise linear interpolation by Philippidis et al. [77] and a semi-empirical method by Harris et al. [73] are used.

The piecewise linear interpolation model requires a limited number of S-N curves and the ultimate tensile and compressive strength. The model interpolates linearly between the measured data in the $\sigma_\mathrm{m} - \sigma_\mathrm{a}$ plane. The more measurement data (R-ratios) are available, the more accurately the model can represent reality. As a rule, load ratios should be selected from all three sectors of the $\sigma_\mathrm{m} - \sigma_\mathrm{a}$ plane [71] (see Figure 2.7).

Philippidis et al. proposed an analytical description of the piecewise linear interpolation method for the individual regions of the CLD, enabling unknown

load ratios (R') to be calculated [77]. If R' is in the tensile-tensile region and between $R = 1$ (X-Axis) and the first known measured value ($R_{1\mathrm{TT}}$) counterclockwise, Equation 2.2 applies.

$$\sigma'_{\mathrm{a}} = \frac{UTS}{\frac{UTS}{\sigma_{\mathrm{a,1TT}}} + r' - r_{1\mathrm{TT}}} \tag{2.2}$$

σ'_{a} displays the interpolated and $\sigma_{\mathrm{a,1TT}}$ the experimental determined amplitude stress and UTS the ultimate tensile strength. The further parameters are calculated according by $r_{\mathrm{i}} = (1 + R_{\mathrm{i}})/(1 - R_{\mathrm{i}})$ and $r' = (1 + R')/(1 - R')$. In the first case, $R_{\mathrm{i}} = R_{1\mathrm{TT}}$ applies.
If R' is between two known R-ratios, R_{i} and $R_{\mathrm{i+1}}$, Equation 2.3 applies.

$$\sigma'_{\mathrm{a}} = \frac{\sigma_{\mathrm{a,i}} \cdot (r_{\mathrm{i}} - r_{\mathrm{i+1}})}{(r_{\mathrm{i}} - r') \cdot \frac{\sigma_{\mathrm{a,i}}}{\sigma_{\mathrm{a,i+1}}} + (r' - r_{\mathrm{i+1}})} \tag{2.3}$$

If R' is in compressive-compressive region and clockwise between $R = 1$ (X-Axis) and the first measured value in compressive region, $R_{1\mathrm{CC}}$, Equation 2.4 applies. UCS represent the ultimate compressive strength.

$$\sigma'_{\mathrm{a}} = \frac{UCS}{\frac{UCS}{\sigma_{\mathrm{a,1CC}}} - r' + r_{1\mathrm{CC}}} \tag{2.4}$$

In addition to the linear interpolation method, the semi-empirical model of Harris et al. is used in this thesis, which is based on investigations with carbon and glass fibre composites. [78–80]. The model is a kind of bell curve that reflects the material behaviour in the $\sigma_{\mathrm{m}} - \sigma_{\mathrm{a}}$ plane. Studies have shown that the behaviour of FRPs with brittle fibres can be reproduced well with the Harris model [78, 80]. The curve can be described using Equation 2.5.

$$a = f \cdot (1 - m)^{\mathrm{u}} \cdot (c + m)^{\mathrm{v}} \tag{2.5}$$

The parameters a, m and c are normalised stresses related to tensile strength. a represents the normalised stress amplitude, m the normalised mean stress and c the normalised compressive strength. The parameters f, u and v depend linearly on the logarithm of the fatigue life and are determined from the measured data. Initially, the model was developed for carbon/aramid hybrids, where $u = v = 1$ [78, 79]. However, it became apparent that the model needed to be more general to represent different composites. Beheshty and Harris [80] showed that the determination of the three parameters applies to a wide range of composites, especially CFRP composites. The parameters f, u and v can be determined from experimental data. For this, at least three S-N curves with different load ratios must be available, whereby these should be distributed on the $\sigma_{\mathrm{m}} - \sigma_{\mathrm{a}}$ plane.

$$f = A_1 \cdot log(n) + B_1 \tag{2.6}$$

$$u = A_2 \cdot log(n) + B_2 \tag{2.7}$$

$$v = A_3 \cdot log(n) + B_3 \tag{2.8}$$

The parameter f primarily determines the curve's height and is mainly determined by the relationship between compressive and tensile strength. The parameters u and v determine the shape of the sides of the curve. Since the parameter f has the most significant influence and depends on the accuracy of the measurement results, Harris et al. have introduced a simplification for the determination of f. For a lot of composites, the following applies in the first instance [78]:

$$f = A \cdot c^{-p} \tag{2.9}$$

A and p represent functions, which depend on log N. Experimental investigations have shown that in a first approximation $A = 0.71$ and $p = 1.05$ can be assumed. However, this must be decided depending on the material to be examined [78].

2.4 Thin-Ply carbon fibre reinforced polymers

One approach to increase the mechanical performance of FRPs is to reduce the layer thickness. Layer thicknesses below 100 µm are usually referred to as Thin-Ply layers. Commercially available are layer thicknesses up to 18 µm [8]. By using thinner layers, a large number of layers can be used for the same laminate thickness. The design space is increased, and the layer structure can be designed more load dependent [8, 9, 59, 81, 82].
One of the first Thin-Ply studies was conducted by Sihn et al. [5]. The results show significantly improved mechanical properties in contrast to thicker plies. Amacher et al. describe four scaling effects that explain the improved mechanical properties [8].

Probability of critical defects
The weakest link assumption implies that a body's strength depends on the probability of the occurrence of a critical defect. Assuming that the density of defects in a layer is independent of the layer thickness, the distance between defects should increase with thinner layers. Thus, the probability of a defect related to a local area decreases and the strength increases. A study by Sihn et al. [5] showed that the size effect does not significantly influence the strength, but according to Amacher et al., the effect cannot be ruled out.

Crack propagation controlled mechanisms

Linear elastic fracture mechanics (LEFM) implies that a body's strength is inversely proportional to the square root of the crack length. The assumption is that the dominant failure behaviour is intralaminar crack propagation. The maximum crack length is limited by reducing the ply thickness because the cracks are stopped at neighbouring layers with different fibre orientations. Therefore the maximum crack length is equal to the layer thickness. The assumption represents the analytical model of "in situ strength" by Camanho et al. [83].

Microstructure and processing

Previous studies show that laminate quality increases through the production process of thinner layers. Due to the rovings' spreading process, the fibres are distributed more homogeneously, and resin-rich areas are smaller, and their number is reduced. Furthermore, interlaminar residual stresses due to the thermal effects caused by the production process are lower [11, 84, 85].

Laminate scaling

If layers of the same orientation are combined to sub-laminates, the lay-up is referred to as block scaling $[0_m/45_m/90_m/\text{-}45_m]_s$. Block scaling laminates have similar mechanical properties as Thick-Ply laminates with the same ply thickness corresponding to the thickness of the sub-laminates. However, the superior laminate quality of Thin-Ply layers positively affects the mechanical properties [11]. If layers of different orientation are combined to sub-laminates, and these sub-laminates are repeated in the laminate structure, the lay-up is referred to as sub-laminate scaling $[0/45/90/\text{-}45]_{ns}$. The reduction of resulting layer thickness, thickness of adjacent layers with the same fibre orientation, results in a changed failure mechanism. Stresses at free edges are reduced, and delaminations are suppressed [11].

2.5 Failure mechanisms of Thin-Ply composites

The failure behaviour of a composite is highly dependent on the layer thickness. The failure mechanisms of undamaged samples change from complex delamination dominated to brittle failure. Pre-damage is reduced, resulting in a higher ultimate tensile and compressive strength for unnotched quasi-isotropic Thin-Ply specimens [5, 7, 8]. The different failure mechanisms of Thick- and Thin-Ply composites are schematically illustrated in Figure 2.9.

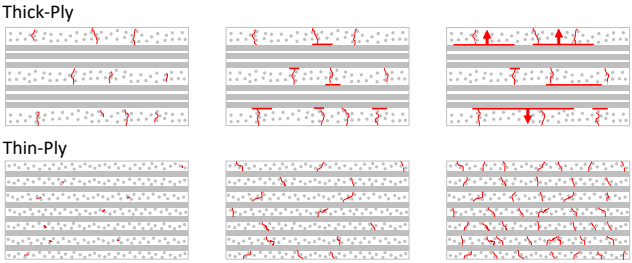

Figure 2.9: Failure mechanism of Thick- and Thin-Ply composites under tensile load from low (left) to high (right) stresses. Red lines represent damage such as inter-fibre fractures and delaminations.

At low stresses (left images 2.9), inter-fibre fractures already occur within the thicker 90 layers. With thinner layers, only microcracks are detectable. The formation of inter-fibre fractures decreases with decreasing layer thickness, as the transversal strength increases. Camanho et al. proposed an analytical model in 2006 that explains the change in the failure mechanism of Thin-Ply composites and is called „in situ strength“. The model has been investigated in detail in previous studies [20, 83, 86]. The in situ strength indicates that a layer embedded in a multi-directional laminate has a higher transverse strength than in an unidirectional laminate. Furthermore, the transverse tensile strength increases exponentially with decreasing layer thickness [83,

87, 88].

With increasing load (middle images 2.9), more inter-fibre fractures develop in the thick 90° plies. High interlaminar shear stresses occur at the interfaces between the plies at the crack tips, initiating delaminations. In the Thin-Ply composite (middle, bottom), on the other hand, only first inter-fibre fractures occur. Yokozeki et al. [7] showed by acoustic emission that the initiation of damage shifts to higher strains and thus higher stresses. Their length is limited to the thickness of the layers, as they are stopped at neighbouring layers. The interlaminar shear stresses in Thin-Ply laminates are insufficient to initiate delaminations; therefore, delaminations are suppressed. Even at higher stresses (right images 2.9), the interlaminar shear stresses are insufficient to initiate delaminations. The suppression of delaminations ensures that the stresses in the transverse layers are higher. Due to the high stresses, the crack density increases with decreasing layer thickness [7–9]. Between the thicker layers, the delaminations continue to grow until entire layers have separated from each other or the sample has failed completely.

A similar behaviour can be observed under cyclic load. Even at low cycle numbers, the first significant damage occurs in Thick-Ply composites, which is reflected in a decrease of the Young's modulus. The damage is matrix-dominant, such as inter-fibre fractures and delaminations. As under static load, these damages are suppressed by the increased transverse strength of Thin-Ply composites, which leads to an improved lifetime independent of the stress level [5, 8, 32, 89].

In addition to the higher number of layers, which results in higher residual stiffness under damage, the higher laminate quality positively affects performance under compressive load. Resin-rich regions and voids are smaller, and the fibres are more homogeneous distributed due to the spreading process [8, 9].

Failure mechanisms of notched Thin-Ply composites

In contrast to the unnotched samples, notched Thin-Ply specimens exhibit a lower open hole tensile strength. Under tensile loading of notched Thick-Ply laminates, fibre-matrix splitting occurs in the 0° layers. Local delaminations occur in the stress concentration area, which propagate through the laminate with increasing load. Delamination failure is the dominant failure mechanism in notched Thick-Ply laminates. The damage acts as a blunting mechanism of the stress concentration [12, 13, 58]. Due to the suppression of delaminations in notched Thin-Ply laminates, no crack blunting due to interlaminar damage occurs. Thus, no energy can be dissipated or stress diverted to adjacent areas, and the stress concentration leads to premature fibre failure [5, 8–10, 12].

Failure mechanisms of Thin-Ply composites under impact load

The failure behaviour during impact also changes with decreasing layer thickness. The damage patterns of Thick-Ply samples show inter-fibre fractures and delaminations and have the shape of a cone, as shown in section 2.2.1. In contrast, no inter-fibre fractures occur in Thin-Ply specimens due to the in situ strength [5, 8, 90]. As a result, a typical damage pattern of bending failure arises. Large delaminations characterise the damage pattern due to the propagation of a single or a few extended delaminations through the laminate. Depending on the stiffness of the laminate, fibre breaks on the specimen's backside [7, 8, 91, 92]. In their study, Amacher et al. have shown that intermediate ply laminates in particular exhibit mixed-mode failure and have the smallest damaged areas [8].

Bearing failure mechanisms of Thin-Ply composites

Load introduction by bolts is an essential aspect concerning the use of Thin-Ply as a primary structure. Studies by Amacher et al., Arteiro et al. and Camanho et al. have investigated Thin-Ply's bearing properties [8, 20, 21]. They demonstrated improved bearing performance compared to Thick-Ply composites. In the study by Amacher et al., an increase of 23 % in bearing strength under room conditions was observed [8]. In the case of Thick-Ply specimens, as already described in section 2.2.3, large delaminations occur, reducing the stiffness and causing final failure. With Thin-Ply specimens, initial damage is delayed, and the formation of delaminations is suppressed. Local shearing and crushing occurs in areas below the bolt and leading to a final failure [8, 9].
With regard to the bearing strength, it should also be mentioned that the increased bearing strength of Thin-Ply is higher under hot-wet conditions. Amacher et al. demonstrated an increase of 138 % in the bearing strength of Thin-Ply compared to Thick-Ply under hot-wet conditions. Under higher temperatures, the matrix properties are reduced and since the matrix dominating behaviour is the predominant failure mode for Thick-Ply, the reduction in strength is higher (72 %). In the case of Thin-Ply specimens, the bearing strength decreases by only 35 % [8].

2.6 Fibre metal laminates

2.6.1 Adhesion and adhesive bonding

The definition of adhesion varies in the literature. One accepted definition of adhesion was provided by Wu et al. [93]:

> "Adhesion refers to the state in which two dissimilar bodies are held together by intimate interfacial contact such that mechanical force or work can be transferred across the interface. The interfacial forces

holding the two phases together may arise from van der Waals forces, chemical bonding, or electrostatic attraction. Mechanical strength of the system is determined not only by the interfacial forces, but also by the mechanical properties of the interfacial zone and the two bulk phases.“

The definition suggests that the bonding strength depends on the properties of the bulk material, the interface between the adhesive and the adherend, and the adhesive properties. For this reason, a distinction is made between three different failure modes. In the case of cohesive failure, the crack does not extend along with the interface but through the bulk material or the adhesive. Both cases are shown in Figure 2.10 a) and b). If the crack extends along with the interface, it is an adhesive failure, see Figure 2.10 c) [94]. In addition to the three theoretically illustrated failure behaviours, combinations of the three failures often occur under real-life conditions.

Figure 2.10: Failure modes of a bonded joints: a) Cohesive failure in the adhesive layer; b) Cohesive failure in the adherend; c) Adhesive failure.

Therefore, the adhesive and cohesive failure must be taken into account in the design process of a bond. In total, five basic requirements, according to Petrie et al. [95], are needed for a successful bond:

1. The choice of adhesive
2. The design of the bond
3. The surface pre-treatment
4. The wetting of the surface
5. The bonding process itself

The bonding used in this thesis provides that the stainless steel foils are inserted as patches into the laminate and locally substitute the weaker 90° CFRP layers. For this reason, no external adhesive is needed, as the matrix itself acts as the adhesive. To ensure high laminate qualities, the laminates were cured with the stainless steel in an autoclave. Therefore, the bonding process corresponds to the curing process of the prepregs used. In order to increase the adhesion between the stainless steel foil and the matrix, it is essential to use a surface pre-treatment adapted to the materials used.
So-called adhesion theories are used in the literature to describe the adhesive force. Figure 2.11 shows a diagram of the adhesion theories, according to Bischof et al. [96, 97]. On the first level, a distinction is made between mechanical and specific adhesion.

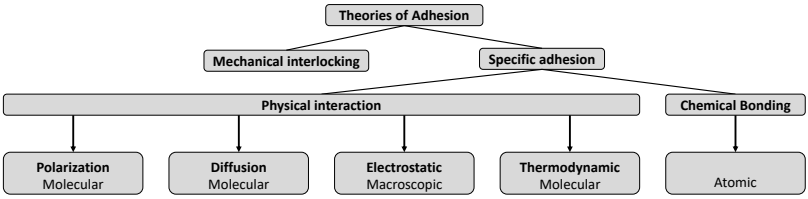

Figure 2.11: Adhesion theories according to Bischof et al. [96, 97].

Mechanical adhesion can increase adhesive strength through four factors. These are mechanical interlocking, cleaning the surfaces, forming reactive groups, and increasing the contact area [94]. However, increasing the contact area by roughening, combined with higher viscosity adhesives and thinner indentations, can lead to insufficient wetting, reducing the adhesive strength. Specific adhesion is subdivided into physical interactions and chemical reactions. The chemical reactions are chemical bonds between adhesive and adherent. Chemical adhesion includes primary valence bonds such as ionic, covalent and metallic bonds. They are characterised by short-range (0.15 to 0.3 nm) and high binding energies (63 to 1050 kJ/mol) (45,52). In metal-polymer bonds, according to Andrews et al. [98], covalent bonds can form

between the epoxy resin groups and the hydrated oxides of the metal surface during curing.
Physical interactions include the polarisation theory, the diffusion theory, the electrostatic theory, and the thermodynamic adhesion [96, 97].
The diffusion theory is only applied to bonds of metals when primers or similar coatings are used. According to it, the inter-diffusion of molecules builds up a boundary layer, which increases the energy to be introduced concerning a separation [94, 99].
The polarisation theory assumes that materials with opposite polarity or dipoles attract each other. In our case, the polymer's functional groups can develop dipole interactions with the oxide and hydroxy groups present on the metal surface. Furthermore, additional dipoles can be artificially induced via hydrogen bonds, increasing adhesion [99]. Electrostatic theory especially has an essential part in the field of metal bonding. Electron transfer between metal and adhesive due to unlike electronic band structures results in boundary layers between adhesive and adherent. Additional energy must be expended to separate the boundary layers [99].
According to thermodynamic theory, for successful wetting, the adhesive's surface energy must be less than the adherent's critical surface energy to be bonded. If this is not the case, successful wetting does not take place. Partial wetting effects that the other adhesion forces cannot work either. Therefore, wetting is an essential requirement for successful bonding [95].

2.6.2 Surface pre-treatment - state of the art

The performance of bonded joints is directly related to the selection and application of a suitable surface pre-treatment method. Depending on the adherent and the environmental conditions, different pre-treatment methods have to be chosen. The adhesion theories presented in section 2.6.1 serve as a basis for deciding which pre-treatment methods could be successful. Pre-treatment methods can remove potential weak interfaces, change the substrate topography, modify the substrate surface's chemistry, or combine

these mechanisms [100]. Concerning the use of FRP/metal hybrid structures, in most cases, a mechanically strong as well as fatigue and ageing resistant bond is required. Furthermore, especially when using carbon fibres and steel, contact corrosion has to be prevented, and primers that operate as insulators have to be used [99].
From the current state of the art, a wide range of pre-treatment methods for stainless steel exist. However, unfortunately, not all pre-treatment methods can be applied to thin stainless steel foils. Therefore a preselection was made to determine the methods used in this thesis. In the following, only the surface modifications applied in this thesis will be discussed. Additional literature is referred to other pre-treatment methods [101–104]. The surface pre-treatment methods used in this thesis are:

- Degreasing
- Abrasion
- Chemical pre-treatment
- Low-temperature plasma
- Sol-Gel process
- Combination of the methods

The first four surface pre-treatment methods are explained briefly below to provide a basic overview. The Sol-Gel process is described in more detail in the next section, as this has been selected as the pre-treatment method for the open hole tensile and bearing tests.

Degreasing
Cleaning the surfaces removes organic and inorganic impurities as well as low-molecular surface layers. Cleaning is usually not the sole surface modification and does not create a permanent bond [105]. Various solvents such as acetone (polar-aprotic) or isopropanol (polar-protic), or distilled water are used for cleaning. The cleaning agent must be chosen according to the sensitivity of the surface and the type of contamination. The most processes use a combination of different solvents [106].

Abrasion

Mechanical pre-treatment has several strategies to increase bonding strength. One strategy is to increase the surface area. Another strategy is that, depending on the morphology, form-fit joints can be shaped by cavities or undercuts. Furthermore, the mechanical pre-treatment removes the surface's top layer so that weaker layers such as oxides are removed before bonding [107, 108]. However, reactive groups can also be formed by mechanical treatment, which includes chemical bonds [99].

Chemical pre-treatment

Chemical pre-treatment removes particles or layers from the adhesive to change the surface morphology. At the same time, reactive groups are formed on the adhesive surface due to the etchant used, which form primary valence bonds with the adhesive. Depending on the adherent and the adhesive material, different etchants or combinations of these can be used [94].
Surface pre-treatment of stainless steel is possible, for example, using sulphuric acid, as iron and iron oxide are soluble. Due to the polycrystalline structure of stainless steel, the surface is not homogeneously removed, but a rough surface morphology is created. Anodic areas dissolve in the sulphuric acid, and the cathodic regions are areas of gas evolution. However, if the treatment time is too long, hydrogen embrittlement can occur, resulting in local weakening of the metal [101].

Low-temperature plasma

Low-temperature plasma treatment under vacuum is a standard pre-treatment process for polymers. The densities of positive and negative charges in the plasma are the same [101]. The charges are ions, radicals, atoms, and molecules [94]. When the charged particles hit the material's surface to be treated, they break or create functional groups. The functional groups form primary valence bonds with the adhesive during the bonding process. Brewes names

four mechanisms to increase adhesive strength through plasma treatment of polymers [100]:

- Removal of contaminants by ablation
- Crosslinking
- Grafting of monomers to a polymer surface
- Introduction of functional groups

2.6.3 Sol-Gel process

The Sol-Gel process is commonly used as a surface pre-treatment method for bonding metals in the aerospace industry. The process works with a wide range of metals such as aluminium, nickel, stainless steel and titanium [109, 110]. In addition to increasing the adhesion, the hybrid polymer layer serves as a corrosion protection layer [111–113]. In general, colloidal dispersions form from the sols, the precursor. The dispersion is applied to the surface by several methods. Usually, the application is made via airbrush or an immersion bath. When applied to the surface, the dispersion gels. Through drying and possible heat treatment, a hybrid polymer layer is formed [99, 114]. The chemical processes are shown as an example of a metallic alkoxide in Figure 2.12.

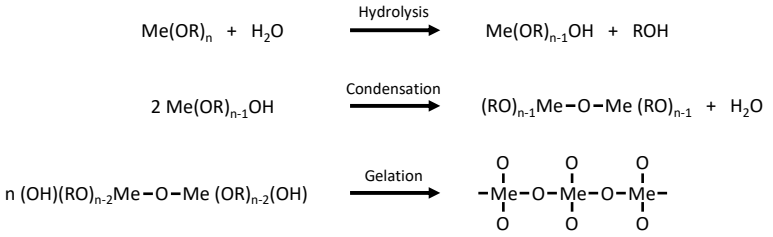

Figure 2.12: Reaction steps of the Sol-Gel process: hydrolysis, condensation and gelation.

Within this thesis, the so-called Boeing Sol-Gel process (Boegel EPII) is used. An aqueous solution with zirconium isopropoxide and a silane-based bonding agent is used. The zirconium creates covalent bonds with the metal oxide surface, and the silane-based bonding agent develops reactive organic groups for bonding with the polymer. The hybrid polymer layer consisting of zirconium oxides and bonding agent molecules can be described as a transition layer (organometallic layer) [99]. The typical structure of such a transition layer is shown in Figure 2.13 schematically.

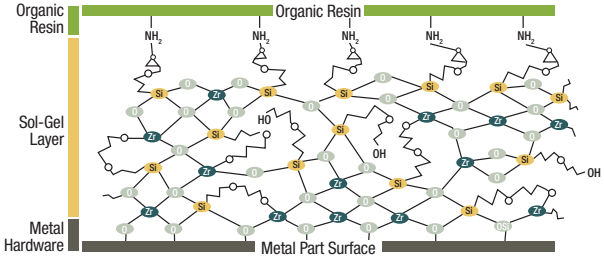

Figure 2.13: Chemical interaction at the interfaces between the metal surface, the Sol-Gel layer and the organic resin [115].

2.6.4 Hybrid fibre metal laminates - state of the art

Fibre-metal laminates are used to combine the beneficial properties of metallic and composite behaviour. Compared to fibre composites, the most significant advantages are quasi-ductile failure behaviour due to the plasticity of the steel foils, better energy absorption under tensile load, and better structural integrity in crash and impact tests [17, 24]. In addition to the static effects, hybridisation also improves the cyclic properties of the composite [116, 117]. In general, two different hybrid structures can be distinguished, see Figure 2.14.

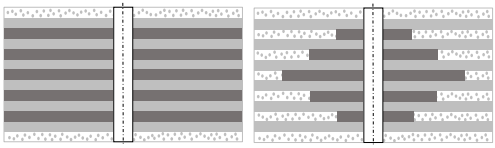

Figure 2.14: Two types of hybrid fibre metal laminate structures. The steel foils are represented in dark grey; left) Ply addition; right) Ply substitution.

"Ply addition" describes that the metal layers are used over the entire surface between and on the composite layers and influence the properties on the whole area, as is the case with GLARE, for example [118, 119]. In contrast, "ply substitution" means that weak composite layers are substituted locally by metals. Therefore only areas with, for example, high stress concentrations and load transfers are influenced [59, 120]. In previous studies, stress concentrations occurred in the transition zone (ply substitution) caused by the difference in stiffness between CFRP and metal. Therefore, the metal patches were arranged in a staircase design. The design distributes the increased stresses over a larger area, and locally the stress concentration decreases [59, 121]. The staircase design has also been used in other studies [22, 23, 122]. Keller et al. have summarised the most important parameters for designing a hybrid composite [123]:

- Layer thickness
- Mechanical properties of the used metal
- Lay-up
- Design of the transition zone
- Adhesion between metal and FRP

Titanium has been used as a reinforcing material in previous studies. Titanium offers the advantages of low density, low CTE (coefficient of thermal expansion), electrochemical compatibility with carbon fibres, and a small difference between the yield strain and the fracture strain of carbon fibres

[24, 124, 125].

Recent studies show that stainless steel is also a viable alternative to titanium. Stainless steel is characterised by its high tensile strength, high stiffness and good fatigue properties. Compared to titanium, only half the volume is needed for the same stiffness, which compensates for the higher density. Furthermore, the costs are an important factor. These are significantly lower for stainless steel [119, 120, 126].

A first study on the combination (ply addition) of Thin-Ply CFRP and stainless steel foils was published in 2015 by Masania et al. [119]. Masania et al. investigated the open hole tensile strength and bearing properties of Thin-Ply metal laminates with a CFRP layer and metal foil thickness of 30 µm and a steel volume content of 25 %. An increase of up to two times in the bearing strength was measured. The specific bearing strength, the bearing strength related to the density of the specimen, is lower than that of Thin-Ply without stainless steel. According to Studer et al. [120], it is sufficient to use local stainless steel reinforcements in areas of load introductions or high local stresses; this would decrease the component density.

Kötter et al. studied Thin-Ply CFRP with local stainless steel patches (ply substitution). This study shows that hybridisation of Thin-Ply CFRP samples with 25 % stainless steel patches increases the open hole tensile strength by up to 60 % compared to CFRP samples. Even when the strength is normalised to the density of the specimens, the OHT strength increases by up to 33 %. No improvement in OHT strength was observed for Thick-Ply hybrid samples, the laminates failed due to delamination. Thin-Ply hybrid and Thick-Ply hybrid samples with a steel content of 25 % showed no improvement in open-hole compressive strength. The specimens with the thin layers had a lot of buckling defects, which led to premature failure. The hybrid specimens with the thicker layers failed due to delamination [59].

A further benefit of hybridisation with metal foils is the possibility of detecting defects. Bosbach et al. have shown that delaminations during loading could be detected by measuring the capacitance between the metal layers [17].

3 Manufacturing methods

3.1 Materials

3.1.1 Carbon fibre reinforced polymers

Three different prepreg systems were used throughout this study. The specific properties regarding the systems are shown in Table 3.1. The prepreg system HexPly M21/35%/268/T800S from Hexcel, USA, developed for aircraft applications, was used to investigate the surface pre-treatment of stainless steel [127]. The resin M21 is a toughened epoxy resin with excellent damage tolerance properties [127]. The used carbon fibres were T800S intermediate modulus, high tensile strength fibres from Torayca, USA [128]. Open hole tensile and bearing tests were performed with a prepreg manufactured at the Industrial Technology Center of Fukui Prefecture, Japan. The epoxy resin system and the carbon fibres are from Mitsubishi Chemical Co., Ltd (see Table 3.1). The fibre areal weight of the prepreg system is 40 gsm. The resin system (jER828:jER1001 [129]) is characterised by its superior properties concerning the production of Thin-Ply laminates. For the production, commercially available 12k TR50S rovings were spread into a flat bundle by a spreading process using sub-atmospheric conditions [130]. A prepreg system from Northern Thin Ply Technology (NTPT) was used for the fatigue and fatigue after impact tests. Its superior properties characterise the toughened prepreg system TP 402 from NTPT, Switzerland [131], with regard to the production of thin layer thicknesses. According to the manufacturer, layer thicknesses of up to 18 µm can be produced. The prepregs from NTPT used

in this study have a fibre areal weight of 30, 60 and 120 gsm and the used carbon fibres were T700S standard modulus fibres from Torayca, USA [132].

Table 3.1: Overview of the prepreg systems used. M21 for the pre-treatment tests, ITCF for the fibre metal laminates and NTPT for the fatigue and fatigue after impact tests.

Prepreg system	**M21/ T800S**	**ITCF**	**NTPT**
Manufacturer	Hexcel	ITCF	NTPT
Carbon fibres	T800S	TR50S	T700S
	Toray	Mitsubishi	Toray
Resin system	M21	jER828:jER1001	ThinPreg 402
	Hexcel	(4:6) Mitsubishi	NTPT
Fibre volume content	56.6 %	50.0 %	55.0 %
Fibre areal weight	268 gsm	40 gsm	30, 60, 120 gsm

3.1.2 Stainless steel foil

The stainless steel foil (SF) used in this study is the austenitic chrome-nickel steel 1.4310 (X10CrNi18-8). Due to its good formability, thin foil thicknesses can be produced. In this thesis, the thickness of the foil was 30 and 150 µm for the foil tensile samples and for the surface pre-treatment samples and 40 and 160 µm for the open hole tensile and bearing tests. The 30 and 150 µm foil was produced by Precision Metals EU, Belgium and the 40 and 160 µm foils by h+s Präzisionsfolien GmbH, Germany. The alloy is characterised by its excellent machinability and high corrosion resistance. Both aspects are essential concerning the production of the specimens as well as durability. The technical data are listed in Table 3.2.

Table 3.2: Material properties of the stainless steel alloy 1.4310 (X10CrNi18-8) [133, 134].

Yield strength	Tensile strength	Young's modulus	Denisty	Thermal expansion
$\geq$ 210 MPa	500 - 700 MPa	200 GPa	7.9 kg/dm^3	16 $\cdot$ 10^{-6} K^{-1}

3.2 Manufacturing of CFRP/Hybrid laminates

The prepreg layers, which were cut by a CNC cutter (Aristomat TL 1625 from Aristo Graphic Systeme GmbH & Co. KG, Germany), were laminated by hand. To avoid air inclusions and compact the layers, an intermediate vacuum was applied to every fourth layer. The laminates were cured in an autoclave according to the individual manufacturer's specifications. In the case of fibre metal laminates, the steel foils are placed by hand during the lamination process after surface preparation. The different surface pre-treatment methods are presented in section 3.3. The thin steel foils were cut with a precision cutter for electronic boards, which results in no visible deformation at the edges of the foil patches. In addition to the stainless steel foils for the hybrid laminates, the stainless steel foils for tensile tests of the steel are also cut using the precision cutter.

3.3 Surface pre-treatment

Seven pre-treatment methods were tested to investigate the adhesion between stainless steel and matrix. A stainless steel foil cleaned by isopropyl alcohol was used as a reference. The isopropyl alcohol cleans the surface of residues such as contamination and lubricants but does not change the surface structure. Regarding the mechanical pre-treatment, roughening with an abrasive paper was chosen. Sandpaper increases the adhesive surface of the metal and removes possible impurities of the surface. A sandpaper with a 500-grain

size was used for pre-treatment. The roughening process was stopped as soon as a continuous film of water developed on the surface. In addition to the mechanical pre-treatments, surfaces were pre-treated by low-temperature plasma. This process is mostly used in the pre-treatment of polymers but will be examined here with metals. In addition to the low-temperature plasma treatment, a combination of abrasive paper and low-temperature plasma is also being investigated. The plasma process takes 5 min at 600 W and 300 mbar. The plasma system is the Smart Plasma 10 from Plasma Technology GmbH, Germany. Three acids were selected as chemical pre-treatment methods. The chemical etching process involves multiple steps. In the first step, the surfaces of the stainless-steel foil are cleaned and degreased with isopropyl alcohol to remove obvious surface contamination such as impurities, grease and oil. Afterwards, the surfaces are etched with the appropriate acid. The compositions of the acids used and the times and temperatures are shown in Table 3.3. The etching process increases the adhesive contact area by roughening the metal surface, removes weakly bonded oxides, and forms an oxide strongly bonded to the bulk of the part. Afterwards, the foils are rinsed with distilled water and, in the case of sulphuric acid and hydrofluoric acid, treated with a further solution. The second etch process remove carbon residues and passivate the surface with a solution of sulfuric acid and potassium dichromate. Finally, the surfaces are rinds and dried at 60 °C for 24 h. Common pre-treatment surface methods as phosphoric acid anodizing (PAA) or sulfuric acid-sodium dichromate etching are not environmentally friendly and were not investigated within this study. They are not economical for smaller series or repairs due to the high efforts involved [110].

Besides the acids, the surface pre-treatment agent AC-130-2 from 3M, USA, was also used. The pre-treatment system AC-130-2 is an aeronautically certified two-component Sol-Gel layer system, which increases the adhesion between metals (aluminium, nickel, stainless steel and titanium) and epoxy-based adhesive systems [109]. The Sol-Gel process consists of four steps.

Table 3.3: Process parameters of the etching methods used to pre-treat the stainless steel surface.

Process step	Acid	Temperature	Time
1	Sulphuric acid 30 %	60 °C	4 min
1	Hydrofluoric acid 4 %	50 °C	20 min
1	Hydrochloric acid 15 %	25 °C	5 min
2	25 pbw sulphuric acid + 2 pbw potassium dichromate	66 °C	5 min

1. Deoxidizing and extending the metal surface manually with abrasive paper (grain size 500).
2. Cleaning of the surface with acetone to remove all metal and abrasive parts and mixing the AC-130-2 Sol-Gel kit.
3. Applying the surface pre-treatment by immersion bath for 2 minutes.
4. Drying of the coated surface for at least 60 minutes.

3.4 Specimen preparation

All CFRP and fibre metal laminate samples were cut by corundum blade on a high precision saw (ATM Brillant 264 from QATM, Germany). After sawing, the samples were polished with sandpaper up to a grain size of 600 to suppress edge effects caused by surface roughness. In the case of the specimens for the static tensile and compressive tests, as well as the fatigue specimens, a finer grain size of 1200 was selected, as edge effects have a great influence, especially under fatigue loading. Before the respective tests, the samples were dried in a vacuum oven at 40 mbar and 40 °C for at least 48 h. The fatigue samples were acclimatised to the test conditions for at least 72 h.

3.4.1 Double cantilever beam (DCB)

The specimens are 125 mm long, 20 mm wide, 4.2 mm thick and the lay-up is $[0_8/SF/0_8]$. Aluminium elements (20 mm × 20 mm) are glued on the top and bottom of the specimen using an instant adhesive to introduce the load perpendicular to the delamination plane. The 63 mm long delamination is prepared using 10 µm thick PTFE foil, which simulates the 53 mm long initial delamination. One edge of the samples is coated with a thin white layer of acrylic paint, which allows the growth of delamination to be observed. On top of this white paint, markings are placed, which will enable the crack growth to be measured quantitatively. From the insert tip, the first 5 mm are marked every 1 mm and from the 5 to the 25 mm every 5 mm. The sample geometry is shown on the left-hand side of Figure 3.1.

3.4.2 End notched flexure (ENF)

The specimens are 160 mm long, 20 mm wide, 4.2 mm thick and the lay-up is $[0_8/SF/0_8]$. One edge of the samples is coated with a thin white layer of acrylic paint. Three marks are on the top of the white layer. They are 20, 30 and 40 mm away from the tip of the initial delamination. The initial 63 mm long delamination is prepared using 10 µm thick PTFE foil. The two marks at 20 and 40 mm are for the compliance calibration tests in front of the test to the final failure at 30 mm. The sample geometry is shown in the middle of Figure 3.1.

3.4.3 Interlaminar shear strength (ILSS)

The ILSS samples deviate from the standard sample geometry. The thickness is 4.2 mm. Based on the thickness, the length of the samples is 25 mm and the width 8 mm. The lay-up ($[0_8/SF/0_8]$) is identical to the DCB and ENF

samples. The sample geometry is shown on the right-hand side of Figure 3.1.

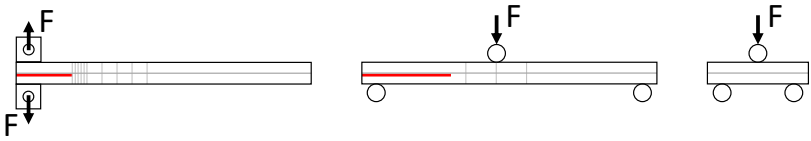

Figure 3.1: Specimen geometries of the DCB specimens on the left, the ENF specimens in the middle and the ILSS specimens on the right. The grey line represents the stainless steel foil and the red line the initial delamination by PTFE foil.

3.4.4 Open hole tension (OHT)

The open hole tensile samples are 250 mm long, 36 mm wide and 3.84 mm thick. In the middle of the sample is a hole with a diameter of 6.0 mm ± 0.6 mm. The hole was drilled using a diamond cutter with a diameter of 1.8 mm on a CNC milling machine (Isel EuroMod MP 30 from isel Germany AG, Germany). The stainless steel layers substitute the 90° CFRP layers local within the specimen. In the case of Thin-Ply, four different volume contents of stainless steel are tested. Due to the lower number of layers, two volume contents are tested in the case of Thick-Ply. If not all 90° layers are substituted by stainless steel due to the defined content, the outer layers are replaced (see Figure 3.2), as they will receive the most compressive stresses under bearing load. The steel foils are stepwise inserted along the length to avoid an abrupt change in stiffness. The minimum length of the stainless steel foil is 40 mm, and the maximum length is 65 mm. Near field strains are recorded via a digital image correlation system. For this purpose, a thin black and white speckle pattern of acrylic coating is sprayed onto the sample surface. Far field strain is recorded via strain gauges, which are glued outside the area with stainless steel. The investigated local volume steel contents with the

corresponding global densities of the samples and the lay-ups are shown in Table 3.4.

Table 3.4: Overview of the lay-ups and steel contents with regard to the open hole tensile and bearing tests (SF: Steel foil).

Local steel content	**Density in g/cm³**		**Lay-up**
	OHT	Bearing	
0.00 % (40 µm)	1.53	1.53	$[45/90/\text{-}45/0]_{12s}$
6.25 % (40 µm)	1.62	1.67	$[(45/SF/\text{-}45/0)_3/(45/90/\text{-}45/0)_9]_s$
12.5 % (40 µm)	1.70	1.80	$[(45/SF/\text{-}45/0)_6/(45/90/\text{-}45/0)_6]_s$
25.0 % (40 µm)	1.86	2.07	$[45/SF/\text{-}45/0]_{12s}$
0.00 % (160 µm)	1.53	1.53	$[45_4/90_4/\text{-}45_4/0_4]_{3s}$
25.0 % (160 µm)	1.88	2.12	$[45_4/SF/\text{-}45_4/0_4]_{3s}$

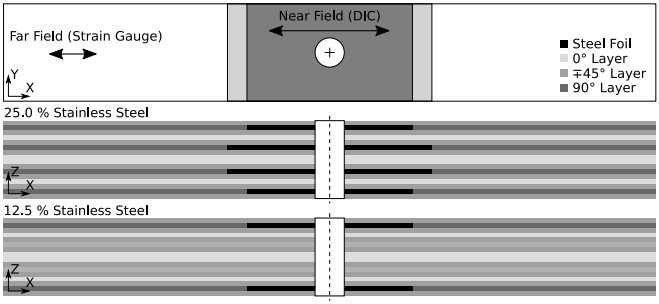

Figure 3.2: Geometry of the FML open hole tensile specimens. The near field strain was measured by a DIC system and the far field strain by strain gauges.

3.4.5 Bearing tests

The bearing samples are 135 mm long, 36 mm wide, 3.84 mm thick and the diameter of the hole is 6 mm (+0/-0.03) (see Figure 3.3). The hole was milled with the same parameters as the holes for the OHT samples. With regard to

the layer structures, please refer to section 3.4.4. The tested configurations are the same as for the OHT samples. The minimum length of the stainless steel foil is 38 mm, and the maximum length is 50.5 mm. The investigated local volume steel contents with the corresponding global densities of the samples and the lay-ups are shown in Table 3.4.

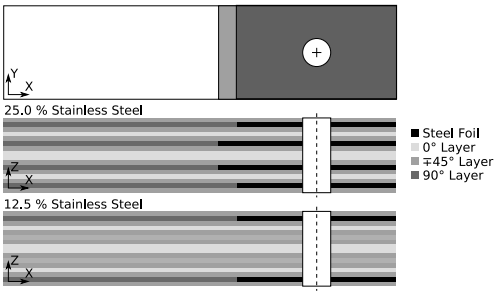

Figure 3.3: Geometry of the FML bearing specimens.

3.4.6 Static and fatigue tests

The lay-ups and specimen geometries for static and fatigue tests are based on the corresponding ASTM standards for static tensile (ASTM D3039-00 [135]) and compressive (ASTM D3410-03 [136]) tests. All tests were carried out with a quasi-isotropic lay-up ($[\text{-}45_\text{m}/90_\text{m}/45_\text{m}/0_\text{m}]_\text{ns}$). Table 3.5 shows the used lay-ups. The specimen dimensions for the related tests and standards are shown in Table 3.6.

Table 3.5: Laminate lay-ups of the static tensile and compressive, as well as fatigue and fatigue after impact (FAI) tests.

	Test method		
	Tension	Compression	Fatigue/FAI
30 gsm	$[45/90/\text{-}45/0]_{12s}$	$[45/90/\text{-}45/0]_{22s}$	$[45/90/\text{-}45/0]_{12s}$
60 gsm	$[45/90/\text{-}45/0]_{6s}$	$[45/90/\text{-}45/0]_{11s}$	$[45/90/\text{-}45/0]_{6s}$
120 gsm	$[45/90/\text{-}45/0]_{3s}$	$[45/90/\text{-}45/0]_{6s}$	$[45/90/\text{-}45/0]_{3s}$
240 gsm	$[45_2/90_2/\text{-}45_2/0_2]_s$	$[45_2/90_2/\text{-}45_2/0_2]_{3s}$	-
360 gsm	$[45_3/90_3/\text{-}45_3/0_3]_s$	$[45_3/90_3/\text{-}45_3/0_3]_{2s}$	$[45_3/90_3/\text{-}45_3/0_3]_s$

Table 3.6: Overview of the test specimen dimensions and load introduction elements (* The thickness of the 240 gsm samples was 1.92 mm due to the lay-up).

	Length [mm]	**Width** [mm]	**Thickness** [mm]	**Tab material**
Tension*	250	25	2.88	1 mm GFRP+ 1 mm Alu
Compression	130	25	5.28	2 mm GFRP
Fatigue (R=0.1, -0.5)	250	25	2.88	1 mm GFRP+ 1 mm Alu
Fatigue (R=10)	130	25	2.88	2 mm GFRP
FAI	250	36	2.88	-

If tabs were used, they were bonded to the laminate in a hot press under 20 kN pressure and 80 °C for 30 min. The 2-component adhesive UHU Endfest 300 from UHU, Germany was used as adhesive. Three different tab setups depending on the type of test were used. Both GFRP tabs are ±45° laminates and 1 or 2 mm thick. The aluminium tabs are 1 mm thick. The fracture patterns of the 30 gsm specimens under tensile-tensile load (R=0.1) showed a non-standard failure near the load introduction area, which required an adjustment of the specimen geometry. A dogbone specimen geometry with a constriction of 2 mm (width 21 mm) and a gauge length of 130 mm was

chosen. For the fatigue after impact specimens, a width of 36 mm was chosen so that the impact damage does not reach the specimens' edges. The number of samples tested is given in Table 3.7. Due to the non-standard failure near the load introduction, a higher number of specimens were tested at the lowest layer thickness under tensile-tensile and tensile-compressive loading.

Table 3.7: Number of tested samples for each ply thickness and load case.

	Fibre areal weight				
	30 gsm	60 gsm	120 gsm	240 gsm	360 gsm
Tension	7	6	6	6	5
Compression	6	6	6	6	5
Fatigue R=0.1	20	10	10	-	9
Fatigue R=-0.5	19	7	7	-	14
Fatigue R=10	10	13	10	-	7
FAI R=-0.5	8	6	8	-	5

4 Experimental methods

4.1 Quality assurance

After curing, the laminates are comprehensively examined to ensure their quality and tradability.. Ultrasound images were recorded to identify possible defects such as delaminations or contaminations. The ultrasound system used was the ultrasonic testing system USPC 3040 from Ingenieurbüro Dr. Hillger, Germany. The laminate quality in terms of resin-rich areas, void content and damage, was examined using micrographs. Samples are sawn using a precision saw (ATM Brilliant 220, QATM GmbH, Germany) and embedded in KEM 15+ cold embedding system based on methacrylate from QATM GmbH, Germany. Finally, the embedded samples were polished in several stages on a ATM Saphir 550 polishing machine (QATM GmbH, Germany) using sandpaper and diamond suspension. The final polishing was done with diamond suspension with a particle diameter of 1 µm. The micrographs were taken using a digital microscope (Keyence VHX-7000), the void content was determined, and possible defects were marked. The fibre volume content was determined according to the DIN EN 2564 standard [137] in the central laboratory of the Hamburg University of Technology. The test method concerns the determination of the mass difference of specimens before and after resin extraction by wet chemical methods with sulphuric acid. The quality tests involving micrographs and fibre volume content were carried out on randomly selected areas.

4.2 Mechanical tests

4.2.1 Tensile tests of stainless steel foils

The tensile tests of the stainless steel foils were carried out according to ASTM E345-16 [138]. The tests were performed on a ZwickRoell Z2.5 universal testing machine. The strains of the foils were recorded using a video extensometer and two measuring marks on the specimen surface. The tensile rates were selected as a function of the stress. Up to yield point the speed was 0.2 MPa/s and after yield point 1 MPa/s. The samples were tested until final failure.

4.2.2 Double cantilever beam (DCB)

The DCB tests were performed using a ZwickRoell Z010 universal testing machine according to the ASTM D5528-02 [139]. The crosshead speed was set to 2 mm/min, and the loads were applied using two aluminium blocks (20 mm × 20 mm) on the surface of the specimen. During the test, the load and the crack opening were recorded automatically, and the crack growth was recorded by an optical magnifier lamp (10x magnification). The tests were stopped after a crack growth of 25 mm.

4.2.3 End notched flexure (ENF)

The ENF tests were conducted on a ZwickRoell Z010 universal testing machine according to the ASTM D7905-14 [140]. The tests were displacement controlled with a crosshead speed of 0.5 mm/min, the unloading rate was 1.6 mm/min, and the load was applied using three stainless steel rolls. The diameter of the loading roller was d_1=12 mm and the diameter of the support rolls was d_2=10 mm with a nominal span length of 100 mm. During the test, the load and the displacement of the crosshead were recorded. The test was

stopped as soon as the maximum measured load had decreased by up to 30 %.

4.2.4 Interlaminar shear strength (ILSS)

The ILSS tests were carried out on a Z010 universal testing machine from ZwickRoell according to the ASTM D2344-00 [141]. The tests were displacement controlled with a crosshead speed of 1 mm/min, and the load was applied using three stainless steel rolls. The diameter of the loading roller was d_1=6 mm and the diameter of the support rolls was d_2=3 mm with a nominal span length of 17 mm. The test was stopped as soon as the maximum measured load had decreased by up to 30 %.

4.2.5 Open hole tension (OHT)

The OHT tests were performed according to ASTM D5766-02a [33] on a ZwickRoell Z400 universal testing machine. The specimens were clamped using mechanical wedge jaws. The tests were displacement controlled with a crosshead speed of 2 mm/min. To avoid the influence of the clamping system and the machine frame flexibility at high loads, the near field strain in the area of the hole was recorded by the 4M Digital Image Correlation Systems from GOM, Germany and the far field strain by strain gauges from Vishay Measurements, USA. For a more detailed investigation of the failure behaviour, micrographs were prepared by the same procedure as used for quality assurance (section 4.1).

4.2.6 Bearing strength

The bearing tests were carried out on a ZwickRoell Z400 universal testing machine according to ASTM D5961-01 [34]. The crosshead speed was set to 2 mm/min. One side of the specimen was clamped with a mechanical

wedge jaw. The bolts manufactured by Scholz Mechanik, Germany, are made of high-strength steel (HSS, EN ISO 4957 [142]) with a bending strength of 4050 MPa. The specimens were clamped with a torque of 6 Nm via two M6 washers (DIN 125, type B) with an inner diameter of 6.4 mm and an outer diameter of 12 mm. For a more detailed investigation of the failure behaviour, micrographs were prepared by the same procedure as used for quality assurance (section 4.1). Preliminary tests have shown that without clamping, the bolt fails. The displacements of the bolt clamping system and the specimen are evaluated using a DIC system. The DIC system used was the 4M Digital Image Correlation Systems from GOM, Germany. The calculation of the bearing strain $\varepsilon^{\mathrm{br}}$ is shown in Equation 4.1. δ_1 and δ_2 are the local displacements as it is shown in the schematic test setup in Figure 4.1. K is the calculation factor to distinguish single-shear from double-shear tests. For double-shear tests, the calculation factor K is 1.0 and for single-shear tests 2.0. d is the diameter of the hole.

$$\varepsilon^{\mathrm{br}} = \frac{(\delta_1 + \delta_2)/2}{K \cdot d} \tag{4.1}$$

The bearing strength σ^{br} is calculated according to Equation 4.2. P is the load, h is the specimen thickness, and k is the load per hole factor; 1.0 for single-fastener or pin tests and 2.0 for double-fastener tests.

$$\sigma^{\mathrm{br}} = \frac{P}{k \cdot D \cdot h} \tag{4.2}$$

4.2.7 Tensile tests

The tensile tests were carried out according to ASTM D3039-00 [135]. The tests were performed on a ZwickRoell universal testing machine Z100 and

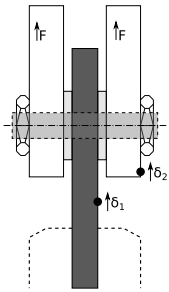

Figure 4.1: Schematic representation of the bearing test set-up.

servo-hydraulic clamping jaws clamp the specimens with 120 bar. Strains were recorded using MultiXtens Extensometer from ZwickRoell. In the case of the thickest layer thickness (360 gsm), the crosshead displacement had to be used for the strain measurement since strong delaminations of the outer layer. The tests were displacement control with a crosshead speed of 2 mm/min. An acoustic emission analysis is carried out to monitor the damage behaviour and detect the onset of the first significant damage. The used system is the MICRO-II from Physical Acoustic, USA. Two ceramic sensors with a diameter of 17 mm are clamped onto the sample surface. Ultrasonic gel, which is suitable for the frequencies used, is used as the transmission medium between the sensors and the sample surface.

4.2.8 Compressive tests

The compressive tests were carried out according to ASTM D3410-03 [136] performed on a ZwickRoell universal testing machine Z400 with a maximum load of 400 kN. IMA Dresden developed the used clamping system (HCCF) for compression tests of fibre reinforced composites at high compressive loads. With the HCCF hydraulic test fixture, one part of the compressive load is introduced via shear forces and one part via compressive forces over the specimen's end surface. The hydraulic pressure for the clamping jaws was

89 bar. The strain was measured with strain gauges from Vishay Precision Group, USA. To determine buckling, two strain gauges are used. The tests were displacement controlled with a crosshead speed of 2 mm/min.

4.2.9 Fatigue tests

The fatigue investigations were carried out on servo-hydraulic fatigue testing systems from Instron. Three load conditions were tested to analyse the influences of the layer thickness on the failure behaviour. Tensile-tensile tests were carried out at a load ratio of R=0.1. These tests were performed on an Instron 8800H2470 hydraulic system under stress control mode at 5 Hz with a maximum force of 100 kN and servo-hydraulic clamps. The pressure of the clamps was 120 bar. The displacement of the cylinder recorded the strains of the specimens. After 10^6 cycles, the tests stopped, and the sample is classified as a run-through. In order to record the damage development and delamination growth, X-ray images after $2 \cdot 10^3$ cycles were taken using X-ray faxitron 43885 (Rohde & Schwarz USA, Inc, USA). Zinc iodide is used as a contrast agent.
Composite structures should be designed for tensile loads, but compressive loads cannot be neglected entirely in most cases. For this reason, a load ratio of R=-0.5 was chosen. The tensile loads are twice as high as the compressive loads. For tensile-compressive tests, the Instron 8800H2470 under stress control mode at 5 Hz with a maximum force of 100 kN and the Instron 8802L2741 under stress control mode at 3 Hz with a maximum force of 250 kN were used. In both cases, servo-hydraulic clamps with a hydraulic pressure of 120 bar clamped the specimens. Anti-buckling supports were used during the tests to prevent buckling of the samples and premature failure (see Figure 4.2). The anti-buckling support shown on the left was used for the thicker layer thicknesses (60, 120 and 360 gsm). The design supports the specimen between the clamps. With the thinnest layer thickness (30 gsm), however, such anti-buckling support was not possible because of a failure in the area

between load introduction and anti-buckling support. In this case, the anti-buckling support designed for the fatigue after impact tests was used. This design is similar to the device used in the open hole compressive tests (ASTM D6484-04 [143]), with the difference that the load is applied via shear forces. The advantage of the anti-buckling support is that the specimen is supported along its entire length, reducing the probability of local buckling. The samples are not restrained laterally, so transverse contraction is not restricted. This design can reduce or avoid stress concentrations at the edges of the specimen. The R-ratio of the compressive-compressive tests was R=10. Due to the short gauge length of 10 mm and the thickness of 2.88 mm, no anti-buckling support was necessary. The specimens were tested on an Instron 8800H2470 servo-hydraulic testing system under stress control mode at 5 Hz with a maximum force of 100 kN and servo-hydraulic clamps with a pressure of 120 bar. The displacement of the cylinder determined the strain.

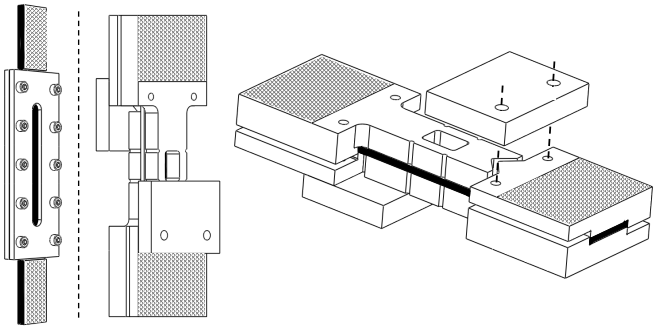

Figure 4.2: Illustration of the anti-buckling supports used for the fatigue and fatigue after impact tests. The left anti-buckling support is located between the tabs. The anti-buckling support in the two illustrations on the right supports the specimen along its entire length and clamps the specimen.

4.2.10 Impact

The drop weight impact tester was a FW Primus 1700 Plus from Coesfeld Materialtest, Germany. The impactor had a diameter of 16.0 mm ± 0.1 mm, a hardness between 60 and 62 HCR, a weight of 5.34 kg and an anti-rebound was used to prevent multiple impacts. The impact energy was 8 J. Impact energies of over 8 J lead in preliminary tests to delamination up to the edges of the sample. The clamping design of the support structure was based on the ASTM D7136-05 (Standard test method for measuring the damage resistance of a fibre-reinforced polymer matrix composite to a drop-weight impact event [144]). The cut-out dimensions were 27 mm × 60 mm. The ratio of length and width is identical to the standard. During the impact tests, four rubber tips restrain the specimen with a holding capacity of 1100 N. Mechanical end stops on the clamping device aligned the samples (see Figure 4.3).

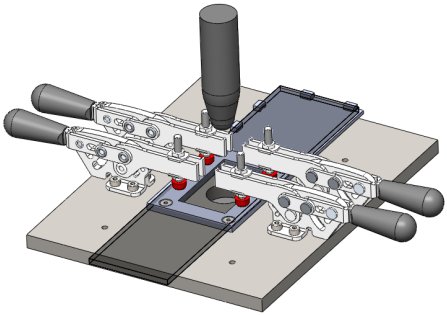

Figure 4.3: Clamping device for the fatigue after impact specimens for the impact tests.

4.2.11 Fatigue after impact

The fatigue after impact investigations were carried out on a servo-hydraulic system (8802L2741) from Instron under stress control mode at 3 Hz with

a maximum force of 250 kN. Servo-hydraulic clamps were used to fix the specimens. The pressure of the clamps was 120 bar. The displacement of the cylinder recorded the strains of the specimens. Tensile-compressive tests were carried out at a load ratio of R=-0.5. After 10^6 cycles, the tests stopped, and the sample is classified as a run-through.
The anti-buckling support was used to avoid buckling, which was also used in the tensile-compressive tests of the Thin-Ply specimens. The support is shown on the right-hand side in Figure 4.2. To analyse the occurring damage and possible growth, samples were tested with a maximum stress of 35 % UTS (undamaged) and stopped at 0, $5 \cdot 10^4$, $3 \cdot 10^5$ and $8 \cdot 10^5$ cycles and examined using computed tomography. The system used is a CT-Alpha device from Procon X-Ray, Germany. The measurements of the damaged sample regions were taken in axial and helical mode with an x-ray tube voltage of 65 kV and a voxel size of 27.3 and 24.3 µm, respectively. The helical scan mode was applied to samples with a large estimated damage area to capture the complete damaged area while maintaining a small voxel size. The visualisation of the volume data, i.e. evaluation and graphical representation of impact damage as well as the damage progression according to the respective load cycles was done with the Volume Graphics VGSTUDIO MAX 3.3 software.

5 Results and discussion

5.1 FML Thin-Ply

5.1.1 Tensile tests of stainless steel foil

Two exemplary stress-strain curves of the stainless steel foil tensile tests are shown in Figure 5.1. The thin foil with a thickness of 30 µm is shown in blue, and the thicker foil with a thickness of 150 µm is shown in black.

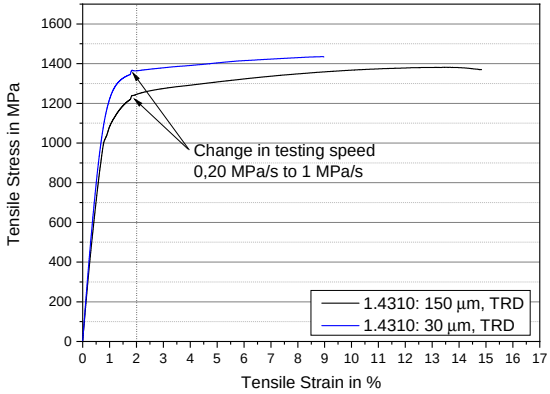

Figure 5.1: Stress-strain curves of stainless steel foil tensile tests. The samples are loaded transverse to the rolling direction (TRD)

The results of the tensile tests show no differences in the Young's modulus. But at higher stresses, the yield strength of the thinner foils is significantly higher. The yield strength of the thin foil loaded in rolling direction (RD) is 27.1 %, and loaded transverse to the rolling direction (TRD) 18.9 % higher than for the thick foils. The steps in the curves at about 1.9 % strain result from the change in the test speed. The characteristic of the curves of the thin RD and TRD foils do not differ. But the yield strength of the RD specimens is slightly higher. For the thick foils, no difference was observed. Table 5.1 shows an overview of the results.
The increased yield strength can be explained by strain hardening of the metal foils. The deformation (rolling) of the metal affects the micro-structure and introduces imperfections. The structural changes increase the probability that the imperfections will influence each other under load. As a result, more energy has to be applied for deformation and the yield strength increases. [145].

Table 5.1: Measured mechanical properties of stainless steel (1.4310) foils (ASTM E345-16 [138]); RD: rolling direction; TRD: transverse rolling direction.

Steel Foil		Yield Strength in MPa	Tensile Strength in MPa	Young's Modulus in GPa
30 µm	RD	1273.77 ± 85.79	1347.31 ± 52.65	150.11 ± 13.62
	TRD	1121.71 ± 26.93	1410.22 ± 30.78	172.62 ± 2.66
150 µm	RD	1002.21 ± 69.91	1337.75 ± 71.13	152.72 ± 4.31
	TRD	943.43 ± 55.05	1371.27 ± 8.32	157.18 ± 1.48

5.1.2 Interlaminar shear strength (ILSS)

It is difficult to compare the results of the specimens with and without stainless steel because ILSS samples with stainless steel do not have a symmetrical lay-up and, therefore, cannot be regarded as ideal specimens. The lower and upper parts of the specimen have different bending stiffnesses. However, the pre-treatment methods can be compared, and significant differences between the pre-treatments can be seen. A comparison reveals that the interlaminar shear strength of the specimen pre-treated with abrasive paper and AC-130-2 is most pronounced. Figure 5.2 shows the results of the ILSS tests. CFRP without stainless steel foil reaches 89.47 MPa, which is only 0.53 MPa below the value specified by the manufacturer Hexcel. From the results, it follows that due to the high interlaminar shear strength and the low standard deviation, the Sol-Gel process with the combination between abrasive paper and AC-130-2 surface pre-treatment system from 3M, USA is the most suitable pre-treatment method for stainless steel - CFRP hybrid laminates.

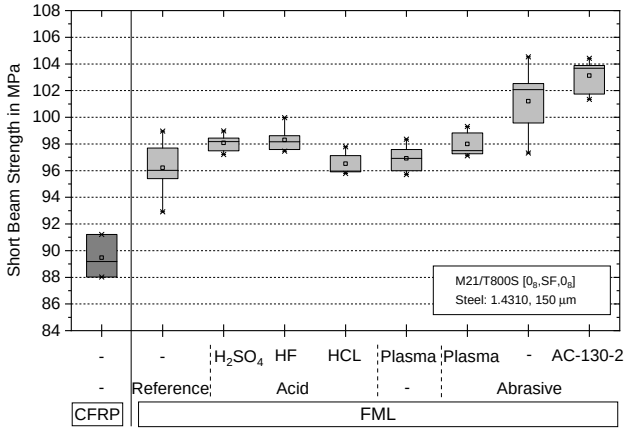

Figure 5.2: Interlaminar shear strengths (ILSSs) of the tested surface pre-treatments of the stainless steel foils.

Figure 5.3 shows scanning electron microscope (SEM) images of the surface of pre-treated stainless steel foils. It is noticeable that the etched surfaces have a fine structured surface, which in turn indicates theoretically good adhesion. Since the Sol-Gel process merely forms an intermediate chemical film on the stainless steel surface and thus does not cause any geometric changes to the surface, no difference can be detected between the surfaces of the samples ground and those ground and treated with AC-130-2 using SEM. The ground surface has a significantly higher roughness. Due to this, the crack or delamination must additionally move perpendicular to the sample plain and more energy is required to grow the damage.

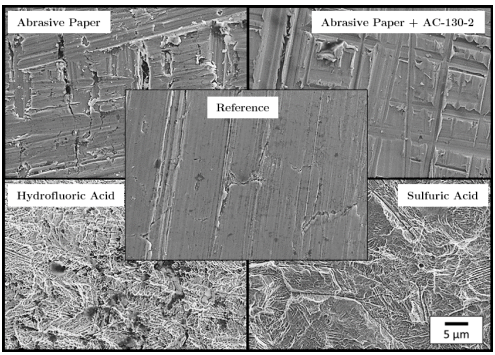

Figure 5.3: Scanning electron microscope images of the pre-treated stainless steel surfaces.

5.1.3 Double cantilever beam (DCB)

Figure 5.4 shows the results of the Mode I tests. A sample without stainless steel is presented in dark grey on the left. To the right is the FML reference sample where the stainless steel was cleaned with isopropanol. The energy release rate does not differ from that without stainless steel. The acids and the specimens pre-treated with abrasive paper show an improvement compared to the FML reference sample. Only the samples pre-treated with

low-temperature plasma show a significant reduction. Some specimens already separated when sawing or clamping the sample. A kind of hydrophobic surface has occurred due to the pre-treatment, which makes adhesion more difficult. With regard to the load-crack opening curves, there are no significant differences in the qualitative curves between the FML samples. All FML samples show a significant decrease after crack initiation, resulting in unstable crack growth for several millimetres. However, after the decrease, the energy release rates increase until they reach a constant value due to fibre bridging and crack propagation.

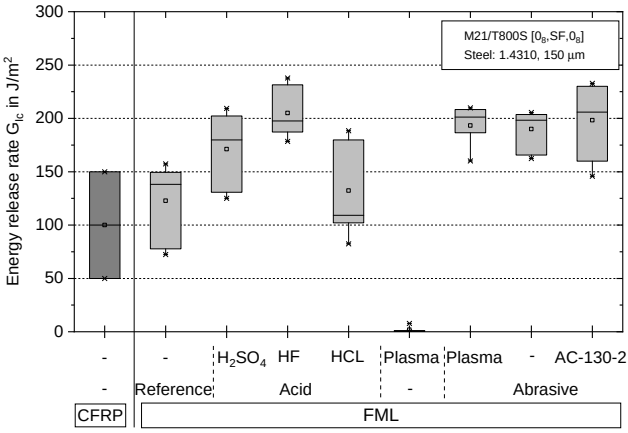

Figure 5.4: Influence of surface pre-treatment on the energy release rate under Mode I loading (Double Cantilever Beam - DCB).

The increase in the energy release rate can also be seen in the fracture patterns. At the beginning of the crack growth, the crack starts at the interface between stainless steel foil and CFRP. As shown in Figure 5.5, an adhesive failure occurs on the first millimetres, which changes to a cohesive failure with increasing crack length. The crack moves upwards into the CFRP sample.

Except for those treated with plasma, the fracture patterns of all specimens show a similar failure behaviour.

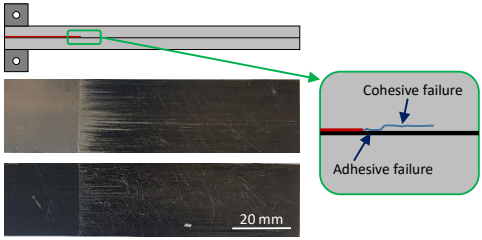

Figure 5.5: Fracture pattern and crack growth of a DCB specimen. The golden surface is the pre-treated metal surface.

5.1.4 End notched flexure (ENF)

The energy release rate under Mode II loading is presented in Figure 5.6. As in the DCB tests, the reference sample without stainless steel is shown in dark grey. All results are equal to or higher under Mode II loading than the reference and showed unstable crack growth. Again, the samples pre-treated only by low-temperature plasma have the lowest release rates. In contrast to the Mode I tests, there are significant differences between the other investigated configurations. The hydrofluoric acid, hydrochloric acid and the samples treated with abrasive paper with and without plasma treatment show similar release rates in the range between 1881 and 1964 J/m^2. The pre-treatment with sulphuric acid, on the other hand, shows higher energies. These are on average 2101 J/m^2. The highest energy release rates are achieved with abrasive paper and Sol-Gel pre-treatment. The average values measured are 2353 J/m^2.

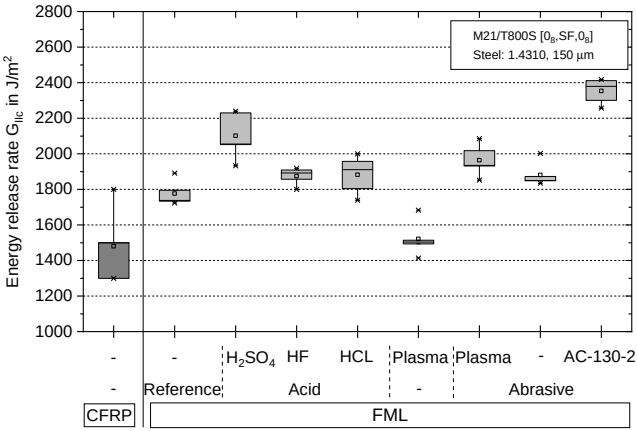

Figure 5.6: Influence of surface pre-treatment on the energy release rate under Mode II loading (End notched flexure - ENF).

The results show that a coarser roughness has advantages concerning Mode II loadings. Due to the roughness, a type of form-locking connection is achieved, which provides additional resistance to unstable crack growth initiation. In the case of samples pre-treated using the Sol-Gel process, there is a combination of two adhesion theories. On the one hand, the surfaces are ground, which leads to mechanical adhesion and, at the same time, chemical adhesion is generated due to the Sol-Gel layer between the two adherends. Both add up to an increased fracture toughness under Mode II. The fracture patterns show no difference between the pre-treatment methods and look like the DCB fracture surfaces, see Figure 5.5.

5.1.5 Open hole tension (OHT)

Figure 5.7 shows the results of the open hole tensile tests. The strength is illustrated in blue, and the specific strength in grey. The specific strength represents the ratio of the strength and the global density of the sample. Therefore, Thick-Ply samples with a local steel content of 25 % have a density of 1.88 g/cm^3 in contrast to the reference samples with a density of 1.53 g/cm^3. The corresponding densities of the samples are summarised in Table 3.4. The open hole tensile strength of the Thin-Ply samples recorded a 9 % lower strength than the Thick-Ply specimens. The results correspond to other studies investigating the OHT strength concerning the layer thickness [5, 8, 59]. Amacher et al. showed that initial damage in quasi-isotropic material shifts to higher strains with decreasing layer thickness. The onset of damage increased from 255 MPa for Thick-Ply specimens to 352 MPa for Thin-Ply specimens. The dominant failure mechanism changes from delamination dominated failure to a brittle failure mode from Thick- to Thin-Ply. Fibre matrix splitting in the 0° plies and localised delaminations at the hole can occur and act as a notch blunting mechanism in Thick-Ply laminates [13, 58]. The brittle behaviour of the Thin-Ply laminates inhibits notch blunting, and stresses at the notch can not be deflected to neighbouring areas and leads to premature failure [5, 8, 10].

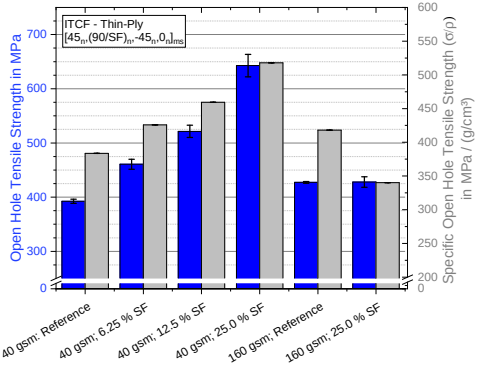

Figure 5.7: Open hole tensile strength (blue) and density specific open hole tensile strength (grey) of CFRP and CFRP fibre metal laminates.

The ultimate strength increases significantly with increasing steel content. With a local steel content of 25 %, the strength rises by 64 %, and even the specific strength rises by up to 36 %. Due to the hybridisation, the notch sensitivity decreases with an increase in steel content. The reduction in notch sensitivity is expressed in a decreasing notched strength reduction ratio (NSR). The NSR indicates the ratio between the notched strengths σ_{UNT} and the middle stress in the net section σ_{net}. The stress reduction ratio is calculated from the OHT strength σ_{OHT}, the ultimate tensile strength of unnotched samples σ_{UNT}, the specimen width w and the hole diameter d, see Equation 5.1 [10].

$$NSR = \frac{\sigma_{\mathrm{UNT}}}{\sigma_{\mathrm{net}}} = \frac{\sigma_{\mathrm{UNT}}}{\sigma_{\mathrm{OHT}}/(1 - \frac{d}{w})} \tag{5.1}$$

A value of nearly one indicates that the stress concentration has only a minimal impact on the strength, whereas higher values indicate high sensitivity to

stress concentrations. The measured values are shown in Table 5.2. It can be seen that the NSR decreases with increasing steel content, thus reducing the susceptibility to stress concentrations. In the case of the Thin-Ply FML samples with a steel content of 25 %, the NSR value is 1.18. As a result, areas with high-stress concentrations have only a small influence, and no thickening or design changes need to be made. The local hybridisation of the material avoids the influence of stress concentrations in thin-layer laminates so that the thin layers' potential can be exploited. The right bars of Figure 5.7 displays the results of the Thick-Ply samples with a local steel content of 25 %. A decrease in strength is shown in contrast to the Thin-Ply samples with 25 % steel content. The lower strength can be explained by the formation of delaminations between the metal layers and the matrix. Due to the higher shear stresses between the layers compared to Thin-Ply, the chosen surface pre-treatment is not sufficient, and delaminations are formed. Higher shear stresses result partly from the external mechanical loads and partly from the laminate residual stresses due to the large difference in thermal expansion coefficient. This consideration favours the formation of delamination. The initiation of delaminations can be seen in the stress-strain diagram (Figure 5.8) by a decrease in stiffness at about 340 MPa. One representative curve is shown for each configuration.

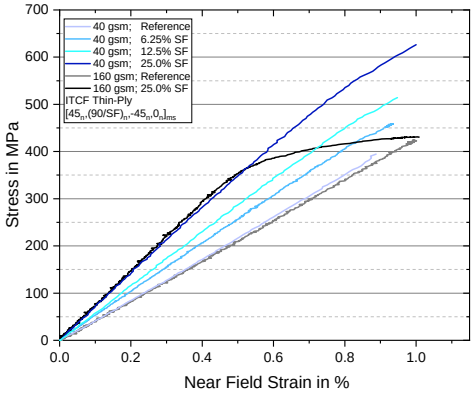

Figure 5.8: Stress-Strain diagram of the open hole tensile tests. The near field strain was recorded by DIC.

Table 5.2: Notched strength reduction ratio of the Thin- and Thick-Ply FML samples.

Fibre areal weight	Steel foil content	Strength in MPa Unnotched	OHT	NSR
40 gsm	0.00 %	911.97 ± 34.43	392.41 ± 3.84	1.94
40 gsm	6.25 %		460.78 ± 9.23	1.65
40 gsm	12.5 %		521.41 ± 11.25	1.46
40 gsm	25.0 %		642.78 ± 20.67	1.18
160 gsm	0.00 %	857.21 ± 11.06	427.27 ± 1.67	1.67
160 gsm	25.0 %		428.02 ± 9.70	1.67

The near field strain is plotted on the abscissa, which was obtained using the digital image correlation system. Near field strain was recorded over a length of 35 mm, so that the area with the maximum stainless steel content is measured. The measuring field is on the left-hand side of the hole and was chosen to ensure that local effects of the hole have no influence. Except for the Thick-Ply specimen with a local steel content of 25 %, all specimens

exhibit brittle failure and no major significant pre-damage. The local steel content can explain the difference in the stiffness. The steel layers substitute 90° CFRP layers, which have a lower tensile stiffness than the steel foil. The measured stiffnesses correspond to the theoretically calculated stiffnesses (E) if the rule of mixture (Equation 5.2) and the local steel content (ψ) are used. The stiffnesses of the individual materials is based on tensile tests for quasi-isotropic CFRP samples according to the ASTM D3039 [135] and tensile tests for the steel foil according to the ASTM E345-16 [138]. The measured and calculated stiffnesses are shown in Table 5.3.

$$E = E_{\mathrm{SF}} \cdot \psi + E_{\mathrm{CFRP}} \cdot (1 - \psi) \tag{5.2}$$

The far field strain was recorded outside the local hybridisation area using strain gauges, and the stiffnesses were determined. As expected, no far field stiffness differences between the configurations can be observed since the stiffness is influenced by the fibres and resin and not by the layer thickness. The stiffness is equivalent to the near field stiffness of the notched reference samples.

Table 5.3: Theoretical and measured stiffness of the hybrid area. The stiffnesses of the reference samples (italics) were determined by measurements according to ASTM D3039.

Configuration (SF: Steel Foil)	Measured Stiffness in GPa	Theoretical Stiffness in GPa
40 gsm	43.57 ± 0.91	*47.00 ± 0.67*
40 gsm; 6.25 % SF	51.38 ± 0.39	50.23
40 gsm; 12.5 % SF	57.00 ± 1.04	56.89
40 gsm; 25.0 % SF	69.43 ± 0.35	70.20
160 gsm	42.70 ± 0.37	*47.87 ± 1.49*
160 gsm; 25.0 % SF	74.13 ± 4.06	70.20

The DIC images in Figure 5.9 and Figure 5.10 show the surface strains of the top 45° layer in tensile direction. The DIC images of Figure 5.9 were taken at a load of 50 kN. Except for the right specimen (Thick-Ply, 25 % SF), all samples show a typical stress pattern near the hole for quasi-isotropic open hole tensile specimens. A stress concentration propagates from the hole in ±45°, furthermore above and below the hole, a local stress minimum appears. The images show that the steel foils reduce the stress of the top 45° layer. As the steel content increases, the local stress decreases. Furthermore, the Thick-Ply specimens with 25 % stainless steel show a high stress concentration at the transition area. For the Thin-Ply specimens with the same steel content, the transition area's stress concentration is significantly lower. Due to the high number of layers, the transition zone can be distributed over a larger area and thus, the local stress concentration can be reduced.

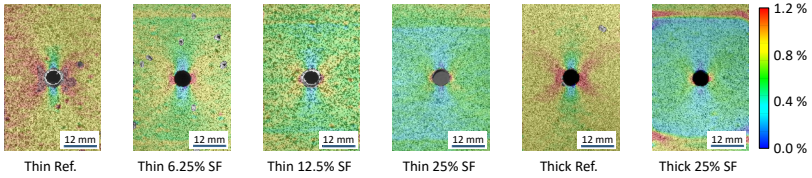

Figure 5.9: Strain in tensile direction at an applied tensile load of 50 kN, recorded by a DIC system.

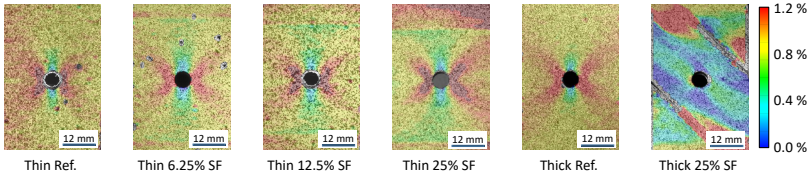

Figure 5.10: Strain in tensile direction shortly before final failure recorded by a DIC system.

Due to the continuous recording of the strain during tests, the images of Figure 5.10 display the specimens right before final failure. The images show that with increasing steel content (Thin- and Thick-Ply), the transition zone between CFRP and stainless steel is more clearly visible and the stress concentrations at the transition zone increase. Thus, the transition zone and the hole represent a second critical area concerning specimen failure. Figure 5.11 illustrates two curves, representing the strain in tensile direction as a function of the position. The position data is a vertical section through the sample, where 0 mm represents the centre of the sample, i.e. the centre of the hole (see Figure 5.11, top right, red line). The strains in the diagram belong to the far field tensile stress of 350 MPa at which delamination growth initiates in the hybrid Thick-Ply specimens. The strain curve (black) of the Thick-Ply specimen with a local steel content of 25 % shows two strong stress peaks symmetrical to the middle. These are located at the transition between the outer metal layers and the corresponding 90° CFRP layers. The local increase of stress initiates delamination growth and results in premature failure. In the case of the hybrid Thin-Ply specimens with a steel content of 25 % (blue), no strong localised stress increase is observable. Due to the low layer thickness, more metal layers are required, which in turn can be distributed stepwise more smoothly. The stepwise arrangement ensures that the stress increase is distributed over a larger area, and therefore the local stress concentrations decreased. The specimen fails at the hole, as do the reference specimens.

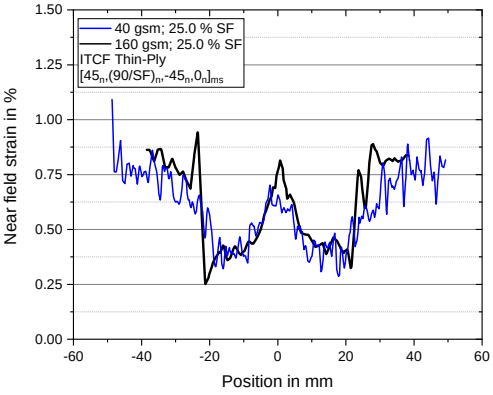

Figure 5.11: Near field strain in tensile direction as a function of the position on the specimen.

In addition to the DIC images, micrographs of the fracture surfaces of the specimens were produced. The images a) to d) of Figure 5.12 show micrographs of Thin-Ply specimens next to the hole. The micrographs demonstrate the brittle failure behaviour as the curves of the stress-strain diagram. Especially the Thin-Ply specimen without stainless steel foil (Figure 5.12 a)) shows a very straight fracture surface. Areas with stainless steel foils show a rougher fracture surface. The length of the fracture surface increases significantly. Figures 5.12 e) and 5.12 f) show detailed images of the fracture edges. An explanation for the higher fracture surfaces in the hybrid areas is the higher fracture strain and plastic deformation of the stainless steel. Due to the higher strains, more inter-fibre fractures in the CFRP layers occur before ultimate failure. These fractures do not always occur at the same location but are statistically distributed. Right before ultimate failure, the individual layers are pulled out, similar to the pull-out of fibres. This ensures that additional energy is dissipated and the open hole tensile strength increases. A characteristic of localised high plastic strains in metals is the fracture angle of the metal (see Figure 5.12, f)).

In order to examine the inter-fibre fractures more precisely, samples were loaded up to a maximum stress of 95 % of the ultimate strength, and further micrographs were prepared. These are shown in Figure 5.12 g) and 5.12 h). However, no damage to the material has yet been detected. Nevertheless, it can be seen that no resin-rich regions or voids are introduced into the material due to the introduction of metal layers.
Furthermore, there are no delaminations in the laminate between the metal and the CFRP due to thermal stresses. The fracture patterns of the micrographs exhibit delaminations on the outer metal layers. However, since DIC detected no deformation perpendicular to the specimen's surface, the outside delaminations result from the compressive stresses occurring within the specimen after the final fracture.

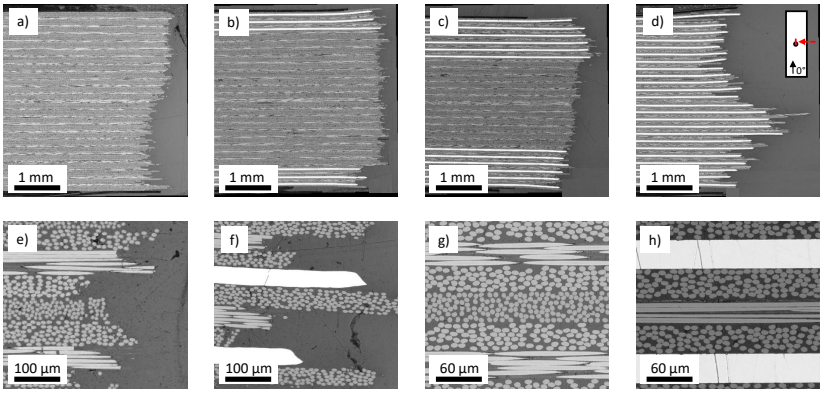

Figure 5.12: a) to f): Micrographs of the fracture surfaces of the open hole tensile specimens with increasing steel content; g) and h): Micrographs of two specimens loaded to 95 % of the maximum strength.

5.1.6 Bearing strength

In the following section, the results from the bearing tests are presented. Figure 5.13 summarizes the bearing strengths of the Thin- and Thick-Ply hybrid samples. As with the open hole tensile tests, three samples were tested per configuration since the results of the first tests showed a significant difference. Higher bearing strengths are achieved with decreasing layer thickness. The bearing strength increases by 15.3 % from 849.85 MPa (Thick-Ply) to 979.61 MPa (Thin-Ply) with a reduction of the area weight from 160 gsm to 40 gsm. Previous studies by Masania et al. and Amacher et al. show that the use of thin layers influences the bearing damage mechanism [8, 119]. The onset of first damage shifts to higher stresses and strains, and the initiation and propagation of delaminations, as well as matrix cracks, are suppressed. Furthermore, the intra-laminar shear stresses are lower due to the thin layer thicknesses and according to Garbo et al. [146], the lower shear stresses result in a delay in the initiation of damage mechanisms such as matrix cracks, fibre kinking and through-thickness shear cracking. Which, as a result, increases the bearing strength. However, progressive behaviour is no longer present, and the stress reduction after initial damage is extensive. For safety-relevant components, such as in aircraft structures, this is particularly critical [8, 20, 147].

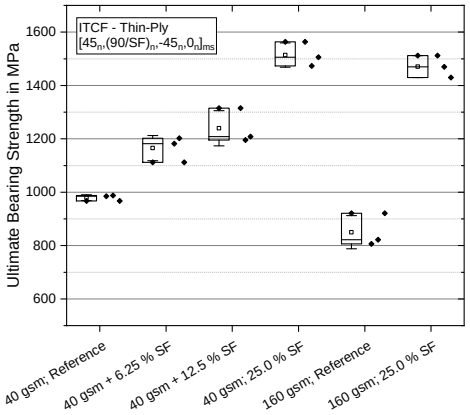

Figure 5.13: Results of the maximum bearing strength regarding layer thickness and steel content.

The micrographs in Figure 5.14 show the damage pattern of tested and embedded samples. Figure 5.14 shows overview images of the loading area of thin layer (a - c) and thick layer (d - f) specimens. In the case of Thin-Ply specimens, fewer delaminations occur, and the samples show less damage after loading. Noticeable for the thin layer thicknesses are the fibre breakage within the 0° layers (Figure 5.14 b) and global kink bands (Figure 5.14 c), which increase from the centre outwards. The clamping area of the washer is visible as a flat area beside the hole (blue lines in Figure 5.14). Directly behind these clamped areas, global buckling occurs, which results in fibre breakage and final failure. Fibre breaks within the 0° layers indicate large compressive stresses. Due to the low layer thickness, the bending stiffness of the specimen is only slightly reduced, with fracture of a single 0° layer. Due to the remaining residual stiffness and the clamping by the washer, no global buckling occurs in the supported area.
Concerning regions far away from stress concentrations, no damage propagates. The area affected by damage resulting from the bearing load damage

is considerably smaller in the Thin-Ply specimen. In contrast, large delaminations between the layers can be seen in the Thick-Ply samples. The individual layers have fractured into numerous fragments and have shifted due to the delamination. This behaviour can also be seen in the two detailed images in Figure 5.14 e) and 5.14 f). Due to the fractures and the displacements, no global kink bands can be observed. Regarding the more distant areas, external delamination has continued, and the outer 45° layers have detached.

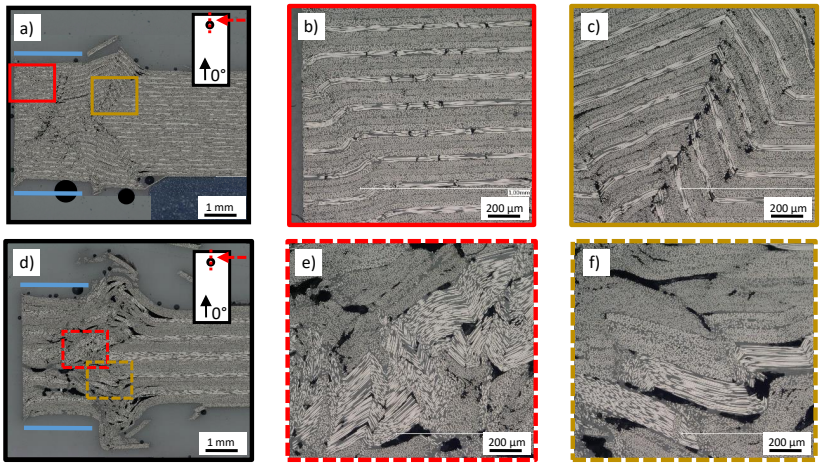

Figure 5.14: Micrographs of bearing Thin- (upper micrographs) and Thick-Ply (lower micrographs) specimen. The red and dark orange micrographs are detailed views of the images a) and b).

Due to the hybridisation with stainless steel foils, significantly higher bearing strengths can be observed (see Figure 5.13). In contrast to the Thin-Ply samples without steel with a bearing strength of 979.6 MPa, the strength of the samples with stainless steel foils increases to 1165.4 MPa in the case of 6.25 % stainless steel, via 1239.5 MPa in the case of 12.5 %, to 1513.9 MPa if all 90° layers are replaced by stainless steel (25 %). The bearing strength

increases by 54.6 %. In the case of the Thick-Ply fibre metal specimens, the bearing strength increases to 1470.6 MPa, an increase of 73 %. In addition to the increased bearing strength, however, the occurring damage mechanism changes. The corresponding stress-strain diagrams are shown in Figure 5.15. One representative sample is shown for each configuration. In addition to the fact described above that the Thick-Ply specimens (grey) show a progressive damage behaviour and the Thin-Ply specimens (light blue) a brittle failure, stress reductions can be seen within the curves of the hybrid specimens. For example, the curve of the Thin-Ply sample with a steel content of 25 % (dark blue) shows three stress reductions. The first occurs at 31.8 %, the second at 37 % and the third just before ultimate failure at 44.9 %.

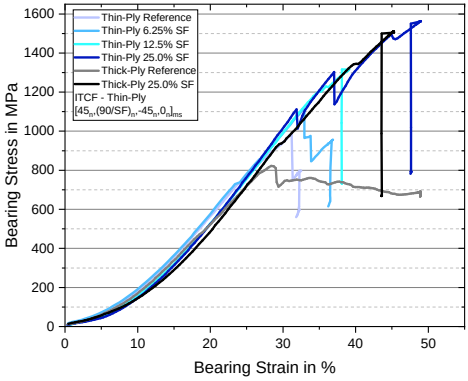

Figure 5.15: Stress-Strain diagram of Thin-Ply, Thick-Ply and their hybrid configurations.

This development indicates that the material has been damaged. To investigate the damage process more in detail, samples were tested and stopped when the first decrease in stress was reached so that micrographs could be prepared and the damage mechanism responsible for the first drop in tensile stress could be observed. These micrographs are shown in Figure 5.16. Figure 5.16 a) shows a Thick-Ply sample with 25 % stainless steel. Global buckling has

occurred, whereby the stainless steel layers have already deformed plastically. Figure 5.16 b) shows a detailed view of the sample. The radii of the buckling are small, which results in fibre fracture. Besides, the FML Thick-Ply samples show delamination at the interfaces between stainless steel and matrix. On the one hand, delaminations can be caused by high shear stresses at the interface due to the high strain of the stainless steel. On the other hand, the stress combined with initial damage can lead to out-of-plane stresses and enhance delamination growth. Besides the delaminations and the fibre breaks in the 0° layers, inter-fibre fractures occur in the ±45° layers. Larger radii show an intact fibre-matrix structure. Figures 5.16 d) and 5.16 e) show a Thin-Ply sample with a 25 % stainless steel content. Again, the first load drop indicates the first buckling. This buckling spreads out symmetrically from the centre of the sample to the outside and develops a kind of V-shaped wedge, as already observed with the FML Thick-Ply samples. As in Figure 5.16 b), fibre breaks can be observed in the 0° layers in Figure 5.16 e). However, no delaminations between stainless steel and matrix are visible. Due to the lower layer thicknesses and the associated higher number of interfaces, the shear stresses between the layers decrease, and delamination growth is suppressed. Figures 5.16 c) and 5.16 f) show a Thick-Ply sample without stainless steel and a Thin-Ply sample with 12.5 % of stainless steel. Both samples show the typical failure behaviour described above, global buckling exhibits from the mid-plane. With the Thick-Ply sample, it appears as if the 0° layers in the middle of the sample would fail under compression, initiating the formation of buckling to the outside. This assumption confirms symmetrical damage.

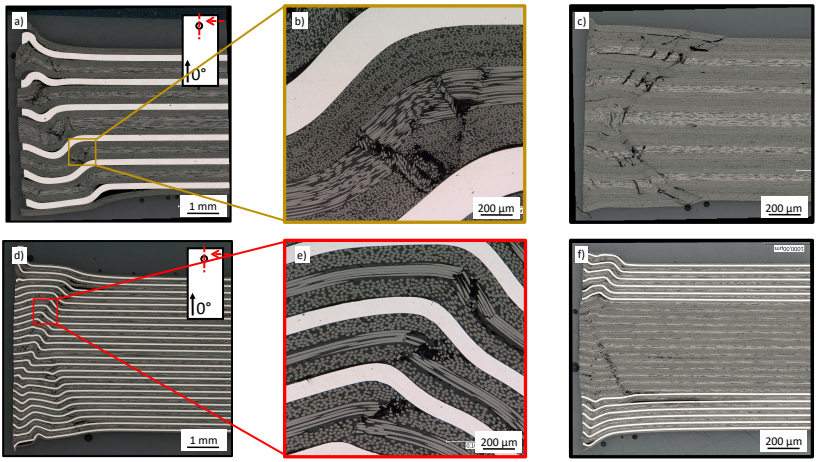

Figure 5.16: Micrographs of samples tested until the first damage; a) Thick-Ply with 25 % local steel content, b) Detailed view of micrograph a), c) Thick-Ply reference, d) Thin-Ply with 25 % local steel content, e) Detailed views of micrograph d), f) Thin-Ply with 12.5 % local steel content.

Whether it makes sense to use fibre metal laminates for structural applications, it is not sufficient only to consider the maximum bearing strength. In the case of conventional structural materials such as metals, an offset bearing strength of 2 % strain is the design criterion. Therefore, three parameters are of particular importance in the case of bearing tests, the maximum bearing strength, the offset bearing strength and the stress at the first load reduction, which is the first significant damage. All three parameters are shown in Figure 5.17. The blue bars represent the strength of the first measurable damage, the grey bars represent the offset bearing strength, and the black bars represent the maximum bearing strength. The Thick-Ply samples without stainless steel serve as reference material since they have the thicknesses commonly used today. However, the 160 gsm plies were laminated by block-scaling (four 40 gsm layers), so that the spreading process of the fibres results in good

quality in terms of fibre volume content, resin-rich regions and fibre angle deviation, which has a positive effect on compressive behaviour [7, 8].

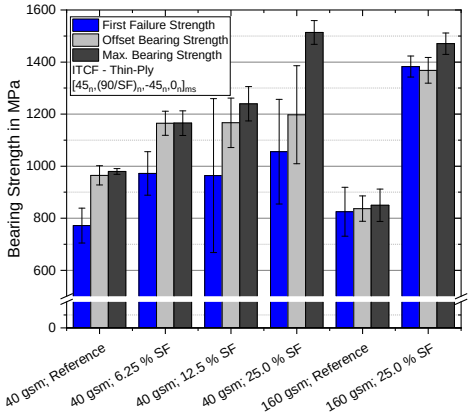

Figure 5.17: First failure (blue), offset (grey) and maximum bearing (black) strength for Thin- and Thick-Ply metal laminates.

The Thick-Ply samples show small differences between the first damage, the offset and the maximum bearing strength. Still, Thick-Ply samples exhibit a progressive damage behaviour so that even after the ultimate bearing strength, there is no risk of sudden failure. In comparison, the Thin-Ply samples without stainless steel have a higher offset and maximum bearing strength, but the stress of the first damage is at the same level as the Thick-Ply samples. Therefore, if the design guide tolerates no damage, the maximum allowable stress is equal to the Thick-Ply. However, after the first damage, a high residual safety factor exists, as the maximum bearing strength is 26.96 % higher. The hybrid laminates show significantly higher strengths regardless of the selected parameter. It is noticeable that the stress at the points of the first damage in all three FML Thin-Ply configurations has a similar value due to the high scattering. The offset stress, which is above the stress of the first damage, is the same for all three Thin-Ply FML configurations. A difference

is visible in the maximum bearing strength, which increases significantly with increasing steel content. Compared to the Thin-Ply samples without steel, the maximum bearing strength of the Thin-Ply samples with 6.25 % steel increases by 19.0 %, with 12.5 % by 26.5 % and the thin FML samples with 25 % by 54.6 %. The difference between the sample configurations results in the residual safety factor after damage. With increasing steel content, the safety factor increases significantly. Whether first damages are tolerable would have to be checked in a further study under cyclic load. The Thick-Ply samples reinforced with stainless steel show the best results in terms of bearing strength. The maximum bearing strength is in the same range as the 25 % Thin-Ply samples, but the offset and the first damage parameters increase significantly. The different damage mechanisms can be interpreted based on micrographs in Figure 5.18.

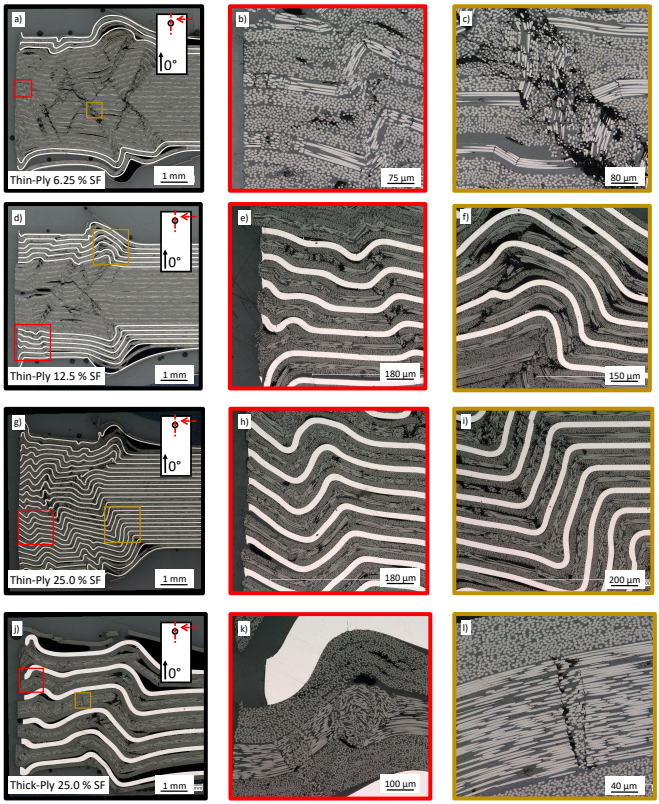

Figure 5.18: Micrographs of hybrid fibre metal composite specimens after bearing tests; a-c) Thin-Ply with 6.25 % local steel content, d-f) Thin-Ply 12.5 % local steel content, g-i) Thin-Ply with 25 % local steel content, j-l) Thick-Ply with 25 % local steel content.

The final failure of all configurations is due to buckling behind the specimen's support by the washers. Buckling in the clamping area has a local load drop as a consequence but is not critical regarding the final failure. These local damages can be assigned to the stress reductions in the stress-strain diagrams

(see Figure 5.15). However, due to the side-wise support, the specimens do not fail at the first buckling and receive higher compressive stresses. The Thin-Ply FML specimens all have several global kink bands. It is noticeable that in the regions where the stainless steel foils replaced the 90° layers, the carbon layers are supported and show minor damage. Even at high deformations of the stainless steel, the supporting effect is maintained.
Especially the middle layers of the samples with 6.25 % (Figure 5.18, a - c) and the 12.5 % (Figure 5.18, d - f) stainless steel show significant damages in the area of neat CFRP. Broken fibres in the 0° layers indicate that the fibres have failed due to high compressive stresses. Due to the supporting effect of the stainless steel and the washer, a local buckling does not result in a global failure. Similarly, the results for the Thick-Ply FML specimens show that ultimate failure results in buckling behind the supported area. But in contrast to the thinner layer thicknesses, the thicker layers do not buckle symmetrically from the centre and preferentially buckle to one side. The stress-strain diagrams indicate that the first damage of the Thick-Ply FML specimens occurs only at higher stresses but grows with increasing load and leads to final failure. However, fibre fractures occur in the 0° layers near the bolt (see Figure 5.18 i) and k)) caused by the high compressive loads. Due to the high bending stiffness of the thicker stainless steel foils and the washer, the 0° layers are still supported, and no global buckling occurs. Figure 5.18 k) show that the fibres broke into small pieces and have shifted to a kind of roundabout. Of particular interest are the ±45° layers next to the roundabout, some of which show no visible damage and are severely deformed.
The percentage change of the first failure bearing strength (blue), the offset bearing strength (grey) and the maximum bearing strength (black) compared to the maximum bearing strength of the Thick-Ply reference sample are shown in Figure 5.19. In the case of the maximum bearing strength, an improvement in the strength can be observed for all configurations, whereby no significant differences between the Thin-Ply FML samples can be observed due to the relatively high scatter in the first failure strength and also in the offset failure strength. However, there is a significant difference in the maximum bearing

strength. Compared to the Thick-Ply reference samples, the Thin-Ply samples with a steel content of 6.25 % increase by 37.1 %, those with a steel content of 12.5 % by 45.9 % and those with 25.0 % stainless steel by up to 78.1 %. Due to the use of stainless steel foil, the specimens are supported against global buckling, and local initial damage does not lead to final failure. The thicker FML specimens show significantly improved behaviour in all aspects. The thick stainless steel foil positively affects the laminate's bending and compression properties, and even local buckling is suppressed.

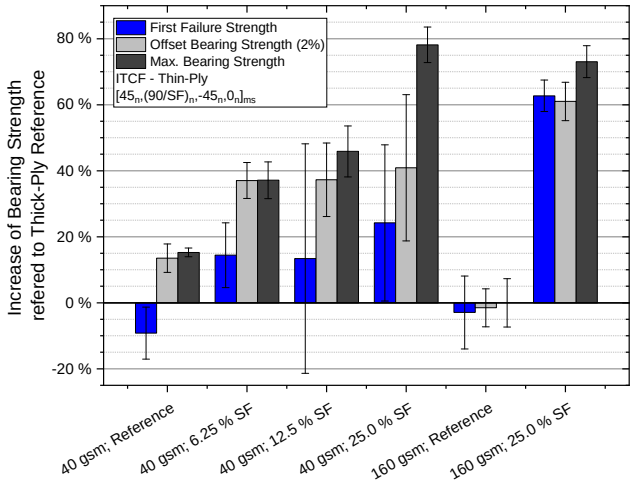

Figure 5.19: Increase of first failure (blue), offset (grey) and maximum (black) bearing strength referred to Thick-Ply reference.

In addition to the bearing strength, weight, and geometry of the joint is an important design parameter. An improved strength taking into account four times the weight, as is the case with pure stainless steel, would be practically meaningless. For this reason, the strengths should be viewed in relation to their weight, or in this case, in relation to their density. Figure 5.20 shows the global specific bearing strength. The global specific bearing strength is

the ratio of the bearing strength and the tested sample's global density. It can be seen that the parameters of the three Thin-Ply FML configurations approximate the maximum specific bearing strength but are still higher than those of the conventional specimens. Concerning the first failure, the results of the Thick-Ply samples with 25 % stainless steel exhibit the highest values, whereby these correspond to the value of the offset and should be taken as the maximum for design. Due to the formation of delaminations, the propagation of damage is not as critical in static bearing tests but probably have a strong effect on the fatigue bearing properties. This has to be clarified in further investigations. Related to the Thin-Ply FML samples, the samples with a steel content of 6.25 % show the highest specific strengths in the first failure. The values are 35.5 % above the specific first failure strength of the Thin-Ply samples and 26.0 % above the Thick-Ply samples without stainless steel. With the industrial application of the hybrid composites investigated in this study, it is shown that hybridisation with 6.25 % stainless steel achieves the same specific maximum bearing strength and the highest specific offset bearing strength as the configurations with a higher steel content. Therefore, although the bearing strength increases with a higher steel content, this does not offer any further advantage concerning the lightweight design due to the increased weight.

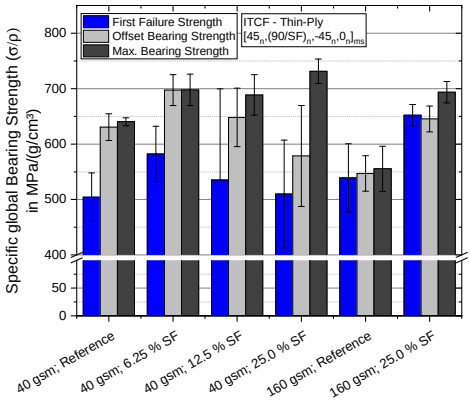

Figure 5.20: Specific first failure, offset and maximum bearing strength.

5.2 CFRP fatigue and fatigue after impact

5.2.1 Tensile tests

The results of the static tensile tests are shown in Figure 5.21 on the left. The tensile strength increases significantly with decreasing layer thickness in the range between 360 gsm and 60 gsm. Even lower layer thicknesses, 30 gsm, show no further improvement compared to the 60 gsm samples. However, the strength doubles between the 360 gsm and 30 gsm samples. In the case of the 360 gsm samples, the outer ±45° and 90° layers fully delaminate at low strains. Therefore the load is mainly transferred by the middle 0° layers, which significantly reduce the strength. This failure behaviour can also be seen in the fracture patterns shown in Figure 5.22. Image e) shows the 360 gsm sample. The pattern exhibits 0° layers with a high number of cracks in the longitudinal direction (splitting) primarily. Only local residues of the outer delaminated layers are still present. This behaviour is not observed at lower layer thicknesses. Figure 5.21 shows the stress-strain curves of the

tensile tests on the right-hand side. All configurations have the same Young's modulus at low strains. The modulus mainly dependent on the fibres and their orientation. However, with increasing load, initial damage occurs, and a decrease in stiffness is recorded for thicker layers.
Figure 5.23 shows the results of the acoustic emission measurements. The black curve corresponds to the stress-strain curve. The blue dots indicate the corresponding hits in kHz, which were recorded by the sensors. Due to the sensors' eigenfrequencies, the hits at 333, 500 and 1000 kHz are not included. The total energy in aJ is shown in red. For this purpose, the measured hits are added up. A higher total energy can be considered as a larger damage state. The AE data for the 360 gsm samples cannot be used due to early delamination of the outer layers from the middle 0° layers.

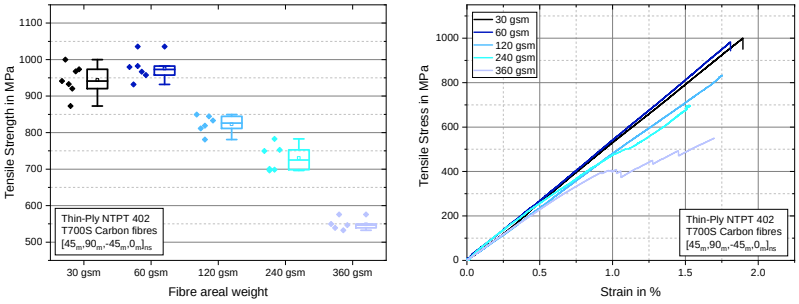

Figure 5.21: Tensile strength (left) and tensile stress-strain curves (right) depending on the layer thickness.

As can already be seen from the stiffness decrease in the stress-strain curves, the AE data of the 240 gsm specimens show that the first significant damage already initiates at 0.75 % strain and that further damage develops until the final failure. The fracture pattern of the 240 gsm samples differs only slightly from that of the 360 gsm samples, as the outer layers are completely delaminated. For the 120 gsm samples, the first significant damage occurs at

higher strains of around 1 %.

Furthermore, 30 gsm and the 60 gsm samples do not show larger damage until final failure, and therefore no decrease in stiffness and no change in strength can be determined. The AE data of the 60 gsm sample shows only a small plateau before the final failure. Initial damage of the 30 and 60 gsm specimens starts at 1.8 % strain. The fracture patterns of the 30, 60 and 120 gsm samples in Figure 5.22 differ from those of the 240 and 360 gsm samples. The delamination areas are smaller, and the fracture behaviour becomes more brittle as the layer thickness decreases. The 30 gsm samples show no delamination in the fracture pattern.

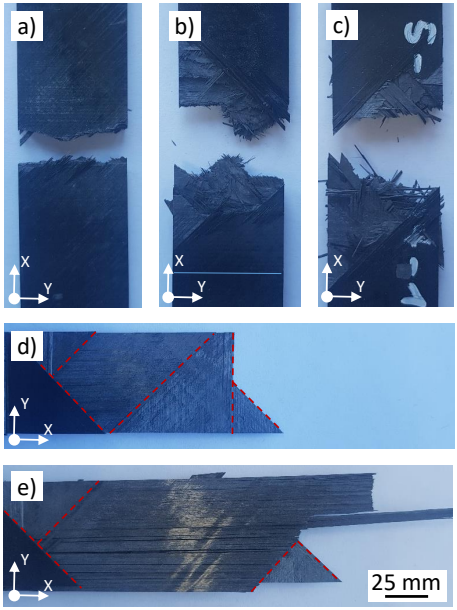

Figure 5.22: Fracture patterns of the tensile specimens after final failure. The red lines represent layer edges: a) 30 gsm, b) 60 gsm, c) 120 gsm, d) 240 gsm, e) 360 gsm.

The failure behaviour can be explained by the in situ strength of the 90° layers. With decreasing layer thickness, the strength of the 90° layers increases exponentially, which shifts the initiation of inter-fibre fractures to higher strains. Besides, the inter-fibre fractures are stopped at layers with different fibre orientations. For short inter-fibre fractures, the interlaminar shear strength is too low, and the crack tip's energy is not sufficient to initiate delamination. With thicker plies, however, new inter-fibre fractures and delaminations develop with increasing stress. The damage growth corresponds to the recorded hits of the AE data. The fracture patterns (Figure 5.22) demonstrate the same behaviour, the fractures offer a brittle failure, and with increasing layer thickness, a more delamination dominated failure behaviour occurs. As a result, it can be concluded that in the case of static tensile loading, a layer thickness of 60 gsm in combination with the fibres and resin system used in this study already shows the maximum achievable strength and a reduction in layer thickness does not provide any further advantage to the mechanical properties investigated. The freedom of design due to the higher number of layers is still an advantage.

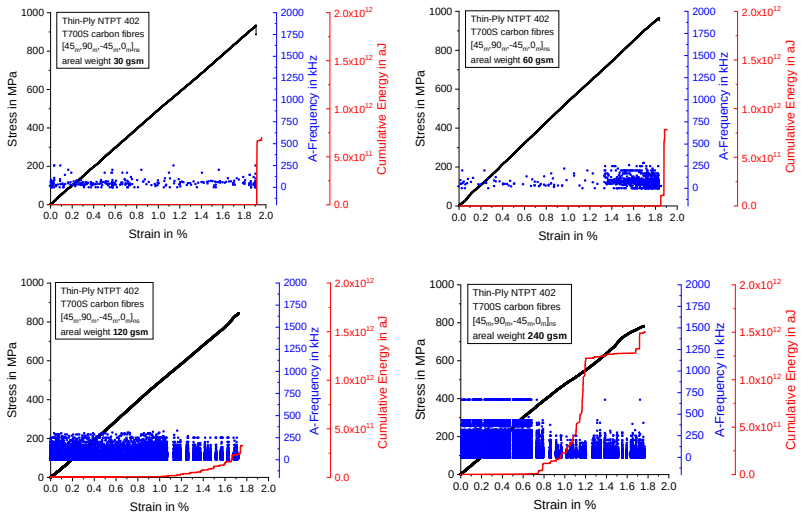

Figure 5.23: Stress-strain curves and the corresponding results of the acoustic emission measurements; top left: 30 gsm; top right: 60 gsm; bottom left: 120 gsm; bottom right: 240 gsm.

5.2.2 Compressive tests

The results of the compressive tests show a significant increase in strength with decreasing layer thickness from 360 gsm to 30 gsm. The left diagram in Figure 5.24 shows the compressive strengths, and the right diagram in Figure 5.24 the stress-strain curves of the compressive tests. The curve characteristics show that progressive failure occurs with low layer thicknesses. Initial damage or first local buckling and delaminations do not lead to final failure for thinner layers under compressive load. Figure 5.25 shows fracture patterns of the layer thicknesses 30, 60 120 and 360 gsm. There is no difference in failure behaviour between the 120 and 240 gsm samples. Samples with the thin layers show several delaminations (blue lines) within the samples. The 60 and 120 gsm

samples fail due to brooming. The outer layers delaminate outwards. Due to the high amount of fibres and the distribution of the 0° layers in sub-laminates, these have a relatively high bending stiffness after the first delaminations of the outer layers which leads to a decrease in stiffness but not to a final failure. With increasing load, more sub-laminates delaminate until the stiffness is too low and the specimen finally fails. An asymmetrical failure pattern (red line) is developed. The 360 gsm samples show early delamination of the outer layers. The delaminations initiate between the 0° and the 45° layers, so that all layers except the 0° layers are delaminated. Since the 0° layers are no longer supported, they buckle, and the specimen finally fails. The 30 gsm samples show a through-thickness failure. Although delaminations initiate as in the 60 and 120 gsm specimens, the residual stiffness of the outer layers (sub-laminates) is high enough that they do not buckle outwards and continue to transmit compressive forces. A stress reduction can determine the damage. However, if the compressive force exceeds a critical value, the layers buckle to one side, and a fracture surface develops that runs straight through the entire specimen (red line, image a)). In addition to the higher residual stiffness, Thin-Ply has superior laminate qualities, which positively affects the failure behaviour under compressive load [7, 8]. Fibre spreading results in more homogeneous fibre distribution, and resin-rich regions are smaller and less common.

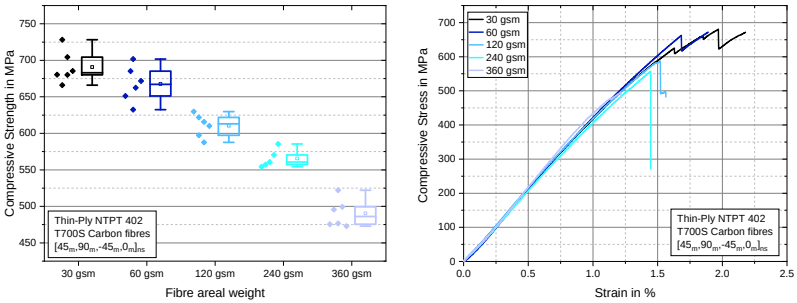

Figure 5.24: Compressive strength (left) and compressive stress-strain curves (right) depending on the layer thickness.

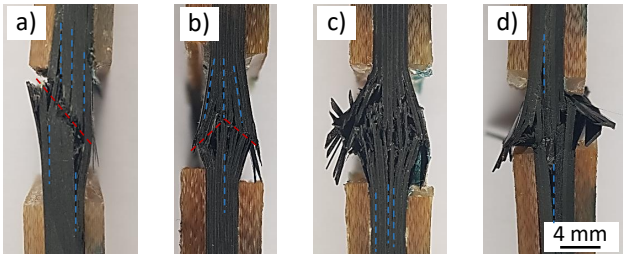

Figure 5.25: Fracture patterns of the compressive specimens after final failure. The blue lines represent delaminations and the red lines fracture planes: a) 30 gsm, b) 60 gsm, c) 120 gsm, d) 360 gsm.

5.2.3 Fatigue tests

Tension-Tension (R = 0.1)

The results of the tensile-tensile tests are shown in Figure 5.26. The left diagram represents the S-N curve; the amplitude stress is plotted versus the number of cycles to failure on a logarithmic scale. The open-symbols represent samples that have reached the run-out criterion of $1 \cdot 10^6$ cycles. Solid lines (S-N curves) show the calculated failure probability that 50 % of the specimens will fail at this number of cycles at a specific stress amplitude. The 50 % probability of failure of the 360 gsm samples is significantly lower than that of the other samples, although the curve is relatively flat. Due to the high layer thickness, all 0° layers are in the middle of the lay-up. The outer layers fully delaminate at low numbers of cycles, resulting in a type of unidirectional sample. The resulting unidirectional load-bearing layers result in a flat S-N curve since the fatigue properties are essentially dependent on the carbon fibres. The behaviour is also apparent in the stiffness degradation curve. The right-hand side of Figure 5.26 shows the relative stiffness, which is the quotient of the stiffness at cycle n and the initial stiffness of the first cycle. In this study, the stiffness is defined as the slope of the tangent of the stress-strain curve (hysteresis) at 5 % and 50 % of the maximum stress of each hysteresis recorded. The typical shape of an S-N curve consists of three phases. An early decrease in stiffness combined with initial damage such as inter-fibre fractures, a relatively constant plateau on which the damage grows and a slight but continuous decrease in stiffness occurs. Finally, a considerable reduction in stiffness and ultimate failure. In the case of the 360 gsm samples, a fourth phase has occurred, a plateau with constant stiffness. In this phase, all outer layers are already delaminated, and only the 0° layers in the middle of the specimens are loaded.

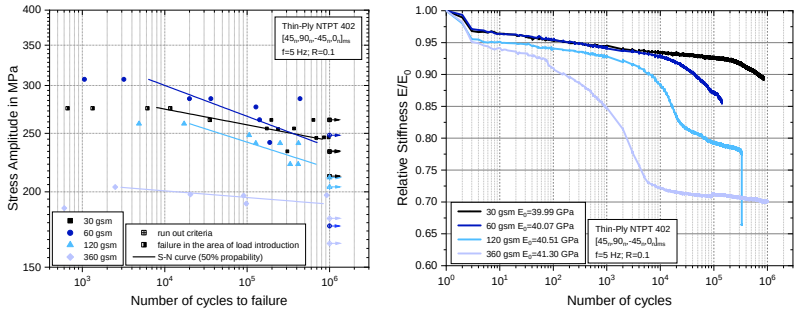

Figure 5.26: Results of the tensile-tensile fatigue tests with a stress ratio of R=0.1. The S-N curves of the corresponding layer thicknesses are shown on the left and the relative stiffness decrease of representative samples on the right.

There is a significant improvement in the fatigue stress of the 60 and 120 gsm compared to the 360 gsm samples. The 50 % probabilities of failure are shifted to higher stress amplitudes, and both S-N curves are steeper than the curve of the 360 gsm samples, where the 60 gsm specimens can handle even higher stresses. Both layer thicknesses have a similar slope of the S-N curve and are equally sensitive to failure behaviour. However, the relative stiffness show also differences between them. The curve of the 120 gsm samples have a fourth phase, as do the 360 gsm samples, which in turn is due to the relatively thick sub-laminate in the middle of the lay-up. The 60 gsm samples do not show this fourth phase anymore. The second decrease in stiffness leads to final failure and can be observed in the fracture patterns. The 120 gsm samples show a failure behaviour dominated by delaminations, whereas the 60 gsm samples fail brittle, and only a few delaminations are visible. As the static tensile tests have already shown, the formation of delaminations is suppressed for samples with reduced layer thicknesses, and brittle failure occurs. The failure behaviour under tensile-tensile load is similar to the failure behaviour under static tensile load. The fracture patterns do not differ from the fracture

patterns under static tensile load.
As described in the section materials and specimen preparation (see section 3.4.6), the 30 gsm samples had to be tested with the shape of a dogbone sample. Without this geometry change, all specimens fail in the load introduction area and therefore not conforming to the standard. Due to the brittle properties of the material and the suppression of damage, high local stress concentrations occur in the load introduction area, which leads to premature failure. Amacher et al. investigated fatigue open hole tensile tests. They observed that at higher stresses, thinner layer thicknesses lead to early failure because no stresses can be dissipated or diverted due to pre-damage in the stress concentration area. Below a certain stress amplitude, no damage occurs, and the fatigue properties improve significantly [8]. The fracture patterns show an increased failure in the area of load introduction for the samples with high stresses (half-filled squares in Figure 5.26, left) despite the sample geometry.
In addition to the cyclic tests performed until the sample failed or reached the run-out criterion, samples were tested at 67 % of UTS for $20 \cdot 10^3$ cycles and subsequently, X-ray images were taken. The X-ray images are shown in Figure 5.27. The radiographs indicate that delamination growth decreases with decreasing layer thickness, and in the case of the 30 gsm samples, no delaminations are present after $20 \cdot 10^3$ cycles. Due to the low layer thicknesses, the edge stresses are lower, so that the stresses are not sufficient for delamination growth. Between the 30, 60 and 120 gsm samples, a steady increase in the delamination area can be observed. The 360 gsm samples are an exception here. The edge delaminations appear to be smaller than those of the 120 gsm sample. However, it can be seen that extensive delamination has developed in the upper right area, extending into the centre of the sample. The delamination is located between the 0° layers in the middle and the adjacent 45° layer. The contrast medium has not been drawn far enough into the delamination for a sharp radiograph. However, it can be seen that the thick layers have strong delamination growth, which leads to early failure and the decrease of stiffness at low numbers of cycles.

At lower stresses, the specimens fail according to the standard within the smaller cross-section area. The stress concentrations in the load introduction area are below the critical stress. In the development of the stiffness decrease, brittle material behaviour can be recognized. The knowledge of the suppression of pre-damage and the results of Amacher et al. regarding stress concentrations suggests that thin-layer laminates have improved fatigue properties at low stresses and high numbers of cycles [8]. To investigate the fatigue behaviour under higher stresses, the load introduction area or the sample geometry must be further modified so that the load introduction is not the critical area.

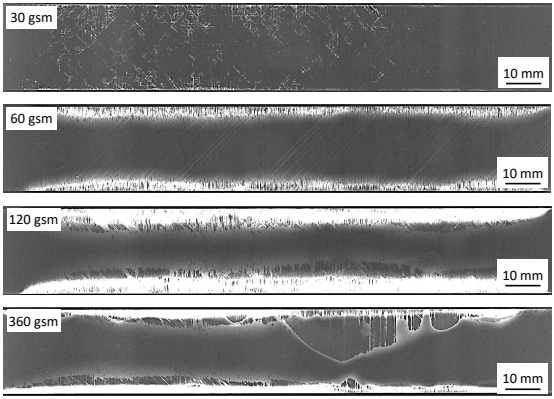

Figure 5.27: X-ray images of samples cyclic tested under tensile-tensile load with 67 % UTS for $20 \cdot 10^3$ cycles.

Tension-Compression (R = -0.5)

The fatigue tests results with a load ratio of R=-0.5 (Figure 5.28) show similar behaviour to the tensile-tensile tests. The fatigue properties improve with decreasing layer thickness. In the case of the 60, 120 and 360 gsm samples, no change in the slope of the S-N curves is apparent. The curves are shifted

in height. Only the S-N curve of the 30 gsm samples shows a lower gradient as under tension-tension. The intersection of the 30 gsm and the 60 gsm S-N curve is at about 40100 cycles and a stress level of 370 MPa. Stress concentrations at thin layer thicknesses will lead to premature failure at higher stresses in the load introduction area. In the tensile-tensile tests, specimens failed at amplitude stress of about 258 MPa near the tabs, which corresponds to a maximum stress of 572 MPa. The tensile-compressive samples fail in the area of the tabs at amplitude stress of about 381 MPa, which corresponds to a maximum stress of 508 MPa. However, the two stresses are not directly comparable since the stress of the tensile-tensile specimens refers to a smaller cross-section area due to the specimen design of a dogbone. The tabs of the samples have the same geometric dimensions and, when the force per mm of specimen thickness is calculated, the critical load is 12.03 kN/mm for the tensile-tensile specimens and 12.70 kN/mm for the tensile-compressive specimens. Thus the same problems arise under tensile-compressive load as under tensile-tensile load. Nevertheless, thinner layers display superior fatigue behaviour at higher load cycles, as they occur in industrial applications.

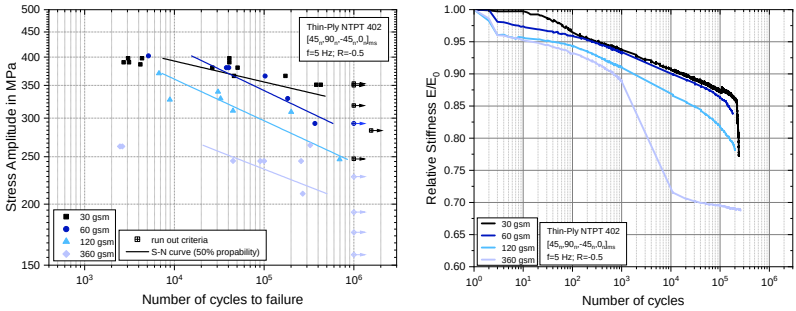

Figure 5.28: Results of the tensile-compressive fatigue tests with a stress ratio of R=-0.5. The S-N curves of the corresponding layer thicknesses are shown on the left and the relative stiffness decrease of representative samples on the right.

The right diagram of Figure 5.28 shows that the stiffness decreases over the number of cycles. The curves do not show a typical horizontal plateau as under tension-tension but a region with a constant stiffness decrease. The stiffness degradation of the 30, 60 and 120 gsm samples looks very similar. Noticeable is the substantial decrease of the 360 gsm sample in the range between 10^3 and 10^4 cycles. To describe this reduction in stiffness in more detail, Figure 5.29 shows the samples' hysteresis. The diagrams show the hystereses of 10^1, 10^2, 10^3, 10^4 and 10^5 cycles. The hysteresis of a 30 gsm sample is in the upper left, of a 60 gsm sample in the upper right, of a 120 gsm sample in the lower left and a 360 gsm sample in the lower right corner. With increasing layer thickness, the angular offset concerning the first cycles increases and also, the area of the hysteresis (energy per cycle) increases with decreasing layer thickness. A flatter hysteresis exhibits a lower stiffness due to damage like inter-fibre fractures and delaminations. In the case of the 360 gsm samples (bottom right), the first 1000 hysteresis are similarly superimposed, but the angle of the hysteresis at higher numbers of cycles change strongly. This is due to the formation of delaminations between the outer layers and the 0° layers in the middle of the samples. The small opening of the hysteresis of the 360 gsm sample at a high number of cycles indicates that only the 0° layers are loaded, and no energy is dissipated due to open and close of inter-fibre fractures or delaminations. It can be seen that the deviation between the hysteresis is smaller with lower layer thicknesses, which indicates a constant material behaviour independent of the number of cycles. As in the static, a brittle material behaviour of the thin layer thicknesses can be seen. The fracture patterns do not differ from the fracture patterns under static tensile loading, as the specimens under tensile-compressive loading fail in the tensile region of the hystereses.

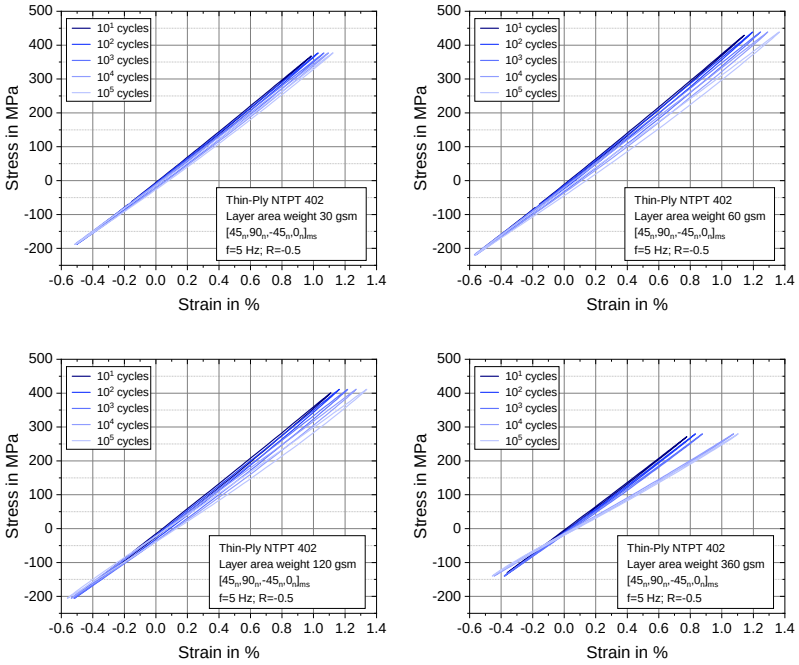

Figure 5.29: Hysteresis of different layer thicknesses (upper left: 30 gsm, upper right: 60 gsm, lower left: 120 gsm and lower right: 360 gsm) at 10^1, 10^2, 10^3, 10^4 and 10^5 cycles.

Compression-Compression (R = 10)

Figure 5.30 shows the S-N curves of the fatigue tests under compressive-compressive load (R=10). The results demonstrate an improvement of the fatigue properties with decreasing layer thickness. Due to the test setup and fibre composites' failure behaviour under compression, there is a significant scatter within the results. Still, the gradient of the S-N curves shows differences. The slopes of the 30 and 60 gsm samples are much steeper. Fracture

patterns of tested specimens in Figure 5.31 show a changing failure mechanism, as can also be found under static compressive loading of quasi-isotropic samples. The fracture patterns show four specimens that have been loaded about half a million cycles to failure. In the case of the 360 gsm specimens, the outer layers delaminated at a low number of cycles. The failure behaviour is a combination of through-thickness (0° layer), and brooming [136]. Due to the absence of supporting layers, the middle 0° layers started to buckle, and the final failure occurred. The 60 gsm and 120 gsm samples show a similar failure pattern. In both cases, brooming occurs, and delaminations and sub-laminates have formed. In the case of the 120 gsm samples, the sub-laminates usually consist of four layers with one 0° layer on the outside, so that the sub-laminates are fragile against buckling. In contrast, the sub-laminates of the 60 gsm samples consist of more than four layers, and 0° layers are not only at the outside of the sub-laminates. The middle 0° layers significantly increase the bending stiffness of the sub-laminates and improve the mechanical properties under compressive load.

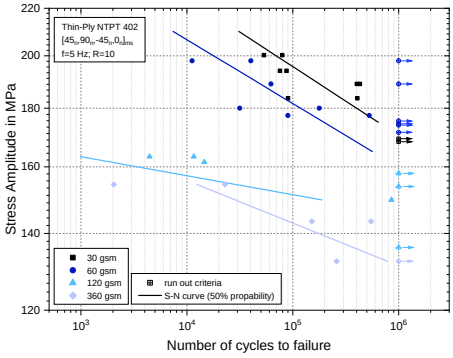

Figure 5.30: S-N curves of the compressive-compressive fatigue tests with a stress ratio of R=10.

The fracture pattern of the 30 gsm sample differs from the other samples. Delamination occurs in a small area, and the fracture patterns show no buckling of the outer layers or sub-laminates. The fracture pattern shows a longitudinal splitting. The stop criterion of the fatigue stress-controlled tests was set with a maximum displacement. The 30 gsm samples show a residual compressive strength even after stopping the tests. Due to the sub-laminates, the residual stiffness is relatively high concerning the existing damage. However, due to the displacement of the upper and lower part of the specimen, the test had to be stopped. For industrial applications, the failure behaviour implies a high safety factor concerning the use of Thin-Ply under cyclic compressive load. Despite damage, there is a relatively high residual stiffness and strength.

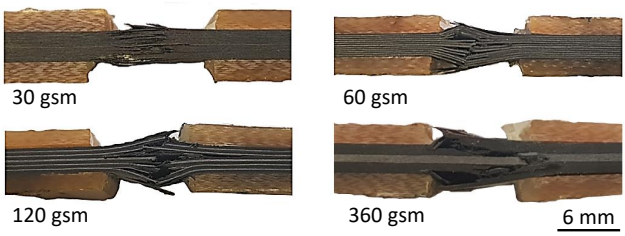

Figure 5.31: Representative fracture patterns of specimens with different layer thicknesses tested under compressive-compressive load.

5.2.4 Constant-life diagram

The constant-life diagram in Figure 5.32 summarized the fatigue results obtained. The mean stress is plotted on the abscissa and the amplitude stress on the ordinate. Each point represents the ratio between mean stress and amplitude stress as a function of the load ratio at $5 \cdot 10^5$ cycles. The theoretical interpolations between the measured values are calculated according to the piecewise linear interpolation of Philippidis et al. [77]. A reduction of the layer thickness results in an improvement of the fatigue properties

and a higher number of load cycles can be tolerated at the same stress level. Only under tensile-tensile loading (R=0.1), the 30 gsm samples achieved no significant improvement compared to the 60 gsm samples. Especially in tensile-compressive load conditions (R=-0.5), the thin layer thicknesses exhibit a significant improvement. Due to the damage suppression, no pre-damage initiates under tensile load, leading to a low stiffness reduction and a superior compressive performance.

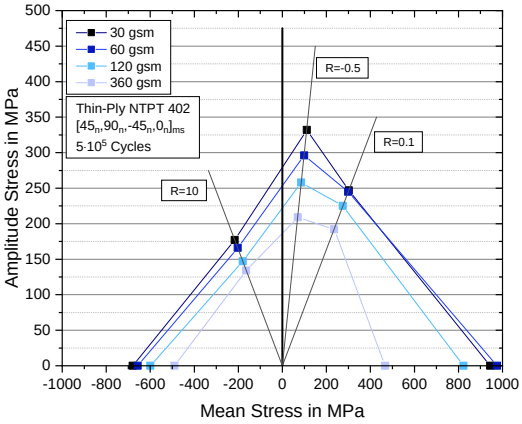

Figure 5.32: Constant-life diagram as a function of the layer thickness at $5 \cdot 10^5$ cycles. Material properties calculated using the linear interpolation method.

In Figure 5.33, as in Figure 5.32, the fatigue tests results are shown in a constant-life diagram. The cyclic behaviour under different load conditions was calculated using the semi-empirical method by Harris et al. presented in section 2.3. For this purpose, the static tensile and compressive strengths and the extrapolated stresses (amplitude stress and mean stress) at $5 \cdot 10^5$ cycles, were used for the calculation of the parameters f, u and v. Table 5.4 summarises the calculated parameters as a function of layer thickness.

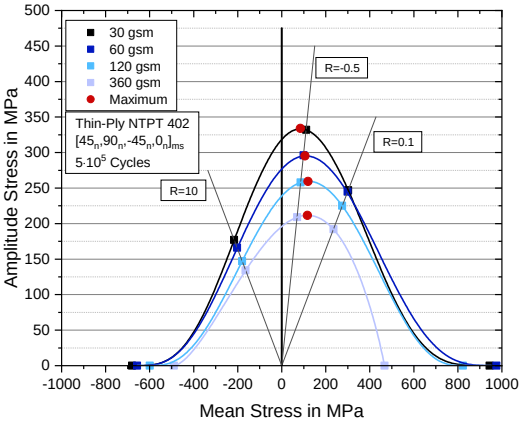

Figure 5.33: Constant-life diagram as a function of the layer thickness at $5 \cdot 10^5$ cycles. Material properties calculated using the semi-empirical method by Harris et al.. The red symbols indicate the max. values of the bell curves.

The material behaviour curves under cyclic load indicate that the maximum amplitude stress increases with decreasing layer thickness. The Thick-Ply samples curve with a fibre areal weight of 360 gsm shows a significantly steeper curve on the tensile dominant side, and the maximum of the curve is on the tensile dominated side. The maxima of the respective curves are listed in Table 5.4 regarding their amplitude stress σ_a and mean stress σ_m. The load ratio R can be calculated using Equation 5.3.

$$R = \frac{\sigma_\mathrm{min}}{\sigma_\mathrm{max}} = \frac{\sigma_\mathrm{m} - \sigma_\mathrm{a}}{\sigma_\mathrm{m} + \sigma_\mathrm{a}} \tag{5.3}$$

According to the stresses, the stress ratio of the maximum stress amplitude (red symbols Figure 5.33 for the Thick-Ply specimens is R=-0.29. The

compressive loads do not yet cause significant damage, or existing damage does not accelerate.

Table 5.4: Parameters f, u and v for modelling the cyclic behaviour according to the semi-empirical model of Harris et al.. The amplitude stress, mean stress and load ratio correspond to the maxima of the bell-shaped curves.

	Parameter			**Stress in MPa**		**Load ratio**
	f	u	v	Amplitude	Mean	
30 gsm	1.209	4.364	3.885	334.11	84.92	-0.59
60 gsm	1.056	3.761	3.324	295.29	106.17	-0.47
120 gsm	0.742	2.898	2.963	259.36	119.90	-0.37
360 gsm	0.387	0.939	1.628	211.45	116.82	-0.29

In contrast to the steep decrease in the tensile dominated side of the Thick-Ply specimens, the specimens with lower fibre areal weights show a relatively symmetrical bell-shaped curve. Besides the higher maximum amplitude stresses, the mean stresses of the corresponding maxima shift to smaller stresses.

For the Thin-Ply specimens, the load ratio of the maximum Performance is R=-0.59. As before, the load ratio is in the tensile-dominated range, but the compressive components are larger than with thicker layers. Thus, the cyclic compressive and tensile behaviour converges more and more with decreasing layer thickness. Due to the suppression of delamination under tensile load, higher compressive loads can be sustained without damage propagation or buckling. Figure 5.34 shows the parameters f, u and v calculated for evaluating the curves according to the respective layer thickness and the corresponding stresses to the maximum of the curves, which are listed in Table 5.4.

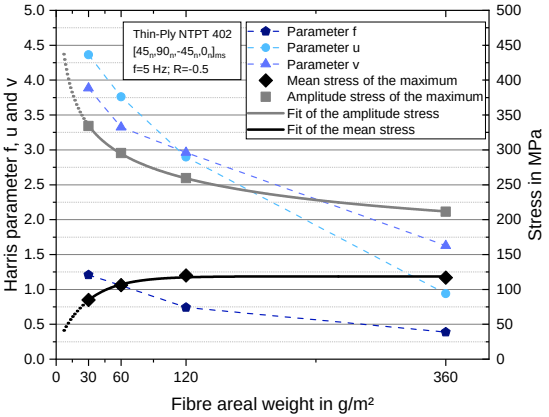

Figure 5.34: Parameters f, u and v to describe the fatigue behaviour under different load ratios calculated according to Harris et al. and stress maxima of the approximated curves. The blue dashed lines are for illustration only.

According to Harris et al., parameter f describes the curve's height and amplitude stress. The parameter f increases with decreasing layer thickness. The parameters u and v, on the other hand, influence the shape of the curve. As already described in the upper part, the right-hand side of the CLD curve of the 360 gsm samples decreases rapidly, whereas the left-hand side has more the shape of a bell curve. The different shapes of the right- and left-hand side bell-shaped curve can be seen in the relatively large difference between u and v. At about 120 gsm, the two parameters cross each other. The bell-shaped curve of the 120 gsm samples is symmetrical to the maximum. With decreasing layer thickness, the two parameters move away from each other. The slope of the right- and left-hand side of the 30 gsm and 60 gsm bell-shaped curves differ slightly from each other.

The fit of the amplitude stress curve is shown in grey, and the fit of the mean stress of the respective maxima in black. As already described, the amplitude stress increases and the mean stress decreases with decreasing layer thickness.

The stress amplitude curve was fitted using the Origin 2019b software from OriginLab Cooperation, Northampton USA. The Allometric 1 model was used to approximate the curve, which works according to Equation 5.4. m_{fa} is the fibre areal weight.

$$\sigma_{\mathrm{a}} = q \cdot {m_{\mathrm{fa}}}^{\mathrm{y}} \tag{5.4}$$

q and y and the correlation factor R^2 are listed in Table 5.5. It is noticeable that the curve shows similarities to the in situ strength from the analytical model of Camanho et al. [124]. Camanho et al. propose that a 90° strength of the layer within a laminate increases exponentially with decreasing layer thickness and converges to infinity at increasingly smaller thicknesses, as does the amplitude stress curve from Figure 5.34. A theoretical infinite strength due to the in situ strength would, therefore, also lead to infinite amplitude stress. The minimum achievable layer thickness represents a boundary concerning the maximum amplitude stress and corresponds to the thickness of one carbon fibre. The used carbon fibres in this study have a thickness of 7 µm. The mean stress curve (Figure 5.34 black curve), in this case, would still show a positive value, which indicates that the maximum of the bell-shaped curve is still in the tensile dominated regime (to the right of R=-1). A material behaviour that exhibits its maximum cyclic performance with the same proportions of the tensile and compressive load is not achievable with this model. The fit of the black curve was done according to the Asymptotic 1 model (see Equation 5.5). The corresponding values of the two models are gave in Table 5.5.

$$\sigma_{\mathrm{m}} = q - y \cdot z^{\mathrm{m_{fa}}} \tag{5.5}$$

Overall, the cyclic results show how critical cyclic tests are concerning the use of new materials. When comparing Thick-Ply and Thin-Ply specimens'

failure behaviour, the Thick-Ply samples show an identical tensile and compressive strength. Still, under cyclic loading, superior performance in the tensile dominated area. With decreasing layer thickness, the tensile strength increases disproportionately to the compressive strength. Concerning the fatigue behaviour, the tensile and compressive components converge at the maximum of the bell curve. The changes in the static and cyclic properties are opposite.

Table 5.5: The models used for the estimation of the stress amplitude (grey curve Figure 5.34) and mean stress (black curve Figure 5.34) depending on the fibre areal weight.

	Amplitude stress	Mean stress
Model	Allometric 1	Asymptotic 1
Equation	$\sigma_{\mathrm{a}} = q \cdot {m_{\mathrm{fa}}}^{\mathrm{y}}$	$\sigma_{\mathrm{m}} = q - y \cdot z^{\mathrm{m_{fa}}}$
q	625.74 ± 3.99	118.69 ± 2.73
y	-0.184 ± 0.002	99.34 ± 35.18
z		0.975 ± 0.011
R^2 (COD)	0.99988	0.98545

5.2.5 Impact

Figure 5.35 shows representative ultrasound images and micrographs of the occurring impact damage. The ultrasound images illustrate the defect depth of the damage, and an approximation of the depth is visualized by different colours. If there are several damages on top of each other, only the uppermost damage could be detected. The ultrasound images demonstrate that the damaged area's extent and the damage pattern depend on the layer thickness. The 360 gsm samples show a typical failure behaviour for fibre reinforced composites. Inter-fibre fractures and delaminations are visible, which increase with the depth of the sample. Depending on the fibre orientation, the damage spread out in a different direction. With decreasing layer thickness, the failure pattern changes. The number and length of inter-fibre fractures decrease

until they are entirely suppressed in the case of the 30 gsm samples, as has also been shown by Arteiro et al. and Saito et al. [9, 91]. The 60 gsm samples show fewer inter-fibre fractures but a high number of delaminations. Sub-laminates are developed, which have a thickness of four layers, 240 µm. The high number of delaminations is untypical for compression after impact (CAI) samples (ASTM D7137-05 [148]) with thin layers. However, this results from the smaller clamping device used in this study.
In contrast to the larger standard CAI specimens, less material can absorb energy and locally, the damage is increased. Due to small deformations and the suppression of inter-fibre fractures in Thin-Ply samples, less energy can be dissipated elastically, and high shear stresses are applied, which initiate delaminations. The shape of the delaminations has changed from a peanut to a circular shape. In the case of the 30 gsm sample, three large circular delaminations occurred. The first delamination develops between the middle layers, the highest shear stress area, and two sub-laminates are developed. A further load increases the shear stresses within the two sub-laminates. If the shear stresses also exceed the critical stress in the sub-laminates between the new middle layers, further delaminations occur. The shear stresses between the other layers are not sufficient to initiate further delaminations as with the 60 gsm samples. About 50 % of the 30 gsm samples show this failure pattern. The other 50 % show a similar failure pattern to the 60 gsm samples. It appears that the test setup is at a tipping point between the two failure modes. It was not possible to increase the energy because higher energies caused fibre breaks on the specimen's backside. Lower energies were not possible because of the test setup and machine used.

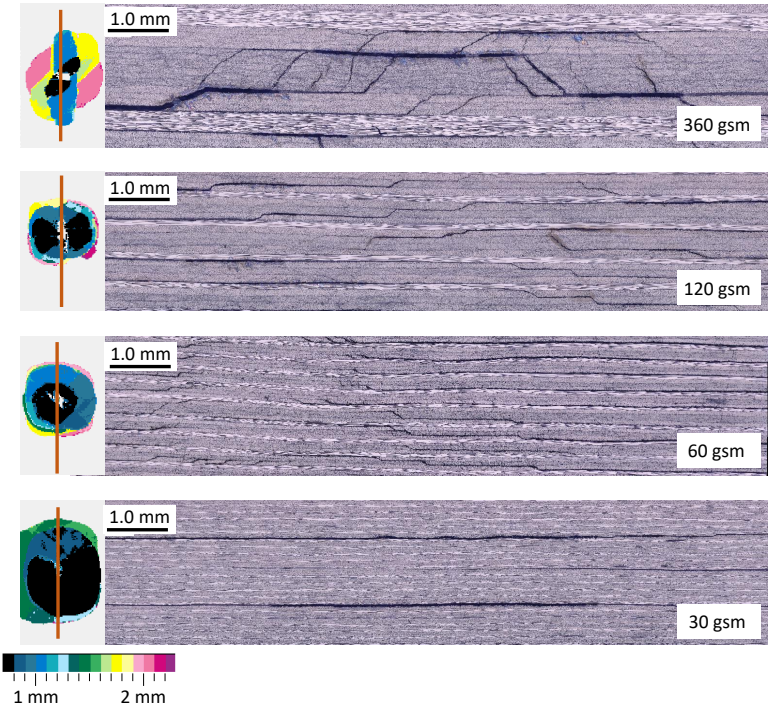

Figure 5.35: Ultrasound C-Scan images and micrographs of the impact damages, from top to bottom: 360 gsm, 120 gsm, 60 gsm and 30 gsm.

5.2.6 Fatigue after impact

Figure 5.36 shows the S-N curves of the pre-damaged samples. The solid lines correspond to the pre-damaged samples' S-N curves and the dashed lines to the samples' S-N curves without impact damage (see section 5.2.3). As expected, the lifetime of the pre-damaged samples is shorter than that of the undamaged samples. However, the difference between the pre-damaged and

non-damaged specimens varies between the layer thicknesses. Considered at $1 \cdot 10^5$ cycles, the 60 gsm and 360 gsm samples show the highest decrease of fatigue stress with 31.9 % and 28.1 % respectively.

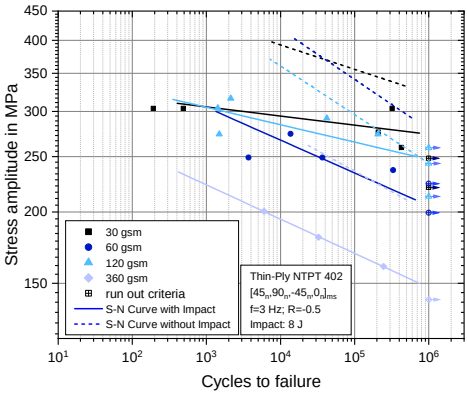

Figure 5.36: S-N curves with (solid lines) and without (dashed lines) impact of the tensile-compressive fatigue tests with a stress ratio of R=-0.5.

As seen in the micrographs, the samples with a layer thickness of 360 gsm show large delaminations and matrix cracks (see Figure 5.35). The growth of damage with an increasing number of load cycles reduces the fatigue strength. A computed tomography system examined the pre-damaged samples after a certain number of cycles and compared the damage patterns. The samples were tested with a maximum stress of 35 % UTS (undamaged) and analysed after 0, $5 \cdot 10^4$, $3 \cdot 10^5$ and $8 \cdot 10^5$ cycles. Figure 5.37 presents representative images of the 30 gsm and 360 gsm pre-damaged samples after loading. The damage patterns of the 360 gsm specimen show large, visible orientation-driven delaminations. The damaged area increases significantly with the increasing number of cycles. The delaminations reach the edge of the sample after only $5 \cdot 10^4$ cycles, and cracks are visible on the top surface after $3 \cdot 10^5$ cycles. The damage of the 360 gsm sample growth perpendicular to the

tensile direction. Due to the fatigue loading, further inter-fibre fractures have initiated, leading to the development of new delaminations and the growth of existing delaminations due to high interlaminar shear stresses. As caused by the impact (asymmetric damage), slight buckling of the specimen increases the stresses within the crack tip of delamination, supporting damage growth. The micrograph of the 60 gsm sample also shows a high number of delaminations. Each sub-laminate consists of four layers and thus has a thickness of about 240 µm. The individual delaminations are arranged circularly around the impact (see Figure 5.35). This geometric arrangement weakens the material in all spatial directions and favours a buckling of the sample or the layers, resulting in premature failure. Additionally, the individual sub-laminates have a low bending stiffness; the respective 0° layer is located on the outside at the sub-laminates and is not supported against buckling.

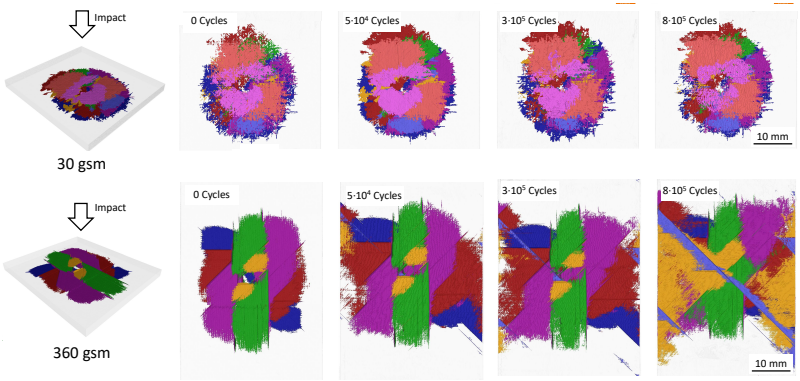

Figure 5.37: Computed tomography images of the impact damage of the 30 gsm (top) and the 360 gsm sample (bottom). The left two images show the initial state after the impact, the three right images show the damage pattern after cyclic loading of $5 \cdot 10^4$, $3 \cdot 10^5$ and $8 \cdot 10^5$ cycles. Colours are chosen arbitrary and indicate layers of damage at different depths.

As already described in the previous part, the 30 gsm samples show two different failure patterns. Some samples show few but very large delaminations (Figure 5.35), and other samples show more and smaller delaminations like the 60 gsm samples. Figure 5.38 shows cross-sections of the impacts from Figure 5.37 perpendicular to the loading direction. The delaminations are highlighted, and the colours are chosen arbitrary and indicate damage at different depths. In addition to the cross-sections, detailed images from the respective impact area are shown, and the thicknesses of the sub-laminates are measured. The computed tomography-cross-sections reveal that the thinnest sub-laminates are approx. 220 µm thick and have at least eight CFRP layers. However, thicker sub-laminates are also visible up to 720 µm. Due to the higher number of CFRP layers and the support of the inner 0° layers against buckling, the sub-laminates have a higher bending stiffness than the sub-laminates of the 60 gsm samples. As with the 60 gsm samples, a circular arrangement of the delaminations can be found, which would indicate a large reduction in fatigue properties. However, the specimens lifetime decreased by only 20.3 %. The computed tomography cross-sections demonstrate that with an increasing number of cycles, the damage does not grow any further, and a static state of damage is achieved. The laminate exhibit no matrix cracks, and the formation of delaminations is suppressed. The interlaminar shear stresses are not sufficient for the growth of delaminations. Due to the large number of layers and the associated high number of interfaces, the interlaminar shear stresses are lower between the layers. The cross-sections of the tomography scans of the 360 gsm samples show a damage progression (green and red delamination) and also new damages such as inter-fibre fractures and delaminations (yellow delaminations) with an increasing number of cycles. As a result, the lifetime is reduced.

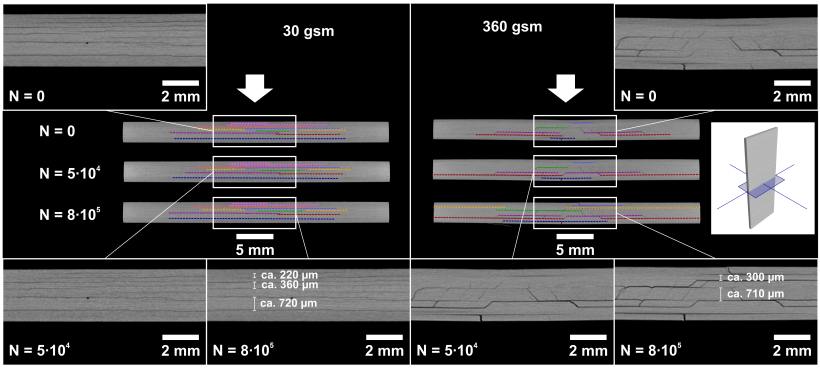

Figure 5.38: Cross sections of the impacted specimens (left 30 gsm and right 360 gsm) after 0, $5 \cdot 10^4$ and $8 \cdot 10^5$ cycles. Colours are chosen arbitrary and indicate layers of damage at different depths.

The 120 gsm samples exhibit the smallest reduction in fatigue performance. Contrary to this trend, the micrographs in Figure 5.35 show inter-fibre fractures and delaminations. Concerning the residual stiffness of the sub-laminates, the delaminations are between the 0° and 45° layers. The differences between the 120 gsm and samples with thinner layers (30 and 60 gsm) can be seen in the ultrasound images in Figure 5.35. The delaminations are not circular but have the shape of a peanut. Thus, although larger delaminations are present, they spread preferentially in the direction of the fibre orientation in the layer. The delamination areas are small in transverse direction to the preferred delamination orientation, leading to a high local residual stiffness.

6 Conclusion

One approach to exploit the full potential of carbon fibres is to reduce the layer thickness. The use of Thin-Ply composites has advantages and disadvantages in terms of mechanical performance and failure behaviour. Unfortunately, concerning structural applications, a compromise has to be made. This study demonstrates the superior behaviour of Thin-Ply composites under cyclic loading with and without local damage, as well as improving performance in areas of high stress concentration by local hybridisation. This thesis examines the research hypothesis:

> *Thin-Ply composites improve the lightweight potential of primary structures*

Four limitations regarding the use of Thin-Ply composites in primary structures were identified, and working assumptions were formulated, which were investigated experimentally.

6.1 Hybridisation - Thin-Ply fibre metal laminates

The first two working assumptions investigate the failure behaviour of Thin-Ply laminates locally hybridised with stainless steel foils. Concerning the failure behaviour of hybrid laminates, it is essential to achieve sufficient adhesion between metal and composite. Therefore, in the first part of this thesis, the surface pre-treatment of stainless steel is investigated. In addition to conventional roughening, chemical etching processes, a low-temperature plasma and the Sol-Gel process were investigated. The surface pre-treatment

with the Sol-Gel process showed the best performance in terms of fracture mechanics. The pre-treatment of the stainless steel was therefore carried out after the Sol-Gel process for all further investigations.

A limitation concerning the use of Thin-Ply in primary structures is the failure behaviour in areas of high stress concentrations. The reduction in strength increases with decreasing layer thickness. This behaviour led to the first working assumption:

> *Local steel hybridisation of Thin-Ply laminates reduces the impact of stress concentrations and strength degradation*

Thin-Ply unidirectional prepregs with a fibre areal weight of 40 gsm and Thick-Ply prepregs with a fibre areal weight of 160 gsm (block-scaling 4 x 40 gsm) were investigated. In areas with high stress concentrations, stainless steel foils substituted local the 90° layers. Four different volume contents of stainless steel were investigated (0, 6.25, 12.5 and 25 %).
The open hole tensile strength increases significantly with increasing steel content. With a local steel content of 25 %, the strength of the Thin-Ply FML rises by 64 %, and even if the strength is related to the density, the specific strength increases by up to 36 %. The notch sensitivity decreases with an increase in steel content.
The Thick-Ply specimens show a delamination dominating failure behaviour. Delaminations occur in the area of the hole and the transition area between stainless steel and 90° CFRP layers. Due to the thick layers, there is a substantial increase in stiffness in the area of the transition zone between 90° CFRP layers and metal. The difference in stiffness causes high local stress concentrations, which lead to the initiation of delamination. Due to the relatively high interlaminar shear stresses between the layers, new delaminations initiate, and existing ones spread further.
Using thinner layers, the transition zone between stainless steel and 90° CFRP layers can be evenly distributed over a large area, and the stress concentrations are reduced. Furthermore, the interlaminar shear stresses are lower due to the

higher number of layers. Both effects suppress the initiation of delamination between metal and CFRP. The micrographs show that the stainless steel foils have deformed plastically. The plastic deformation and the load transfer to more distant areas act as a blunting mechanism, like pre-damage in Thick-Ply CFRP and the open hole tensile strength increases.
Based on the experimental results, the first assumption can be verified, and areas with high stress concentrations are no longer a limiting factor for the use of Thin-Ply composites for primary structures.

The second working hypothesis examines the load introduction by bolted connections. By using Thin-Ply, the weight of a structure can be reduced due to the higher strength of the material and the wall thickness decreases. But a thinner wall thickness weakens the load-bearing behaviour. Working assumption two was:

> *Local steel hybridisation of Thin-Ply laminates improves the load-bearing capacity*

The materials and steel contents used are identical to those of the open hole tensile tests. The ultimate bearing strength increases with increasing steel content. 1513.9 MPa is the bearing strength if all 90° layers are replaced by stainless steel (25 %), which corresponds to an increase of 54.6 % compared to the Thin-Ply samples without steel (979.6 MPa). The offset strength of the Thin-Ply FML specimens, which corresponds to a strain of 2 %, is also 55 % higher than that of Thin-Ply without stainless steel. Since the offset strength is used as a reference for the design process of bolted joints, the Thin-Ply samples with a steel content of 6.25 % have the best performance in terms of offset strength and weight. There are no differences between the offset strengths of the Thin-Ply FML samples and the density of the samples with 6.25 %is the lowest. In addition to the higher strength, the hybridisation results in a more progressive failure behaviour. Due to the support of the CFRP layers by the stainless steel foil, initial damage does not lead to final failure.

The Thick-Ply samples, with 25 % stainless steel, have the highest offset strength. The thick stainless steel foils have a high bending stiffness, which supports the laminate at higher compressive loads due to the bolt, and therefore higher strengths are achieved.
Based on the experimental results, working assumption two can be verified. Although the strengths of a bolt connection are still below the tensile strength, the bearing strength can be significantly increased by hybridisation.

6.2 Fatigue and fatigue after impact behaviour of Thin-Ply

Working assumption three was based on the fact that no studies have yet been published on the influence of the layer thickness on the fatigue behaviour under different load ratios and consequently represents a limitation concerning the use in primary structures. The third working assumption was:

> *Reducing the layer thickness improves the durability under fatigue loading*

Four fibre areal weights (30, 60, 120 and 360 gsm) were tested under three load ratios (R=0.1, -0.5 and 10). Overall, the fatigue performance increases with decreasing layer thickness independent of the load ratio. However, the extent of the improvement varies. The most significant improvements were observed under tensile-compressive loading.
The failure behaviour under fatigue does not differ from the static failure behaviour. Due to the higher strength of the 90° layers (in situ strength) and lower interlaminar shear stresses, delaminations are suppressed, and the specimens show a brittle failure behaviour. Under cyclic loading, the reduction in stiffness decreases with decreasing layer thickness.
The load ratio, which represents the maximum fatigue performance, converges towards R=-1 with reducing layer thickness. At this load ratio, the tensile and compressive part of the loading is identical. This behaviour is consistent

with the theory of in situ strength. Suppose the strength of the 90° layers increases exponentially with decreasing layer thickness, the strengths of the 0° and 90° layers will approach each other, and the maximum cyclic performance will converge towards R=-1.
The results show that thinner layer thicknesses positively affect fatigue performance, and working assumption three can be verified.

Another limitation regarding the use of Thin-Ply composites for primary structures is damage growth under fatigue loading. It is already known that the damage caused by an impact in Thin-Ply is more extensive than in Thick-Ply and therefore has to be considered more critically. This behaviour led to the following working assumption:

> *Reducing the layer thickness improves the fatigue behaviour of structures with impact damage*

Four layer thicknesses were tested at a load ratio of R=-0.5, as the influence of impact damage is higher under compressive load. The damage patterns show that the damage area increases significantly with decreasing layer thickness. However, the fatigue results show that the delaminations of the Thin-Ply specimens do not expand below a certain fatigue stress level, and a constant damage pattern is observed. The damage growth was observed by computed tomography. The decrease in fatigue performance due to an impact damage is smaller for Thin-Ply than for Thick-Ply. However, the results also show that fatigue performance reduction is lowest for a fibre areal weight of 120 gsm. The delaminations of the 120 gsm specimens are not circular and have the shape of a peanut. This implies that the delaminations are small in one spatial direction and that there are relatively high residual stiffnesses.
Concerning working assumption four, the assumption can be verified to a certain extent. It could be shown that, especially in high cycle regimes, the conditions of application for primary structures, the Thin-Ply fatigue performance is superior. However, it could also be shown that the geometry of the delaminations has a major impact on the cyclic performance and that

the 120 gsm samples show the lowest reduction of cyclic performance.

The results of the experimental investigations regarding the four working assumptions show that the lightweight potential of primary structures can be increased by using Thin-Ply composites. The research hypothesis of this thesis can therefore be verified.

6.3 Further topics for attention

In this section, conclusions are presented, resulting in the sample preparation or the mechanical tests and can be applied for future investigations. The conclusions are each presented in a brief subsection.

Cutting of the stainless steel foil
Within this thesis, different methods for cutting stainless steel foils were investigated. The main criterion for the quality of the cut was the deformation of the edges. Cutting with a CNC cutter, a carpet knife, a metal shear, a saw with a corundum blade, and a milling machine deformed the edges of the foils and created a kind of wave pattern. Cutting with a precision cutter for electronic boards worked without deformation of the edges, which was used for all tests.

Surface pre-treatment for FML Thin-Ply laminates
The FML specimens' failure behaviour showed that the surface pre-treatment of the stainless steel in the case of Thin-Ply samples has a lower impact concerning the final failure. Although the surface was pre-treated using the Sol-Gel process, delaminations occurred in the Thick-Ply FML samples. The surface pre-treatment is not sufficient with thicker layers, and delaminations initiate due to the high interlaminar shear stresses. The higher number of layers for Thin-Ply samples reduces the interlaminar shear stresses at the

interfaces, and the surface pre-treatment was sufficient. It was not investigated whether a less complex surface pre-treatment method would have been sufficient for Thin-Ply FML samples.

Arrangement of the transition zone
The digital image correlation system showed that locally high stresses had developed in the area of the transition zone between the metal and the CFRP layer. To reduce local stresses, it is essential to enable a uniform stiffness transition over a wide area. A stepwise arrangement achieved a constant stiffness transition. The length of the steps was based on other studies. It was not investigated whether smaller metal foils and less weight would have been sufficient or whether a different arrangement could have reduced weight.

Bearing tests – bolt material
The bearing tests showed that the material of the bolts had to be adapted according to the higher loads due to hybridisation. To ensure the failure of the specimen, high-strength stainless steel (HSS) bolts with a bending strength of 4050 MPa had to be used. Furthermore, the samples were clamped with a torque of 6 Nm. Without clamping, the high-strength stainless steel bolts failed prematurely.

Fatigue tests of brittle materials
The fatigue tests have shown that the load introduction and a standard-compliant failure in the area between the tabs are not possible with Thin-Ply samples with the standard's specimen geometry. The brittle behaviour is more similar to testing a unidirectional specimen. Thin-ply specimens tested with a converted force of more than 12 kN/mm thickness under tensile-tensile or tensile-compressive loading have failed near the tabs with a tab geometry of 50 mm × 25 mm. The specimen geometry has to be changed for a standard-compliant failure. Samples shaped like a dogbone with a constriction of 2 mm on each side did achieve higher stresses, but only because the cross-section was smaller. The specimens still failed at a force of 12 kN/mm at the tabs. A

further reduction of the specimen width and a more considerable constriction have effects that are due to the specimen size, so thinner samples were not investigated within this thesis.

Anti-buckling support - fatigue after impact tests
The fatigue after impact tests demonstrated that the anti-buckling support used as standard at the Institute of Polymer and Composites, which supports the specimen between the tabs from all sides, could not be used in the case of the FAI specimens. Due to the obstruction of the transverse contraction by the anti-buckling support, edge delaminations occur. In the case of large delaminations caused by the impact, the delaminations combine under load and influence the damage propagation. Using an anti-buckling support that does not support the samples to the sides, edge delaminations could be prevented so that the damage growth due to the impact could be observed for Thin-Ply samples.

Bibliography

[1] M. C. Niu. *Composite airframe structures: Practical design information and data*. 3rd publ. Hong Kong: Conmilit Press, 2000. ISBN: 962-7128-06-6.

[2] R. Amacher, W. Smith, J. Botsis, C. Dransfeld, and J. Cugnoni. "New design opportunities using thin-ply composites". In: *Jec Composites Magazine* 96 (2015), pp. 38–40.

[3] P. Camanho, A. Arteiro, A. Turon, J. Costa, and G. Guillamet. "Structural integrity of thin-ply laminates". In: *Jec Composites Magazine* 2012.71 (2012), pp. 49–50.

[4] K. Kawabe, S. Tomoda, and T. Matsuo. "A Pneumatic Process for Spreading Reinforcing Fiber Tow". In: *42nd International SAMPE Symposium* (1997), pp. 65–76.

[5] S. Sihn, R. Kim, K. Kawabe, and S. Tsai. "Experimental studies of thin-ply laminated composites". In: *Composites Science and Technology* 67.6 (2007), pp. 996–1008. ISSN: 02663538. DOI: 10.1016/j.compscitech.2006.06.008.

[6] R. Amacher, W. Smith, C. Dransfeld, J. Botsis, and J. Cugnoni. *Thin-Ply: From Size-Effect Characterization to Real Life Design*. Ed. by Thin Ply Technology SARL.

[7] T. Yokozeki, Y. Aoki, and T. Ogasawara. "Experimental characterization of strength and damage resistance properties of thin-ply carbon fiber/toughened epoxy laminates". In: *Composite Structures* 82.3 (2008), pp. 382–389. ISSN: 02638223. DOI: 10.1016/j.compstruct.2007.01.015.

[8] R. Amacher, J. Cugnoni, J. Botsis, L. Sorensen, W. Smith, and C. Dransfeld. “Thin ply composites: Experimental characterization and modeling of size-effects”. In: *Composites Science and Technology* 101.101 (2014), pp. 121–132. ISSN: 02663538. DOI: 10.1016/j.compscitech.2014.06.027.

[9] A. Arteiro, C. Furtado, G. Catalanotti, P. Linde, and P. P. Camanho. “Thin-ply polymer composite materials: A review”. In: *Composites Part A: Applied Science and Manufacturing* 132 (2020). ISSN: 1359835X. DOI: 10.1016/j.compositesa.2020.105777.

[10] J. Cugnoni, R. Amacher, S. Kohler, J. Brunner, E. Kramer, C. Dransfeld, W. Smith, K. Scobbie, L. Sorensen, and J. Botsis. “Towards aerospace grade thin-ply composites: Effect of ply thickness, fibre, matrix and interlayer toughening on strength and damage tolerance”. In: *Composites Science and Technology* 168 (2018), pp. 467–477. ISSN: 02663538. DOI: 10.1016/j.compscitech.2018.08.037.

[11] M. R. Wisnom, B. Khan, and S. R. Hallett. “Size effects in unnotched tensile strength of unidirectional and quasi-isotropic carbon/epoxy composites”. In: *Composite Structures* 84.1 (2008), pp. 21–28. ISSN: 02638223. DOI: 10.1016/j.compstruct.2007.06.002.

[12] B. G. Green, M. R. Wisnom, and S. R. Hallett. “An experimental investigation into the tensile strength scaling of notched composites”. In: *Composites Part A: Applied Science and Manufacturing* 38.3 (2007), pp. 867–878. ISSN: 1359835X. DOI: 10.1016/j.compositesa.2006.07.008.

[13] M. R. Wisnom, S. R. Hallett, and C. Soutis. “Scaling Effects in Notched Composites”. In: *Journal of Composite Materials* 44.2 (2010), pp. 195–210. DOI: 10.1177/0021998309339865.

[14] A. Afaghi-Khatibi and L. Ye. “Residual Strength Simulation of Fibre Reinforced Metal Laminates Containing a Circular Hole”. In: *Journal of Composite Materials* 31.19 (1997), pp. 1884–1904. DOI: 10.1177/002199839703101901.

[15] T. A. Barreto and R. C. Santiago. "Experimental study of the tensile strength of open-hole fiber-metal laminates". In: *Proceedings of the 4th Brazilian Conference on Composite Materials*. Pontifícia Universidade Católica do Rio de Janeiro, 2018, pp. 473–481. DOI: 10.21452/bccm4.2018.07.03.

[16] G. Wu, Yi Tan, and J. Yang. "Evaluation of residual strength of notched fiber metal laminates". In: *Materials Science and Engineering: A* 457.1-2 (2007), pp. 338–349. ISSN: 09215093. DOI: 10.1016/j.msea.2006.12.135.

[17] B. Bosbach. "Multifunctional fibre metal laminates with improved load bearing capability". Dissertation. Hamburg: Technische Universität Hamburg, 2018.

[18] B. Bosbach, M. Baytekin-Gerngross, E. Heyden, M. Gerngross, J. Carstensen, R. Adelung, and B. Fiedler. "Reaching maximum interlaminar properties in GFRP/nanoscale sculptured aluminium ply laminates". In: *Composites Science and Technology* 167 (2018), pp. 32–41. ISSN: 02663538. DOI: 10.1016/j.compscitech.2018.07.033.

[19] R. M. Frizzell, C. T. McCarthy, and M. A. McCarthy. "An experimental investigation into the progression of damage in pin-loaded fibre metal laminates". In: *Composites Part B: Engineering* 39.6 (2008), pp. 907–925. ISSN: 13598368. DOI: 10.1016/j.compositesb.2008.01.007.

[20] A. Arteiro, G. Catalanotti, J. Xavier, and P. P. Camanho. "Notched response of non-crimp fabric thin-ply laminates: Analysis methods". In: *Composites Science and Technology* 88 (2013), pp. 165–171. ISSN: 02663538. DOI: 10.1016/j.compscitech.2013.09.003.

[21] P. P. Camanho and F. L. Matthews. "Delamination Onset Prediction in Mechanically Fastened Joints in Composite Laminates". In: *Journal of Composite Materials* 33.10 (1999), pp. 906–927. DOI: 10.1177/002199839903301002.

[22] B. Bosbach, M. Baytekin-Gerngross, E. Sprecher, J. Wegner, M. Gerngross, J. Carstensen, R. Adelung, and B. Fiedler. "Maximizing bearing fatigue lifetime and CAI capability of fibre metal laminates by nanoscale sculptured Al plies". In: *Composites Part A: Applied Science and Manufacturing* 117 (2019), pp. 144–155. ISSN: 1359835X. DOI: 10.1016/j.compositesa.2018.11.017.

[23] J. Both, M. Wedekind, and H. Baier. *Simulation and experimental characterization of the bearing behavior of CFRP-metal laminates*. ECCM 15 and 15th European conference on composite materials, Venice, Italy, 2012.

[24] A. Fink, P. P. Camanho, J. M. Andrés, E. Pfeiffer, and A. Obst. "Hybrid CFRP/titanium bolted joints: Performance assessment and application to a spacecraft payload adaptor". In: *Composites Science and Technology* 70.2 (2010), pp. 305–317. ISSN: 02663538. DOI: 10.1016/j.compscitech.2009.11.002.

[25] R. L. Meltzer, Y. R. Fiorini, R. T. Horstman, I. C. Moore, A. L. Batik, T. K. O'Brien, and K. L. Reifsnider. "Fatigue Damage: Stiffness/Strength Comparisons for Composite Materials". In: *Journal of Testing and Evaluation* 5.5 (1977), p. 384. ISSN: 00903973. DOI: 10.1520/JTE10547J.

[26] A. L. Highsmith and K. L. Reifsnider. "Stiffness-Reduction Mechanisms in Composite Laminates". In: *Damage in Composite Materials: Basic Mechanisms, Accumulation, Tolerance, and Characterization* (1982), pp. 103–117. DOI: 10.1520/STP34323S.

[27] E. K. Gamstedt and B. A. Sjögren. "Micromechanisms in tension - compression fatigue of composite laminates containing transverse plies". In: *Composites Science and Technology* 59.2 (1999), pp. 167–178. ISSN: 02663538. DOI: 10.1016/S0266-3538(98)00061-X.

[28] M. H. Beheshty, B. Harris, and T. Adam. "An empirical fatigue-life model for high-performance fibre composites with and without impact

damage". In: *Composites Part A: Applied Science and Manufacturing* 30.8 (1999), pp. 971–987. ISSN: 1359835X. DOI: 10.1016/S1359-835X(99)00009-3.

[29] N.H Tai, M.C Yip, and J.L Lin. "Effects of low-energy impact on the fatigue behavior of carbon/epoxy composites". In: *Composites Science and Technology* 58.1 (1998), pp. 1–8. ISSN: 02663538. DOI: 10.1016/S0266-3538(97)00075-4.

[30] L. Melin. "Fatigue testing and buckling characteristics of impacted composite specimens". In: *International Journal of Fatigue* 24.2-4 (2002), pp. 263–272. ISSN: 01421123. DOI: 10.1016/S0142-1123(01)00081-0.

[31] T. Yokozeki, A. Kuroda, A. Yoshimura, T. Ogasawara, and T. Aoki. "Damage characterization in thin-ply composite laminates under out-of-plane transverse loadings". In: *Composite Structures* 2010.93 (2010), pp. 49–57. ISSN: 02638223. DOI: 10.1016/j.compstruct.2010.06.016.

[32] B. Kötter, P. Polyak, Johann Körbelin, and B. Fiedler. *Influence of ply thickness on failure initiation, propagation and mechanical properties in CFRP laminates*. In: Proceedings of ICFC 7. Vicenza, 2018.

[33] ASTM D5766-02. *Test Method for Open-Hole Tensile Strength of Polymer Matrix Composite Laminates*. West Conshohocken, PA, 2018. DOI: 10.1520/D5766_D5766M-11R18.

[34] ASTM D5961-01. *Test Method for Bearing Response of Polymer Matrix Composite Laminates*. West Conshohocken, PA, 2017. DOI: 10.1520/D5961_D5961M-17.

[35] H. Schürmann. *Konstruieren mit Faser-Kunststoff-Verbunden*. 1. Springer-Verlag Berlin Heidelberg, 2005. ISBN: 978-3-540-72189-5.

[36] I. M. Daniel and O. Ishai. *Engineering mechanics of composite materials*. New York: Oxforn University Press, 1994.

[37] H. Böder, D. Gölden, Ph. Rose, and H. Würmseher. “Kohlenstoffasern - Herstellung, Eigenschaften, Verwendung”. In: *Materialwissenschaft und Werkstofftechnik* 11.8 (1980), pp. 275–281. ISSN: 0933-5137. DOI: 10.1002/mawe.19800110805.

[38] H. M. Hawthorne. “On non-Hookean behaviour of carbon fibres in bending”. In: *Journal of Materials Science* 28.9 (1993), pp. 2531–2535. ISSN: 0022-2461. DOI: 10.1007/BF01151688.

[39] K. Schulte and B. Fiedler. *Structure and properties of composite materials*. 1. ed. Hamburg: TUHH-Technologie-GmbH, 2003. ISBN: 3-930400-53-7.

[40] G. W. Ehrenstein. *Faserverbund-Kunststoffe: Werkstoffe - Verarbeitung - Eigenschaften*. 2., völlig überarbeitete Auflage. München and Wien: Hanser, 2006. ISBN: 978-3-446-22716-3.

[41] K. K. Chawla. *Composite materials: Science and engineering*. Third edition. New York: Springer, 2012. ISBN: 978-1-4939-5015-7.

[42] A. Puck. *Festigkeitsanalyse von Faser-Matrix-Laminaten: Modelle für die Praxis*. München: Hanser, 1996. ISBN: 3446181946.

[43] M. Knops. *Analysis of failure in fiber polymer laminates: The theory of Alfred Puck*. Berlin: Springer, 2008. ISBN: 978-3-540-75765-8.

[44] V. Trappe and K. Harbich. “Intralaminar fatigue behaviour of carbon fibre reinforced plastics”. In: *International Journal of Fatigue* 28.10 (2006), pp. 1187–1196. ISSN: 01421123. DOI: 10.1016/j.ijfatigue.2006.02.037.

[45] H. Schürmann. *Konstruieren mit Faser-Kunststoff-Verbunden*. 2., bearbeitete und erweiterte Auflage. VDI-Buch. Berlin, Heidelberg: Springer-Verlag Berlin Heidelberg, 2007. ISBN: 978-3-540-72189-5. DOI: 10.1007/978-3-540-72190-1.

[46] A. Gagel, D. Lange, and K. Schulte. "On the relation between crack densities, stiffness degradation, and surface temperature distribution of tensile fatigue loaded glass-fibre non-crimp-fabric reinforced epoxy". In: *Composites Part A: Applied Science and Manufacturing* 37.2 (2006), pp. 222–228. ISSN: 1359835X. DOI: 10.1016/j.compositesa.2005.03.028.

[47] M. Rheinfurth, N. Kosmann, D. Sauer, G. Busse, and K. Schulte. "Lamb waves for non-contact fatigue state evaluation of composites under various mechanical loading conditions". In: *Composites Part A: Applied Science and Manufacturing* 43.8 (2012), pp. 1203–1211. ISSN: 1359835X. DOI: 10.1016/j.compositesa.2012.03.021.

[48] C. R. Schultheisz and A. M. Waas. "Compressive failure of composites, part I: Testing and micromechanical theories". In: *Progress in Aerospace Sciences* 32.1 (1996), pp. 1–42. ISSN: 03760421. DOI: 10.1016/0376-0421(94)00002-3.

[49] B. Budiansky, N. A. Fleck, and J. C. Amazigo. "On kink-band propagation in fiber composites". In: *Journal of the Mechanics and Physics of Solids* 46.9 (1998), pp. 1637–1653. ISSN: 00225096. DOI: 10.1016/S0022-5096(97)00042-2.

[50] M. Capriotti, H. E. Kim, F. Lanza Di Scalea, and H. Kim. "Detection of major impact damage to composite aerospace structures by ultrasonic guided waves and statistical signal processing". In: *Procedia Engineering* 199 (2017), pp. 1550–1555. ISSN: 18777058. DOI: 10.1016/j.proeng.2017.09.505.

[51] H. Schmutzler, M. Alder, N. Kosmann, H. Wittich, and K. Schulte. "Degradation monitoring of impact damaged carbon fibre reinforced polymers under fatigue loading with pulse phase thermography". In: *Composites Part B: Engineering* 59 (2014), pp. 221–229. ISSN: 13598368. DOI: 10.1016/j.compositesb.2013.12.010.

[52] C. Garnier, M. Pastor, F. Eyma, and B. Lorrain. "The detection of aeronautical defects in situ on composite structures using Non Destructive Testing". In: *Composite Structures* 93.5 (2011), pp. 1328–1336. ISSN: 02638223. DOI: 10.1016/j.compstruct.2010.10.017.

[53] M. A. Omar and Y. Zhou. "A quantitative review of three flash thermography processing routines". In: *Infrared Physics & Technology* 51.4 (2008), pp. 300–306. ISSN: 13504495. DOI: 10.1016/j.infrared.2007.09.006.

[54] M. Alemi-Ardakani, A. S. Milani, S. Yannacopoulos, L. Bichler, D. Trudel-Boucher, G. Shokouhi, and H. Borazghi. "Microtomographic Analysis of Impact Damage in FRP Composite Laminates: A Comparative Study". In: *Advances in Materials Science and Engineering* 2013 (2013), pp. 1–10. ISSN: 1687-8434. DOI: 10.1155/2013/521860.

[55] G.A.O. Davies, X. Zhang, G. Zhou, and S. Watson. "Numerical modelling of impact damage". In: *Composites* 25.5 (1994), pp. 342–350. DOI: 10.1016/S0010-4361(94)80004-9.

[56] S. Abrate. *Impact engineering of composite structures*. Vol. no. 526. Courses and lectures. Vienna and New York: Springer, 2011. ISBN: 3709105234.

[57] S. Heimbs, S. Heller, P. Middendorf, F. Hähnel, and J. Weiße. "Low velocity impact on CFRP plates with compressive preload: Test and modelling". In: *International Journal of Impact Engineering* 36.10-11 (2009), pp. 1182–1193. ISSN: 0734743X. DOI: 10.1016/j.ijimpeng.2009.04.006.

[58] M. R. Wisnom and S. R. Hallett. "The role of delamination in strength, failure mechanism and hole size effect in open hole tensile tests on quasi-isotropic laminates". In: *Composites Part A: Applied Science and Manufacturing* 40.4 (2009), pp. 335–342. ISSN: 1359835X. DOI: 10.1016/j.compositesa.2008.12.013.

[59] B. Kötter, J. Karsten, J. Körbelin, and B. Fiedler. "CFRP Thin-Ply Fibre Metal Laminates: Influences of Ply Thickness and Metal Layers on Open Hole Tension and Compression Properties". In: *Materials (Basel, Switzerland)* 13.4 (2020). ISSN: 1996-1944. DOI: 10.3390/ma13040910.

[60] K. H. Illgner and J. Esser. *Schrauben Vademecum*. 9., vollst. neu überarb. und erw. Aufl., 40. - 45. Tsd. Bramsche: Rasch, 2001. ISBN: 978-3-935326-46-9.

[61] B. Kolesnikov, H. Wilmes, A. Herrmann, and A. Pabsch. "Composite material with a reinforced connecting area". WO/2000/056541. 2000.

[62] H. Schmutzler. *Damage accumulation monitoring of impact damage in carbon fibre reinforced polymers by means of active thermography: Zugl.: Hamburg, Techn. Univ. Hamburg-Harburg, Diss., 2015*. Vol. 23. Technisch wissenschaftliche Schriftenreihe. Hamburg: TuTech Verl., 2015. ISBN: 9783941492868.

[63] B. Harris. *Fatigue in composites: Science and technology of the fatigue response of fibre-reinforced plastics*. Boca Raton, Fla and Cambridge, U.K: CRC Press, 2003. ISBN: 1 85573 608 X. DOI: 10.1016/B978-1-85573-608-5.50001-2.

[64] Russell D. Jamison. "The role of microdamage in tensile failure of graphite/epoxy laminates". In: *Composites Science and Technology* 24.2 (1985), pp. 83–99. ISSN: 02663538. DOI: 10.1016/0266-3538(85)90053-3.

[65] N. Uda, K. Ono, and K. Kunoo. "Compression fatigue failure of CFRP laminates with impact damage". In: *Composites Science and Technology* 69.14 (2009), pp. 2308–2314. ISSN: 02663538. DOI: 10.1016/j.compscitech.2008.11.031.

[66] O. Attia, A. J. Kinloch, and F. L. Matthews. "The prediction of fatigue damage growth in impact-damaged composite skin/stringer structures. Part I: theoretical modelling studies". In: *Composites Science and Technology* 63.10 (2003), pp. 1463–1472. ISSN: 02663538. DOI: 10.1016/S0266-3538(03)00164-7.

[67] C. Garnier, M. Pastor, B. Lorrain, and O. Pantalé. “Fatigue behavior of impacted composite structures”. In: *Composite Structures* 100 (2013), pp. 443–450. ISSN: 02638223. DOI: 10.1016/j.compstruct.2012.12.025.

[68] N. Tai. “Effects of thickness on the fatigue-behavior of quasi-isotropic carbon/epoxy composites before and after low energy impacts”. In: *Composites Science and Technology* 59.11 (1999), pp. 1753–1762. ISSN: 02663538. DOI: 10.1016/S0266-3538(99)00037-8.

[69] D. D. Symons and G. Davis. “Fatigue testing of impact-damaged T300/914 carbon-fibre-reinforced plastic”. In: *Composites Science and Technology* 60.3 (2000), pp. 379–389. ISSN: 02663538. DOI: 10.1016/S0266-3538(99)00138-4.

[70] M. S. Rosenfeld and L. W. Gause. “Compression Fatigue Behavior of Graphite/Epoxy in the Presence of Stress Raisers”.

[71] A. P. Vassilopoulos, B. D. Manshadi, and T. Keller. “Influence of the constant life diagram formulation on the fatigue life prediction of composite materials”. In: *International Journal of Fatigue* 32.4 (2010), pp. 659–669. ISSN: 01421123. DOI: 10.1016/j.ijfatigue.2009.09.008.

[72] DIN 50100:2016-12. *Schwingfestigkeitsversuch_- Durchführung und Auswertung von zyklischen Versuchen mit konstanter Lastamplitude für metallische Werkstoffproben und Bauteile*. Berlin, 2016. DOI: 10.31030/2580844.

[73] B. Harris. “A historical review of the fatigue behaviour of fibre-reinforced plastics”. In: *Fatigue in Composites*. Elsevier, 2003, pp. 3–35. ISBN: 9781855736085. DOI: 10.1533/9781855738577.1.3.

[74] M. Kawai and M. Koizumi. “Nonlinear constant fatigue life diagrams for carbon/epoxy laminates at room temperature”. In: *Composites Part A: Applied Science and Manufacturing* 38.11 (2007), pp. 2342–2353. ISSN: 1359835X. DOI: 10.1016/j.compositesa.2007.01.016.

[75] G. Boerstra. "The Multislope model: A new description for the fatigue strength of glass fibre reinforced plastic". In: *International Journal of Fatigue* 29.8 (2007), pp. 1571–1576. ISSN: 01421123. DOI: 10.1016/j.ijfatigue.2006.11.007.

[76] C. Kassapoglou. "Fatigue Life Prediction of Composite Structures Under Constant Amplitude Loading". In: *Journal of Composite Materials* 41.22 (2007), pp. 2737–2754. DOI: 10.1177/0021998307078735.

[77] T. P. Philippidis and A. P. Vassilopoulos. "Life prediction methodology for GFRP laminates under spectrum loading". In: *Composites Part A: Applied Science and Manufacturing* 35.6 (2004), pp. 657–666. ISSN: 1359835X. DOI: 10.1016/j.compositesa.2004.02.009.

[78] B. Harris. "A parametric constant-life model for prediction of the fatigue lives of fibre-reinforced plastics". In: *Fatigue in Composites*. Elsevier, 2003, pp. 546–568. ISBN: 9781855736085. DOI: 10.1533/9781855738577.4.546.

[79] N. Gathercole, H. Reiter, T. Adam, and B. Harris. "Life prediction for fatigue of T800/5245 carbon-fibre composites: I. Constant-amplitude loading". In: *International Journal of Fatigue* 16.8 (1994), pp. 523–532. ISSN: 01421123. DOI: 10.1016/0142-1123(94)90478-2.

[80] M. H. Beheshty and B. Harris. "A constant-life model of fatigue behaviour for carbon-fibre composites: the effect of impact damage". In: *Composites Science and Technology* 58.1 (1998), pp. 9–18. ISSN: 02663538. DOI: 10.1016/S0266-3538(97)00121-8.

[81] A. Arteiro, G. Catalanotti, A. R. Melro, P. Linde, and P. P. Camanho. "Micro-mechanical analysis of the in situ effect in polymer composite laminates". In: *Composite Structures* 2014.116 (2014), pp. 827–840. ISSN: 02638223. DOI: 10.1016/j.compstruct.2014.06.014.

[82] B. Kötter, K. Yamada, J. Körbelin, K. Kawabe, M. Nishikawa, M. Hojo, and B. Fiedler. "Steel foil reinforcement for high performance bearing strength in Thin–Ply composites". In: *Composites Part C: Open Access* 4 (2021). ISSN: 26666820. DOI: 10.1016/j.jcomc.2020.100085.

[83] P. P. Camanho, C. G. Dávila, S. T. Pinho, L. Iannucci, and P. Robinson. "Prediction of in situ strengths and matrix cracking in composites under transverse tension and in-plane shear". In: *Composites Part A: Applied Science and Manufacturing* 2006.37 (2006), pp. 165–176. ISSN: 1359835X. DOI: 10.1016/j.compositesa.2005.04.023.

[84] J. Lee and C. Soutis. "A study on the compressive strength of thick carbon fibre–epoxy laminates". In: *Composites Science and Technology* 67.10 (2007), pp. 2015–2026. ISSN: 02663538. DOI: 10.1016/j.compscitech.2006.12.001.

[85] J. Lee and C. Soutis. "Measuring the notched compressive strength of composite laminates: Specimen size effects". In: *Composites Science and Technology* 68.12 (2008), pp. 2359–2366. ISSN: 02663538. DOI: 10.1016/j.compscitech.2007.09.003.

[86] M. J. Laffan, S. T. Pinho, P. Robinson, and L. Iannucci. "Measurement of the in situ ply fracture toughness associated with mode I fibre tensile failure in FRP. Part I: Data reduction". In: *Composites Science and Technology* 70.4 (2010), pp. 606–613. ISSN: 02663538. DOI: 10.1016/j.compscitech.2009.12.016.

[87] G. Catalanotti. "Prediction of in situ strengths in composites: Some considerations". In: *Composite Structures* 207 (2019), pp. 889–893. ISSN: 02638223. DOI: 10.1016/j.compstruct.2018.09.075.

[88] A. Parvizi, K. W. Garrett, and J. E. Bailey. "Constrained cracking in glass fibre-reinforced epoxy cross-ply laminates". In: *Journal of Materials Science* 13.1 (1978), pp. 195–201. ISSN: 0022-2461. DOI: 10.1007/BF00739291.

[89] Y. Nishikawa, K. Okubo, T. Fujii, and K. Kawabe. "Fatigue crack constraint in plain-woven CFRP using newly-developed spread tows". In: *International Journal of Fatigue* 28.10 (2006), pp. 1248–1253. ISSN: 01421123. DOI: 10.1016/j.ijfatigue.2006.02.010.

[90] T. A. Sebaey, E. V. González, C. S. Lopes, N. Blanco, P. Maimí, and J. Costa. "Damage resistance and damage tolerance of dispersed CFRP laminates: Effect of the mismatch angle between plies". In: *Composite Structures* 101 (2013), pp. 255–264. ISSN: 02638223. DOI: 10.1016/j.compstruct.2013.01.026.

[91] H. Saito, M. Morita, K. Kawabe, M. Kanesaki, H. Takeuchi, M. Tanaka, and I. Kimpara. "Effect of ply-thickness on impact damage morphology in CFRP laminates". In: *Journal of Reinforced Plastics and Composites* 30.13 (2011), pp. 1097–1106. ISSN: 0731-6844. DOI: 10.1177/0731684411416532.

[92] T. A. Sebaey and E. Mahdi. "Using thin-plies to improve the damage resistance and tolerance of aeronautical CFRP composites". In: *Composites Part A: Applied Science and Manufacturing* 86 (2016), pp. 31–38. ISSN: 1359835X. DOI: 10.1016/j.compositesa.2016.03.027.

[93] Wu. *Polymer Interface and Adhesion*. 1st ed. New York: CRC Press, 1982. ISBN: 0824715330.

[94] S. Ebnesajjad. *Handbook of adhesives and surface preparation: Technology, applications and manufacturing*. PDL handbook series. Amsterdam: William Andrew/Elsevier, 2011. ISBN: 1437744621.

[95] Charles A. Harper, ed. *Handbook of plastics and elastomers*. New York: McGraw-Hill, 1975. ISBN: 0070266816.

[96] C. Bischof, A. Bauer, W. Possart, R. Kapelle, and R. D. Schulze. "Zur Adhäsion in Metall-Polymer-Grenzschichten und ihrer praktischen Nutzung". In: *Acta Polymerica* 40.3 (1989), pp. 214–221. ISSN: 03237648. DOI: 10.1002/actp.1989.010400309.

[97] C. Bischof. "ND-Plasmatechnik im Umfeld der Haftungsproblematik bei Metall-Polymer-Verbunden". In: *Materialwissenschaft und Werkstofftechnik* 24.2 (1993), pp. 33–41. ISSN: 0933-5137. DOI: 10.1002/mawe.19930240208.

[98] E. H. Andrews and N. E. King. “Adhesion of epoxy resins to metals”. In: *Journal of Materials Science* 11.11 (1976), pp. 2004–2014. ISSN: 0022-2461. DOI: 10.1007/PL00020326.

[99] A. Monden. “Adhäsion zwischen epoxidharzbasiertem CFK und oberflächenmodifiziertem Stahl: Grenzschichtversagen von Hybridlaminaten unter Mode I, Mode II und Mixed-Mode Belastung”. Dissertation. Augsburg: Universität Augsburg, 2016.

[100] R. D. Adams, ed. *Adhesive bonding: Science, technology and applications*. Boca Raton: CRC Press, 2005. ISBN: 0-8493-2584-6.

[101] A. V. Pocius. *Adhesion and adhesives technology: An introduction*. 3rd ed. Munich and Cincinnati: Hanser Publishers and Hanser Publications, 2012. ISBN: 9781569905111.

[102] K. W. Allen and H. S. Alsalim. “Surface Preparation of a Stainless Steel for Adhesive Bonding”. In: *The Journal of Adhesion* 8.3 (2006), pp. 183–194. ISSN: 0021-8464. DOI: 10.1080/00218467608075082.

[103] F. Bouquet, J. M. Cuntz, and C. Coddet. “Influence of surface treatment on the durability of stainless steel sheets bonded with epoxy”. In: *Journal of Adhesion Science and Technology* 6.2 (1992), pp. 233–242. ISSN: 0169-4243. DOI: 10.1163/156856192X00304.

[104] J. G. Teng, D. Fernando, T. Yu, and X. L. Zhao. “Treatment of Steel Surfaces for Effective Adhesive Bonding”. In: *Advances in FRP Composites in Civil Engineering*. Ed. by Lieping Ye, Peng Feng, and Qingrui Yue. Berlin, Heidelberg: Springer Berlin Heidelberg, 2011, pp. 865–868. ISBN: 978-3-642-17486-5. DOI: 10.1007/978-3-642-17487-2_190.

[105] M. Davis and D. Bond. “Principles and practices of adhesive bonded structural joints and repairs”. In: *International Journal of Adhesion and Adhesives* 19.2-3 (1999), pp. 91–105. ISSN: 01437496. DOI: 10.1016/S0143-7496(98)00026-8.

[106] G. W. Critchlow, K. A. Yendall, D. Bahrani, A. Quinn, and F. Andrews. "Strategies for the replacement of chromic acid anodising for the structural bonding of aluminium alloys". In: *International Journal of Adhesion and Adhesives* 26.6 (2006), pp. 419–453. ISSN: 01437496. DOI: 10.1016/j.ijadhadh.2005.07.001.

[107] P. Molitor, V. Barron, and T. Young. "Surface treatment of titanium for adhesive bonding to polymer composites: a review". In: *International Journal of Adhesion and Adhesives* 21.2 (2001), pp. 129–136. ISSN: 01437496. DOI: 10.1016/S0143-7496(00)00044-0.

[108] S. Park, W. Choi, H. Choi, H. Kwon, and S. Kim. "Recent Trends in Surface Treatment Technologies for Airframe Adhesive Bonding Processing: A Review (1995–2008)". In: *The Journal of Adhesion* 86.2 (2010), pp. 192–221. ISSN: 0021-8464. DOI: 10.1080/00218460903418345.

[109] 3M Aerospace and Aircraft Maintenance Department. *3M Surface Pre-Treatment AC-130 and AC-130-2 Metal Alloy Surface Preparation for Bonding - Application Guide*. Ed. by Aerospace and Aircraft Maintenance Department. St. Paul, USA, 2012.

[110] 3M Aerospace and Aircraft Maintenance Department. *3M Surface Pre-Treatment AC-130, Technical Datasheet*. Ed. by 3M Aerospace and Aircraft Maintenance Department. St. Paul, USA, 2012.

[111] T. P. Chou, C. Chandrasekaran, and G. Z. Cao. "Sol-Gel-Derived Hybrid Coatings for Corrosion Protection". In: *Journal of Sol-Gel Science and Technology* 26.1/3 (2003), pp. 321–327. ISSN: 09280707. DOI: 10.1023/A:1020736107842.

[112] E. Gonzalez, N. Vejar, R. Solis, L. Muñoz, M. Victoria Encinas, and M. Paez. "Sol-Gel Films: Corrosion Protection Coating for Aluminium Alloy". In: *Sol-Gel Method - Design and Synthesis of New Materials with Interesting Physical, Chemical and Biological Properties*. Ed. by Guadalupe Valverde Aguilar. IntechOpen, 2019. ISBN: 978-1-78985-333-9. DOI: 10.5772/intechopen.79712.

[113] M. L. Zheludkevich, I. Miranda Salvado, and M. G. S. Ferreira. “Sol–gel coatings for corrosion protection of metals”. In: *Journal of Materials Chemistry* 15.48 (2005). ISSN: 0959-9428. DOI: 10.1039/b419153f.

[114] J. Mazza, G. Gaskin, W. de Piero, and K. Blohowiak. *Sol-Gel technology for low-VOC, nonchromated adhesive bonding applications: (Report no.: AFRL-ML-WP-TR-2004-4063)*. 2004.

[115] 3M Aerospace and Aircraft Maintanance Division. *3M Surface Pre-Treatment AC-130 - Description*. Ed. by 3M Aerospace and Aircraft Maintanance Division. St. Paul, USA, 2012.

[116] Y. Guo and X. Wu. “Bridging stress distribution in center-cracked fiber reinforced metal laminates: modeling and experiment”. In: *Engineering Fracture Mechanics* 63.2 (1999), pp. 147–163. DOI: 10.1016/S0013-7944(99)00018-1.

[117] J.J.C Remmers. “Discontinuities in material and structures”. Dissertation. Delft: Technische Universität Delft, 2006.

[118] L.B Vogelesang and A. Vlot. *Development of fibre metal laminates for advanced aerospace structures*. Vol. 103. Amsterdam and New York: North-Holland, 2000. ISBN: 0444884688. DOI: 10.1016/S0924-0136(00)00411-8.

[119] K. Masania, R. Geissberger, D. Stefaniak, and C. Dransfeld. *Steel foil reinforced composites: Experimental and numerical study of strength, plasticity and ply size effect*. Workshop on Aircraft System Technologies, Hamburg, 2015.

[120] J. Studer, A. Keller, F. Leone, D. Stefaniak, C. Dransfeld, and K. Masania. “Local reinforcement of aerospace structures using co-curing RTM of metal foil hybrid composites”. In: *Production Engineering* 12.2 (2018), pp. 195–201. ISSN: 0944-6524. DOI: 10.1007/s11740-018-0794-3.

[121] E. Petersen, D. Stefaniak, and C. Hühne. "Experimental investigation of load carrying mechanisms and failure phenomena in the transition zone of locally metal reinforced joining areas". In: *Composite Structures* 182 (2017), pp. 79–90. ISSN: 02638223. DOI: 10.1016/j.compstruct.2017.09.002.

[122] G. Kolks and K. I. Tserpes. "Efficient progressive damage modeling of hybrid composite/titanium bolted joints". In: *Composites Part A: Applied Science and Manufacturing* 56 (2014), pp. 51–63. ISSN: 1359835X. DOI: 10.1016/j.compositesa.2013.09.011.

[123] A. Keller, R. Geissberger, J. Studer, F. Leone, D. Stefaniak, J. A. Pascoe, C. Dransfeld, and K. Masania. "Experimental and numerical investigation of ply size effects of steel foil reinforced composites". In: *Materials & Design* 198 (2021). ISSN: 02613069. DOI: 10.1016/j.matdes.2020.109302.

[124] P. P. Camanho, A. Fink, A. Obst, and S. Pimenta. "Hybrid titanium–CFRP laminates for high-performance bolted joints". In: *Composites Part A: Applied Science and Manufacturing* 40.12 (2009), pp. 1826–1837. ISSN: 1359835X. DOI: 10.1016/j.compositesa.2009.02.010.

[125] B. Kolesnikov, L. Herbeck, and A. Fink. "CFRP/titanium hybrid material for improving composite bolted joints". In: *Composite Structures* 83.4 (2008), pp. 368–380. ISSN: 02638223. DOI: 10.1016/j.compstruct.2007.05.010.

[126] J. Lopes, M. Freitas, D. Stefaniak, and P. P. Camanho. "Inter-laminar shear stress in hybrid CFRP/austenitic steel". In: *Frattura ed Integrità Strutturale* 9.31 (2015), pp. 67–79. DOI: 10.3221/IGF-ESIS.31.06.

[127] Hexcel Corporation. *Datasheet - HexPly M21*. Ed. by Hexcel Corporation. Stamford, USA, 2007.

[128] Toray Carbon Fibres America inc. *Datasheet - T800S Carbon firbe*. Tacoma, USA, 2016.

[129] Special XChem. *Datasheet - jER™ 828 - Mitsubishi Chemical*. Waltham, USA, 2018.

[130] Mistubishi Rayon Carbon Fibre & Composites. *Datasheet - GRAFIL 24-700*. Binley, United Kingdom, 2020.

[131] Northern Thin Ply Technology. *Datasheet - NTPT-DS-ThinPreg-402*. Renens, Switzerland, 2017.

[132] Toray Carbon Fibres America inc. *Datasheet - T700S Carbon firbe*. Tacoma, USA, 2016.

[133] Deutsche-Edelstahlwerke GmbH. *Datasheet 1.4310 Chromium-nickel austenitic stainless steel*. Ed. by Deutsche-Edelstahlwerke GmbH. Witten, Germany, 2007.

[134] HSM Stahl- und Metallhandel GmbH. *Werkstoffdatenblatt 1.4310 / X10CrNi18-9: Nichtrostender Stahl, autenitisch*. Ed. by HSM Stahl- und Metallhandel GmbH.

[135] ASTM D3039-00. *Test Method for Tensile Properties of Polymer Matrix Composite Materials*. West Conshohocken, PA, 2017. DOI: 10.1520/D3039_D3039M-17.

[136] ASTM D3410-03. *Standard Test Method for Compressive Properties of Polymer Matrix Composite Materials with Unsupported Gage Section by Shear Loading*. West Conshohocken, PA, 2003. DOI: 10.1520/D3410_D3410M-03.

[137] DIN EN 2564:2019-08. *Luft- und Raumfahrt - Kohlenstofffaser-Laminate - Bestimmung der Faser-, Harz- und Porenanteile; Deutsche und Englische Fassung:2018*. Berlin, 1998. DOI: 10.31030/3064174.

[138] ASTM E345-16. *Test Methods of Tension Testing of Metallic Foil*. West Conshohocken, PA, 2016. DOI: 10.1520/E0345-16.

[139] ASTM D5528-01. *Test Method for Mode I Interlaminar Fracture Toughness of Unidirectional Fiber-Reinforced Polymer Matrix Composites*. West Conshohocken, PA, 2013. DOI: 10.1520/D5528-13.

[140] ASTM D7905-14. *Test Method for Determination of the Mode II Interlaminar Fracture Toughness of Unidirectional Fiber-Reinforced Polymer Matrix Composites*. West Conshohocken, PA, 2014. DOI: 10.1520/D7905_D7905M-14.

[141] ASTM D2344-00. *Test Method for Short-Beam Strength of Polymer Matrix Composite Materials and Their Laminates*. West Conshohocken, PA, 2006. DOI: 10.1520/D2344_D2344M-00R06.

[142] *DIN EN ISO 4957:2018-11, Werkzeugstähle (ISO_4957:2018); Deutsche Fassung*. Berlin, 2018. DOI: 10.31030/2842661.

[143] ASTM D6484-04. *Test Method for Open-Hole Compressive Strength of Polymer Matrix Composite Laminates*. West Conshohocken, PA, 2014. DOI: 10.1520/D6484_D6484M-20.

[144] ASTM D7136-05. *Test Method for Measuring the Damage Resistance of a Fiber-Reinforced Polymer Matrix Composite to a Drop-Weight Impact Event*. West Conshohocken, PA, 2005. DOI: 10.1520/D7136_D7136M-20.

[145] W. Weißbach. *Werkstoffkunde: Strukturen, Eigenschaften, Prüfung*. 16., überarbeitete Auflage. Wiesbaden: Friedr. Vieweg & Sohn Verlag | GWV Fachverlage GmbH Wiesbaden, 2007. ISBN: 9783834802958. DOI: 10.1007/978-3-8348-9417-5.

[146] S. P. Garbo and J. M. Ogonowski. *Effect of variances and manufacturing tolerances on the design strength and life of mechanically fastened composite joints: Volume 3 - Methodology development and data evaluation, Final report AFWAL-TR-81-3041*. Wright-Patterson Air Force Base, Ohio, 1981.

[147] P. P. Camanho. "Application of numerical methods to the strength prediction of mechanically fastened joints in composite laminates". Dissertation. London: Imperial College of Science, 1999.

[148] ASTM D7137-05. *Test Method for Compressive Residual Strength Properties of Damaged Polymer Matrix Composite Plates*. West Conshohocken, PA, 2005. DOI: 10.1520/D7137_D7137M-05.